

This article was downloaded by:

On: 21 January 2011

Access details: *Access Details: Free Access*

Publisher *Taylor & Francis*

Informa Ltd Registered in England and Wales Registered Number: 1072954 Registered office: Mortimer House, 37-41 Mortimer Street, London W1T 3JH, UK



International Reviews in Physical Chemistry

Publication details, including instructions for authors and subscription information:

<http://www.informaworld.com/smpp/title~content=t713724383>

Heterogeneous uptake and reaction of nitrogen oxides and volatile organic compounds on the surface of atmospheric particles including oxides, carbonates, soot and mineral dust: Implications for the chemical balance of the troposphere

Vicki H. Grassian

Online publication date: 26 November 2010

To cite this Article Grassian, Vicki H.(2011) 'Heterogeneous uptake and reaction of nitrogen oxides and volatile organic compounds on the surface of atmospheric particles including oxides, carbonates, soot and mineral dust: Implications for the chemical balance of the troposphere', *International Reviews in Physical Chemistry*, 20: 3, 467 – 548

To link to this Article: DOI: 10.1080/01442350110051968

URL: <http://dx.doi.org/10.1080/01442350110051968>

PLEASE SCROLL DOWN FOR ARTICLE

Full terms and conditions of use: <http://www.informaworld.com/terms-and-conditions-of-access.pdf>

This article may be used for research, teaching and private study purposes. Any substantial or systematic reproduction, re-distribution, re-selling, loan or sub-licensing, systematic supply or distribution in any form to anyone is expressly forbidden.

The publisher does not give any warranty express or implied or make any representation that the contents will be complete or accurate or up to date. The accuracy of any instructions, formulae and drug doses should be independently verified with primary sources. The publisher shall not be liable for any loss, actions, claims, proceedings, demand or costs or damages whatsoever or howsoever caused arising directly or indirectly in connection with or arising out of the use of this material.



Heterogeneous uptake and reaction of nitrogen oxides and volatile organic compounds on the surface of atmospheric particles including oxides, carbonates, soot and mineral dust: implications for the chemical balance of the troposphere

VICKI H. GRASSIAN

Departments of Chemistry and Chemical and Biochemical Engineering, and the Center for Global and Regional Environmental Research, The University of Iowa, Iowa City, IA 52242, USA

The role of heterogeneous reactions of trace atmospheric gases on solid aerosol surfaces in the troposphere is not well understood. In this review, the heterogeneous chemistry of nitrogen oxides and volatile organic compounds on the surface of atmospherically relevant particles such as oxides, soot, carbonates and mineral dust is discussed. The approach to unravelling both the molecular level details and the global significance of these reactions is one that combines laboratory investigations and atmospheric chemistry models. The laboratory investigation utilizes spectroscopic measurements to provide an understanding of the details of the chemistry that occurs in the gas phase and on the surface of the particle together with kinetic measurements in order to quantify the rates of these reactions. These fundamental measurements provide a basis for understanding the detailed molecular level physical chemistry of atmospheric processes. The kinetic data, together with the details provided by the spectroscopic studies, are incorporated into atmospheric chemistry models in order to gain a greater understanding of the role that heterogeneous chemistry plays in the chemical balance of the troposphere. Several examples from the present author's laboratory are discussed in this review. These examples include: (i) the heterogeneous uptake and reactivity of nitrogen oxides (nitrogen dioxide and nitric acid) on oxide and dust particles; (ii) the role of water in the heterogeneous uptake of nitric acid on oxide, carbonate and dust particles; (iii) the heterogeneous production of nitrous acid on silica and soot particles; and (iv) the heterogeneous uptake and reactivity of acetone and other carbonyl compounds on oxide and mineral dust particles.

	PAGE
1. Introduction	469
1.1. Background	469
1.2. The approach to these studies	471
2. Methods used in the laboratory studies and box-model analysis	472
2.1. Spectroscopic measurements	474
2.1.1. Transmission Fourier transform infrared spectroscopy of the solid surface and the gas phase	474
2.1.2. Diffuse reflectance ultraviolet–visible spectroscopy of surface-bound species	475
2.2. Transmission electron microscopy and X-ray analysis	476

2.3. Methods used in measuring heterogeneous reaction kinetics	476
2.3.1. Knudsen cell measurements: experimental apparatus and data analysis methods	476
2.3.2. Kinetic measurements utilizing transmission infrared spectroscopy	487
2.3.3. Aerosol reaction chamber	488
2.4. Atmospheric chemistry models and equations used in the box-model analysis	490
3. Heterogeneous uptake of NO₂ and HNO₃ on oxide and mineral dust particles	491
3.1. The importance of heterogeneous uptake of nitrogen oxides in the troposphere	491
3.2. Spectroscopic measurements following adsorption and reaction of NO ₂ and HNO ₃ on oxide particles	492
3.3. Knudsen cell measurements of NO ₂ and HNO ₃ on oxide particles and authentic dust samples	496
3.4. Model analysis of the heterogeneous uptake of NO ₂ and HNO ₃ on mineral dust aerosol	501
4. Role of H₂O vapour and surface-adsorbed H₂O in the heterogeneous uptake of HNO₃ on oxide, carbonate and authentic dust particles	508
4.1. The importance of adsorbed water in heterogeneous reactions	508
4.2. <i>In-situ</i> spectroscopic measurements of the heterogeneous reaction of HNO ₃ on CaCO ₃ particles in the presence of H ₂ O	509
4.3. Transmission electron microscopy measurements of the carbonate particles	511
4.4. <i>In-situ</i> spectroscopic measurements of the heterogeneous reaction of HNO ₃ on oxide particles in the presence of H ₂ O	513
4.5. Knudsen cell studies on the effect of surface-adsorbed H ₂ O on the heterogeneous reactivity of HNO ₃ on oxide and mineral dust particles	519
4.6. Corrections needed to the box-model analysis	519
5. Heterogeneous formation of HONO on solid aerosol particles	519
5.1. The importance of HONO in the troposphere	519
5.2. Spectroscopic measurements of the heterogeneous reaction of NO ₂ on soot and wetted SiO ₂ particles	522
5.3. Knudsen cell measurements of the heterogeneous reaction of NO ₂ on wetted SiO ₂ and soot	525
5.4. Atmospheric relevance and box-model analysis	530
6. Heterogeneous uptake of volatile organic compounds on oxide, carbon black and mineral dust particles	531
6.1. The importance of carbonyl compounds in the troposphere	531
6.2. Transmission Fourier transform infrared and diffuse reflectance ultraviolet–visible spectroscopy of acetaldehyde, acetone and propionaldehyde adsorbed on SiO ₂ , α -Al ₂ O ₃ , α -Fe ₂ O ₃ , CaO and TiO ₂	532
6.3. Knudsen cell measurements: heterogeneous uptake kinetics for acetaldehyde, acetone and propionaldehyde on SiO ₂ , α -Al ₂ O ₃ , α -Fe ₂ O ₃ , CaO and TiO ₂	536

6.4. Box-model analysis: atmospheric implications of carbonyl adsorption on mineral dust aerosol	540
7. Conclusions	543
Acknowledgements	543
References	544

1. Introduction

1.1. *Background*

With estimated annual emissions of 3000–5000 Tg of particulate matter in the form of soil dust, sea salt, organics, sulphate aerosol and soot (Jonas *et al.* 1995), it is clear there are many large and diverse sources of surfaces that can facilitate heterogeneous chemistry in the troposphere. The role that heterogeneous chemistry on solid aerosol surfaces plays in the troposphere remains an important question. It is known that particulate matter can influence radiative transfer by absorption and scattering of solar and terrestrial radiation, and by changing the optical properties of clouds through modification of the distribution of cloud condensation nuclei (Charlson *et al.* 1992). However, much less is known regarding their role as reactive surfaces; yet understanding the chemical interactions between the gas and aerosol phases is important because these processes may result in a change in aerosol composition and size distribution and thus alter aerosol optical properties. Furthermore, these processes may perturb the photochemical oxidant and biogeochemical cycles.

From a photochemical perspective, heterogeneous pathways that directly impact gaseous NO_x , HO_x and/or ozone (O_3) are of great interest. There is increasing evidence that interesting heterogeneous chemistry involving O_3 and its precursors takes place on aerosol surfaces typical of those present in the atmosphere (Ammann *et al.* 1998, Gard *et al.* 1998, Jacob 2000). A fundamental factor is that O_3 is not directly emitted into the atmosphere but is instead formed by a complex set of photochemical reactions involving nonlinear interactions of NO_x ($\text{NO}_x = \text{NO} + \text{NO}_2$) and volatile organic compounds (VOCs). Thus, an understanding of all processes that control NO_x and VOC concentrations is key to the development of models that can accurately describe tropospheric O_3 formation. Figure 1 depicts a portion of the photochemical cycle and some potential reactions of trace atmospheric gases on solid aerosols that may be of importance in the chemical balance of the troposphere.

As discussed in an article by Ravishankara (1997), our ability to predict accurately the composition of the troposphere will depend on advances in understanding the role of particulate matter in the atmosphere and the extent to which heterogeneous reactions on solids and multiphase reactions in liquid droplets contribute to the chemistry. Stratospheric particles, known as polar stratospheric clouds (PSCs), have been relatively well studied because of their role in converting chlorine-containing reservoir compounds into photoactive chlorine-containing compounds that result in stratospheric O_3 depletion (see Kolb *et al.* (1995) and Molina *et al.* (1996), and references therein). PSCs are mainly composed of ice and nitric acid trihydrate. The troposphere, in contrast, has a much higher particle

Potential reactions of trace atmospheric gases with solid aerosol particles

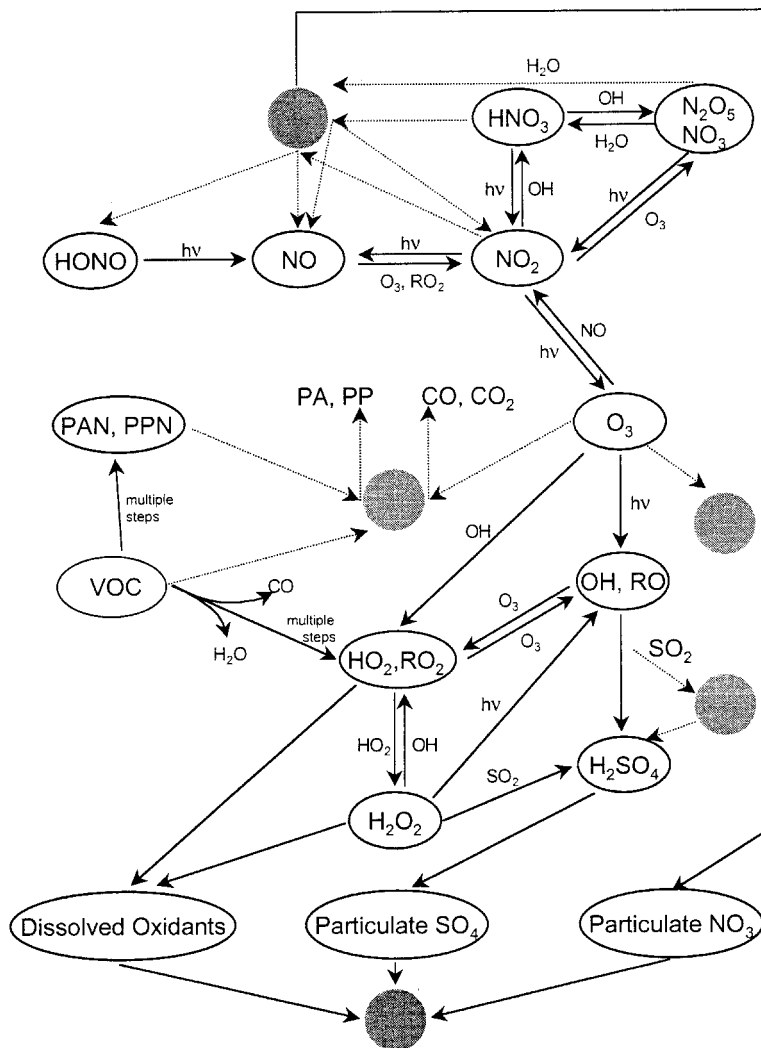


Figure 1. A portion of the photochemical cycle is depicted with known gas-phase chemistry and includes potential reactions of trace atmospheric gases on solid aerosol surfaces (represented by shaded circles): PA, peroxyacetyl radical; PAN, peroxyacetyl nitrate; PP, peroxypropionyl radical; PPN, peroxypropionyl nitrate.

density and there is also a much greater diversity in the types of particle present relative to the stratosphere. These particles include soot, sea salt, sulphates, organics and mineral dust. The heterogeneous chemistry of salt particles, such as sodium chloride (NaCl), with atmospheric gases has received a fair amount of attention because of the release of reactive chlorine atoms that occurs with many of these reactions. The reader is referred to two recent and insightful review articles on the chemistry of sea salt (DeHaan *et al.* 1999, Hemminger 1999).

The motivation for the studies described herein is the recognition that the photochemical oxidant cycle can be altered through heterogeneous uptake and subsequent reactions of atmospheric gases on solid particle surfaces present in the global troposphere. A large fraction of our studies has focused on delineating the potential importance of reactions of trace atmospheric gases on mineral aerosol. Mineral aerosol comes in the form of wind-blown soils and is an important component of the Earth-atmosphere system. It is estimated that 1000–3000 Tg of mineral aerosol are emitted annually into the atmosphere (Jonas *et al.* 1995). Furthermore the emissions of mineral aerosol may be increasing substantially as the arid and semiarid areas expand owing to shifting precipitation patterns and land use changes associated with overgrazing, erosion, land salinization, and mining and industrial activities (Sheehy 1992). The importance of mineral dust interactions on tropospheric chemistry has been the subject of several modelling studies (Dentener and Crutzen 1993, Zhang *et al.* 1994, Dentener *et al.* 1996, Tabazadeh *et al.* 1998). Dentener *et al.* (1996) investigated the impact of irreversible reactions of nitric acid (HNO_3), dinitrogen pentoxide (N_2O_5), nitrogen trioxide (NO_3), HO_2 , O_3 and SO_y on mineral dust surfaces. The results from the modelling study indicate that mineral aerosols may have a significant impact on the chemistry of the troposphere. However, the surface chemistry of mineral aerosol is an area of research that has yet to be fully explored. Mineral aerosols are composed, in part, of metallic and non-metallic oxides, namely silicates and aluminium silicates, as well as other oxides (e.g. haematite) and carbonates, to list a few examples (Bunce 1994).

As discussed here, laboratory studies are vital to answering questions regarding the role of solid aerosol in the troposphere. Some of the issues and questions that need to be addressed include the following: (i) Do gases readily adsorb on the surface of a solid aerosol that can then be removed from the atmosphere via wet or dry deposition, thereby providing a sink for the gas? (ii) Do surface reactions contribute to the conversion of one gas-phase species into another? (iii) Are these surface reactions catalytic or does the surface become deactivated with time? (iv) Is the reaction surface limited or can there be reaction with the bulk of the particle? (v) How fast do these reactions occur? (vi) Can atmospheric processing of solid aerosol particles affect the water (H_2O) uptake and optical properties of the aerosol? (vii) What is the dependence of these reactions on atmospheric conditions such as pressure, relative humidity (RH) and temperature?

As Ravishankara (1997) discussed, these reactions must be fast enough to be competitive with known gas-phase chemical and photochemical reactions if heterogeneous chemistry is to have an appreciable effect on the chemical balance of the troposphere.

1.2. *The approach to these studies*

The questions listed above can be answered through a combination of kinetic and spectroscopic measurements of the gas phase and surface of the solid particle. In particular, the analytical tools of surface science may be particularly helpful in unravelling the details of the heterogeneous chemistry (Vogt *et al.* 1996). The results of the laboratory studies can then be incorporated into atmospheric chemistry models in order to assess the global significance. The approach that we have taken to these studies is one that utilizes both laboratory measurements and box-model analysis. The modelling activities provide a means to evaluate rapidly the significance of new laboratory findings and to help to guide the laboratory studies to those

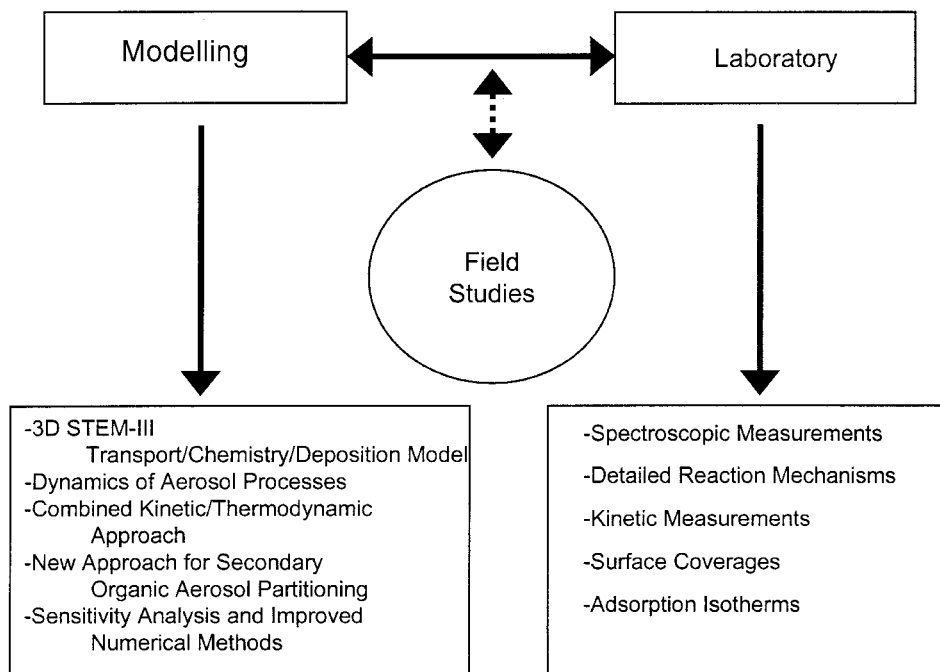


Figure 2. The approach that is taken to understanding the role of solid aerosol particles in the atmosphere is one that combines laboratory measurements with box-model analysis. This approach provides an understanding of the detailed molecular-level chemistry and the global atmospheric significance. Field studies provide important information that guides the laboratory and modelling activities.

areas that have high sensitivity and importance. The laboratory studies provide a molecular-level understanding of the mechanism of adsorption and reaction of atmospheric gases on aerosol surfaces and the identification of saturation effects and product species, which are then accounted for in new model formulations. This multidisciplinary approach which combines modelling and laboratory components is extremely effective. Some of the methods and objectives of the modelling and laboratory components are summarized in figure 2. The critical importance of accurate and reliable field studies needed to guide atmospheric modelling and laboratory activities is indicated in figure 2 as well. Field studies provide data on the composition of the atmosphere including particle density, composition and size as well as concentrations of trace atmospheric gases.

2. Methods used in the laboratory studies and box-model analysis

A majority of the laboratory experiments discussed here are done on solids in the powdered form and not suspended as an aerosol. Detailed information about the surface chemistry and the adsorption process of trace atmospheric gases on atmospherically relevant solids is derived from the laboratory measurements. The experimental methods include transmission Fourier transform infrared (FTIR) spectroscopy, diffuse reflectance ultraviolet (UV)–visible spectroscopy and transmis-

sion electron microscopy (TEM) coupled with X-ray microanalysis. Kinetic measurements have been made with several techniques. A Knudsen cell reaction chamber coupled to a quadrupole mass spectrometer is used to measure uptake on powdered samples under dry conditions and to quantify reaction products. The rate of formation of surface-bound products as a function of RH is measured using FTIR spectroscopy in order to delineate the role of adsorbed H₂O in the heterogeneous reaction kinetics. A newly constructed environmental aerosol chamber is also described. In this chamber, kinetic measurements are made of gas-phase reactants in the presence of suspended particles.

The experimental techniques used are quite complementary and allow us to probe the solid and the gas phase, so that a complete understanding of the reactants, products and intermediates on the surface and in the gas phase may be obtained. A very important consideration is the surface area of the particles and this quantity is determined with a multipoint-Brunauer–Emmett–Teller (BET) apparatus using molecular nitrogen (N₂) as the adsorbate. Surface areas of all powdered samples used in these experiments including authentic dust samples and freshly prepared soot samples have been measured in our laboratory. A summary of the properties of the powders used in these studies is given in table 1. The details of the laboratory experiments, data analysis and atmospheric chemistry models are described in the next few pages.

Table 1. The commercial sources and tabulated values of the average diameters and BET surface areas of oxide particles and authentic dust samples used in these studies.

Sample	Source	Diameter (cm)	S_{BET} (cm ² mg ⁻¹)
α -Al ₂ O ₃	Aesar	1.0×10^{-4}	140
γ -Al ₂ O ₃	Degussa	1.8×10^{-6}	1010
α -Fe ₂ O ₃	Aldrich	6.9×10^{-5}	23
γ -Fe ₂ O ₃	Aesar	2.3×10^{-6}	500
TiO ₂	Degussa	2.5×10^{-6}	500
SiO ₂	Degussa	2.0×10^{-6}	2300
MgO	Aesar	1.0×10^{-4}	150
CaO	Aesar	1.3×10^{-4}	39
CaCO ₃	Aldrich	3.5×10^{-4}	59
Gobi dust	^a	4.0×10^{-4}	110
Saharan sand	^b	2.5×10^{-3}	31
Hexane soot	^c	3.9×10^{-6}	760

^a From M. Nishikawa, National Institute for Environmental Studies, Tsukuba, Ibaraki, Japan. Chemical composition from X-ray microanalysis (excluding carbon and oxygen): 48% Si, 22% Ca, 10% Fe, 10% Al, 7% K, 2% Mg and 1% Ti.

^b From C. Galy-Lacaux, Laboratory of Aerology, Observatory Midi-Pyrenes, Toulouse, France. Chemical composition from X-ray microanalysis (excluding carbon and oxygen): 80% Si, 1% Ca, 7% Fe, 8% Al, 2% K, 1% Mg and 1% Ti.

^c Hexane soot was prepared from a flame.

2.1. Spectroscopic measurements

2.1.1. Transmission Fourier transform infrared spectroscopy of the solid surface and the gas phase

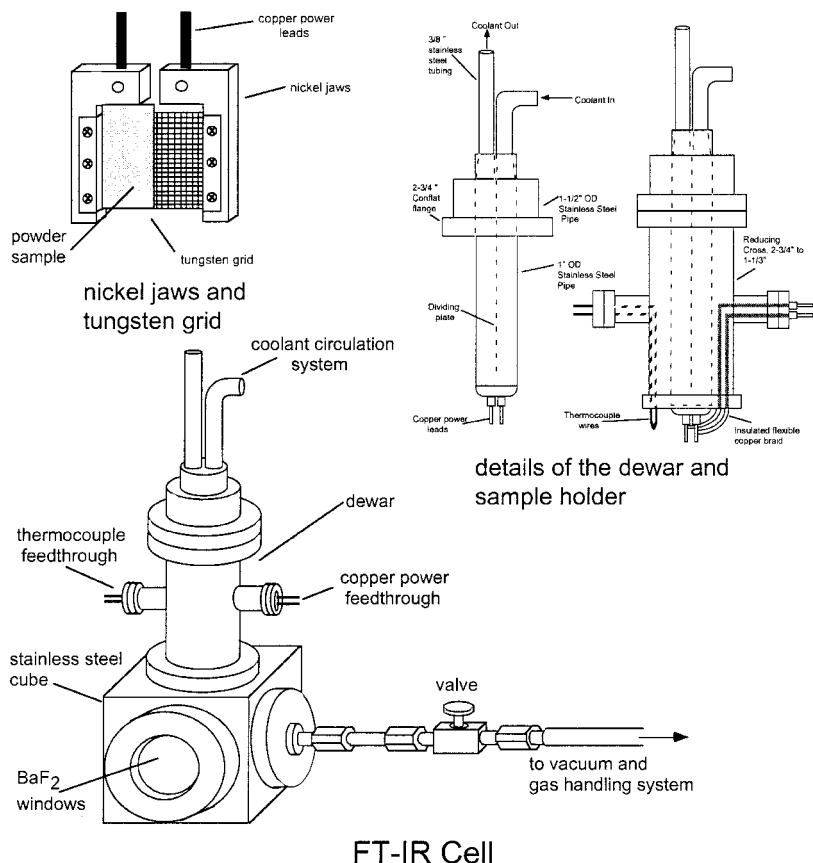
In the studies described herein, transmission infrared (IR) spectroscopy is used to probe the surface of solid particles including oxides, carbonate and soot samples after adsorption and reaction of trace atmospheric gases. The IR cell used in these studies is designed such that spectroscopic measurements could be made of both the gas phase and the surface (figure 3) and thus can provide a complete spectroscopic picture of the two important phases under investigation. This is accomplished by coating the powder on to half of a tungsten grid, leaving the other half of the grid blank so that gas-phase measurements can be made. Depending on the size, chemical composition or the porosity of the powder, samples are coated on to the grid in slightly different ways. The powder can be evenly coated by spraying a water slurry of the particles with an atomizer on to a slightly heated tungsten grid, or by painting a paste of the powder on to the grid, or by pressing the powder into the holes of the grid. In the case of freshly prepared hexane soot, the soot is directly deposited from the flame on to the grid.

The tungsten grid, half-covered with the sample, is then mounted in the IR cell. A schematic diagram of the IR cell is shown in figure 3. The cell consists of a stainless steel cube with two differentially pumped IR windows made of barium fluoride (BaF_2) and a set of nickel jaws attached to a nickel feedthrough. The tungsten grid is held in place by the nickel jaws and can be resistively heated or cooled by flowing a coolant through the dewar to which the nickel feedthrough is attached. The temperature of the sample is monitored by spot welding thermocouple wires to the centre of the grid.

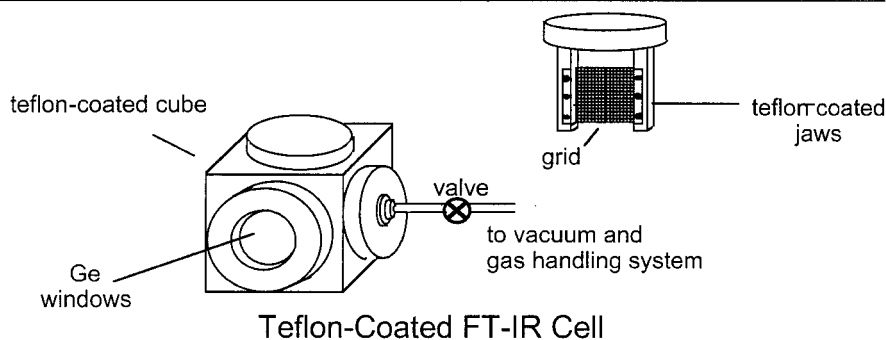
The IR cell is seated on a linear translator inside the FTIR spectrometer so that both halves of the grid could be measured by simply moving the IR cell through the IR beam path. The positions of the linear translator and the size of the IR beam (via a computer-controlled variable iris) are adjusted such that the beam only interrogates each half of the grid. IR spectra are recorded with a Mattson RS-10000 equipped with a narrow-band mercury-cadmium-telluride detector and water-cooled IR source. Typically, 250 or 500 scans are acquired at an instrument resolution of 4 cm^{-1} . The low-frequency cut-off of the spectrometer is near 750 cm^{-1} because of the detector window.

The entire IR cell is attached to a vacuum chamber through a bellows hose. The vacuum chamber consists of a turbomolecular pump, 80 L s^{-1} ion pump, two absolute pressure transducers for accurate pressure measurements in the 0.001–1000 Torr range and a manifold for gas introduction. After the tungsten grid is placed into the IR cell, the system is evacuated to a pressure of 1×10^{-6} Torr. In some cases it is necessary to heat the particles under vacuum to remove adsorbed H_2O and carbonaceous deposits such as adsorbed carbonate or hydrocarbon impurities from the sample.

The IR cell and gas-handling system described above can be used for experiments involving nitrogen dioxide (NO_2), acetaldehyde, acetone and propionaldehyde. HNO_3 decomposes on the walls of the stainless steel reactor; so, for these studies, the stainless steel cube and the jaws are both Teflon coated. The Teflon-coated jaws are attached directly to the top flange of the cube so that the grid could not be heated or cooled (see figure 3). The gas-handling system for the HNO_3 experiments is completely made from glass and Teflon tubing. IR windows made of germanium



FT-IR Cell



Teflon-Coated FT-IR Cell

Figure 3. A schematic diagram of the FTIR cell and other components used to measure the IR spectrum of surface-bound and gas-phase species. For experiments with HNO₃, a Teflon-coated FTIR cell was used.

are found to be less reactive with HNO₃ and are used in place of the BaF₂ windows.

2.1.2. Diffuse reflectance ultraviolet-visible spectroscopy of surface-bound species

UV-visible diffuse reflectance spectra of the powder before and after adsorption of trace atmospheric gases were obtained with a Perkin-Elmer Lambda 20 UV-visible spectrophotometer equipped with an internal diffuse reflectance attachment

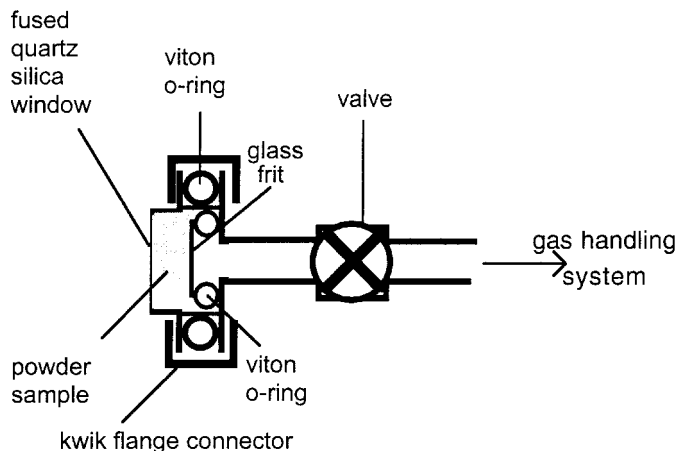


Figure 4. Diffuse reflectance UV-visible sample holder used for measuring changes in the reflectivity spectrum of powdered samples following the adsorption of gases.

(LabSphere). The design of the sample holder used for these measurements is shown in figure 4. The sample holder consists of a 1 inch UV-grade fused silica (SiO_2) window mounted on an ISO flange. Approximately 150 mg of the powdered sample is needed to cover the window completely. A glass frit is placed on top of the powder and a Viton O-ring is used to hold the glass frit in place. The sample holder is connected to another flange with a VCR fitting. The entire assembly is attached to a vacuum system through the VCR connection. Background scans are collected of the powder before the introduction of gases. UV-visible data are plotted as percentage reflectivity ($\%R$): $\%R = (R/R_0) \times 100$, where R_0 is the reflectivity of the powder prior to adsorption and R is the reflectivity after adsorption of the gas.

2.2. Transmission electron microscopy and X-ray analysis

TEM was used to characterize the particle size for the different samples investigated. A Hitachi H-600 electron microscope operating at an acceleration voltage of 100 kV was used to image oxide, carbonate and soot particles. Particles were deposited on to a Formvar-coated copper grid (400 mesh) and then imaged. Particle size distributions were determined from analysing approximately 50 particles for each of the powdered samples. Chemical analysis of the authentic dust samples was determined by the energy-dispersive X-ray technique.

2.3. Methods used in measuring heterogeneous reaction kinetics

2.3.1. Knudsen cell measurements: experimental apparatus and data analysis methods

The use of the Knudsen cell, a very-low-pressure flow reactor, to obtain kinetic information for heterogeneous gas-solid and gas-liquid reactions was pioneered over 30 years ago by Golden *et al.* (1973). The technique is ideally suited to the study of heterogeneous reactions in that, at the experimental pressures used, the mean free path of the molecules in the cell usually exceeds the dimensions of the cell. This minimizes the possibility of gas-phase collisions and eliminates boundary-layer effects, which greatly simplifies the analysis of the data. The Knudsen cell can be used at higher pressures, but to assure molecular flow the mean free path must be a

factor of at least ten greater than the diameter of the exit aperture (Golden *et al.* 1973). The technique has a wide dynamic range with the ability to measure reaction probabilities from near unity down to 10^{-7} (Caloz *et al.* 1997).

The general design of Knudsen cell reactors for the study of heterogeneous reactions has been described in detail in the literature (Golden *et al.* 1973, 1994, Caloz *et al.* 1997). Typically, the reactor consists of a chamber with an isolated sample compartment and a small aperture through which gas-phase reactant and product species can escape to be detected, usually by mass spectrometry. Choice of the area A_h of the aperture (or hole), and the volume V of the reactor determine the escape constant k_{esc} , that is the first-order rate constant, through the cell, as given by

$$k_{\text{esc}} = \frac{\bar{c}A_h}{4V}, \quad (1)$$

where \bar{c} is the average molecular speed of the gas molecules. The residence time τ of the gas-phase molecules in the cell is defined as the inverse of k_{esc} :

$$\tau = \frac{1}{k_{\text{esc}}}. \quad (2)$$

Two different kinds of Knudsen cell reactor are used in these experiments: a single-sample-holder Knudsen cell reactor and a multisample-holder reactor. There are advantages and disadvantages of each of these designs. The obvious advantage of the multisample Knudsen cell is that different samples (either different powders or the same powder but different masses) can be analysed in a single run. The disadvantage is that the volume of the reactor needs to be at least 1000 cm^3 and thus limits the values of k_{esc} that can be reasonably obtained. The advantage of the single-sample-holder Knudsen cell reactor is that the volume of the reactor can be made much smaller, of the order of 100 cm^3 , and thus k_{esc} values as large as $5\text{--}10 \text{ s}^{-1}$ can be obtained. The single-stage Knudsen cell reactor was used to measure the heterogeneous reaction kinetics of carbonyl compounds on oxide particles and authentic dust samples and the heterogeneous reaction kinetics of NO_2 on soot samples. The reactor consists of a stainless steel cross that serves as the reaction chamber. The reaction chamber is coupled to a quadrupole mass spectrometer (UTI model 100C) through a gate valve. The mass spectrometer is pumped by a 150 L s^{-1} ion pump (Varian). The region between the exit aperture and the gate valve is differentially pumped by a 70 L s^{-1} turbo molecular pump (Varian). Gas molecules are introduced into the reaction chamber through a leak valve. A stainless steel sample holder sits on top of a tee support in the reaction chamber and is O-ring sealed by a blank flange. The geometric area A_s of the sample holder is 11.95 cm^2 . The blank flange is attached to a push-pull linear motion feedthrough so that the sample holder can be completely and quickly opened by pulling up on the linear motion feedthrough. The volume of the sealed sample holder is small such that, when the sample holder lid is lifted and opened, there is no observed drop in gas pressure if no adsorbent is present. A linear rotary motion feedthrough is used to change the size of the escape aperture in vacuum. The effective area A_h of the escape aperture used in the VOC experiments was 0.0179 cm^2 , after accounting for the Clausing factor (Dushman 1962). The experimentally determined first-order escape constants were measured to be 0.11, 0.17 and 0.10 s^{-1} for acetaldehyde, acetone and propionaldehyde respectively. The escape constant was determined by abruptly

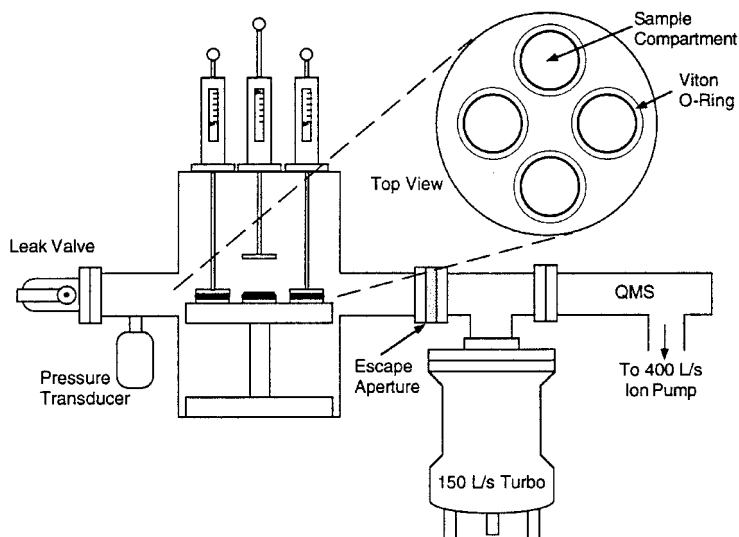


Figure 5. A schematic diagram of the multisample Knudsen cell reactor used to measure heterogeneous uptake kinetics of NO_2 and HNO_3 on oxide particles and authentic dust samples.

changing the inlet flow of each gas while monitoring the quadrupole mass spectrometry (QMS) intensity of the parent ion as a function of time. A plot of the natural logarithm of the QMS intensity as a function of time gave a straight line of slope equal to $-k_{\text{esc}}$. For the NO_2 experiments, a larger aperture was used and k_{esc} was determined to be 0.36 s^{-1} . In more recent experiments in our laboratory (not shown here), larger escape constants of the order of 5 s^{-1} are used.

The multisample Knudsen cell reactor is used to measure the heterogeneous kinetics of NO_2 and HNO_3 uptake on oxide, carbonate and authentic dust samples. A schematic diagram of the reaction chamber of the multisample Knudsen cell is shown in figure 5. A stainless steel reducing cross (6–2.75 inch) now has four individual sample holders attached to a platform that rests on the bottom of a 6 inch flange. All exposed interior surfaces are coated with Teflon to provide a chemically inert surface. Four Teflon-coated aluminium discs attached to four linear translators serve as covers for each of the powdered samples. The geometric area of each of the four sample holders is 5.07 cm^2 . Since the volume of the sample holder is only about 2.5 cm^3 and the total volume is near 1500 cm^3 , no corrections are needed to account for volume change upon opening the sample compartment. The seal between the sample holders and the cover is made with Viton O-rings. With this setup, four different samples are analysed in a single run. Escape constants between 0.05 and 0.50 s^{-1} are used in these experiments.

The multisample Knudsen cell reactor is also coupled to a quadrupole mass spectrometer (UTI DetecTorr II). The mass spectrometer is housed in a vacuum chamber equipped with a 400 L s^{-1} ion pump and an ion gauge (both from Varian). The region between the quadrupole mass spectrometer and the Knudsen cell reactor is pumped by a 150 L s^{-1} turbomolecular pump (Leybold) for differential pumping of the mass spectrometer.

Samples for the Knudsen cell were prepared in one of two ways depending on how much sample was required for the experiment. For relatively large amounts of sample, typically 0.5–2.0 g, the powdered sample was spread evenly across the sample holder and then lightly pressed down to form a flat surface. When much less sample, approximately 2–100 mg, was needed, the powder was sprayed on to the sample holder. It is very important for thin samples that the powdered sample be evenly applied and it must cover the entire geometric area of the sample holder; otherwise the initial uptake coefficient may reflect the amount of unreactive and unreactive surface in the sample holder as well as the sample mass. Both of these concerns are addressed by using an atomizer to spray an aqueous slurry of the sample on to a heated sample holder. This spraying procedure ensured very even coverages of the powdered sample across the bottom of the sample holder, as determined with an optical microscope.

For all Knudsen cell experiments, flowing the reactive gas through the reactor for at least 90 min prior to the experiment passivated the walls of the reactor. The gas was introduced through a leak valve to the desired pressure as measured with an absolute pressure transducer (MKS model 690A.1TRC; range, 10^{-6} –0.1 Torr). During passivation the powdered samples were sealed with the blank flange.

The equations used to analyse Knudsen cell data can be derived by first considering the gas–surface collision frequency ω , which is given by the kinetic theory of gases as

$$\omega = \frac{\bar{c}A}{4} \frac{n}{V}, \quad (3)$$

where \bar{c} is the average molecular speed of the gas molecules, A is the area that the flux of molecules impinges upon and n/V is the number density of the reactant gas. In turn, the number density within the Knudsen cell is a function of the average molecular speed, the flow F of molecules out of the cell and the area A_h of the exit aperture:

$$\frac{n}{V} = \frac{4F}{A_h \bar{c}}. \quad (4)$$

To determine the flux of molecules to the sample in a Knudsen cell, $A = A_s$ is the geometric area of the sample holder. Substituting this and equation (4) into equation (3) gives

$$\omega = \frac{FA_s}{A_h}. \quad (5)$$

It is useful to determine the uptake coefficient γ which is simply a measure of how likely the molecule will be taken up by the surface, through either adsorption or reaction, on a per collision basis. It is defined by

$$\gamma = \frac{\text{number of molecules lost from the gas phase per second}}{\text{total number of gas-surface collisions per second}}. \quad (6)$$

Knudsen cells can be designed so that there is minimal volume change when the sample compartment is opened. In addition, since the flow of molecules into the cell does not change when the sample compartment is opened, the number of the reactant molecules that are ‘lost’ to the surface is equal to the flow change $F_0 - F$ out of the cell where F_0 and F represent the gas-phase flow out of the cell with the

sample covered and exposed respectively. Combining this with equation (5), it is possible to rewrite equation (6) as

$$\gamma = \frac{A_h F_0 - F}{A_s F}. \quad (7)$$

Equation (7) is the standard (steady-state) Knudsen cell equation used for determining heterogeneous uptake coefficients and reaction probabilities. Since the measured quantity is usually the mass spectral intensity of the reactant gas and this value is directly proportional to the flow out of the cell, equation (7) usually appears as

$$\gamma = \frac{A_h I_0 - I}{A_s I}. \quad (8)$$

Here I_0 and I are the mass spectral intensities measured with the sample covered and exposed respectively. For reasons described below, the uptake coefficient calculated using equations (7) and (8) will be referred to as the observed uptake coefficient γ_{obs} .

It is informative to consider the assumptions inherent in deriving equations (7) and (8). In setting $A = A_s$ in equation (5), it is assumed that each time that a gas-phase molecule approaches the sample it collides only once and only with the top layer. If the sample were a liquid or a single crystal or even a porous sample with an uptake coefficient approaching unity, this assumption probably would not introduce any substantial error. For powdered samples with uptake coefficients much less than unity, both of these assumptions are clearly oversimplifications whose effects must be carefully considered if true uptake coefficients are to be extracted from the data. However, correcting the observed uptake coefficient, and in particular the initial uptake coefficient, for this increased surface area requires an understanding as to how much of the powdered sample is probed by the gas phase during the time scale of the measurement.

Keyser, Moore, and Leu (KML) (1991) adapted a model from the heterogeneous catalysis literature (Aris 1975) to explain heterogeneous reactions of atmospheric relevance. The model takes into account gas diffusion into the underlying layers of a porous sample by considering the surface area contribution from both the first layer (external) and the underlying layers (internal) of particles in determining uptake coefficients. As the earlier work includes a complete set of justifications and derivations (Aris 1975, Keyser *et al.* 1991) that has been summarized in other publications (Fenter *et al.* 1996, Underwood *et al.* 2000) the details will not be presented here. The premise of the model is that the true uptake coefficient γ_t can be thought of in terms of external and internal components (figure 6) which are related to the observed uptake coefficient γ_{obs} by the following equation:

$$\gamma_{\text{obs}} = \gamma_t \frac{S_e + \eta S_i}{A_s} \quad (9)$$

where

$$\eta = \frac{1}{\phi} \tanh(\phi)$$

and

$$\phi = \frac{m}{\rho_b A_s d} \frac{3\rho_b}{2(\rho_t - \rho_b)} (3T\gamma_t)^{1/2}.$$

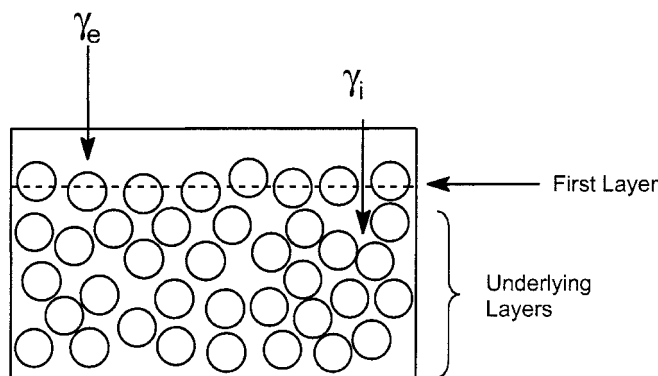


Figure 6. Graphical representation of a powdered sample in the sample holder compartment. External and internal contributions to γ_{obs} are indicated by γ_e and γ_i respectively. Because the sample holder is of fixed geometry, increasing the mass of the sample increases the sample thickness and thus the number of layers of particles.

The term $(S_e + \eta S_i)/A_s$ is a correction factor for the effect of gas-phase diffusion into the underlying layers. S_e and S_i are the internal and external surface areas respectively, A_s is the geometric area of the sample holder and η is a calculated 'effectiveness factor'. The effectiveness factor is the fraction of the internal area that contributes to the measured value of the uptake coefficient. Its value is mass (sample thickness) dependent and is determined from the relative rates of surface adsorption and diffusion into the underlying layers. Because of inhomogeneities in the interparticle voids, however, the effective diffusion constant is less than would be calculated assuming diffusion through long straight capillaries. This effect is accounted for by incorporating a tortuosity factor τ . Porous solids have predicted τ values in the range 1–8; however, most porous solids, especially powders, are not characterized well enough for an accurate calculation of τ to be made; thus, τ must be experimentally determined.

The form of the equation that we use in our studies is somewhat modified from the work by others in that here we do not assume either sc or hcp packing. Instead, the experimentally measured bulk density was used in the calculations. In addition, the specific BET surface area was measured rather than calculated. Rewriting equation (9) in terms of measured bulk density and BET surface area yields

$$\gamma_{\text{obs}} = \gamma_t \rho_b S_{\text{BET}} (h_e + \eta h_i), \quad (10)$$

where S_{BET} is the BET specific surface area, h_e is the height of the first layer and h_i is the height of all the internal layers calculated from the total mass, the measured bulk density and the particle mass. Computer simulations of the KML model shown in figure 7 demonstrate the effect that these different parameters have on the mass dependence of the observed uptake coefficient. Because of the fixed geometry of the sample holder, increasing the mass of the sample increases the sample thickness and thus the number of layers of particles. It can be seen that γ_{obs} is a function of sample mass (i.e. number of layers of particles) in each of the simulations and its value depends on the true uptake coefficient, the size and BET area of the powder, the powder density, and the tortuosity. The parameters used in the model are given in the figure caption.

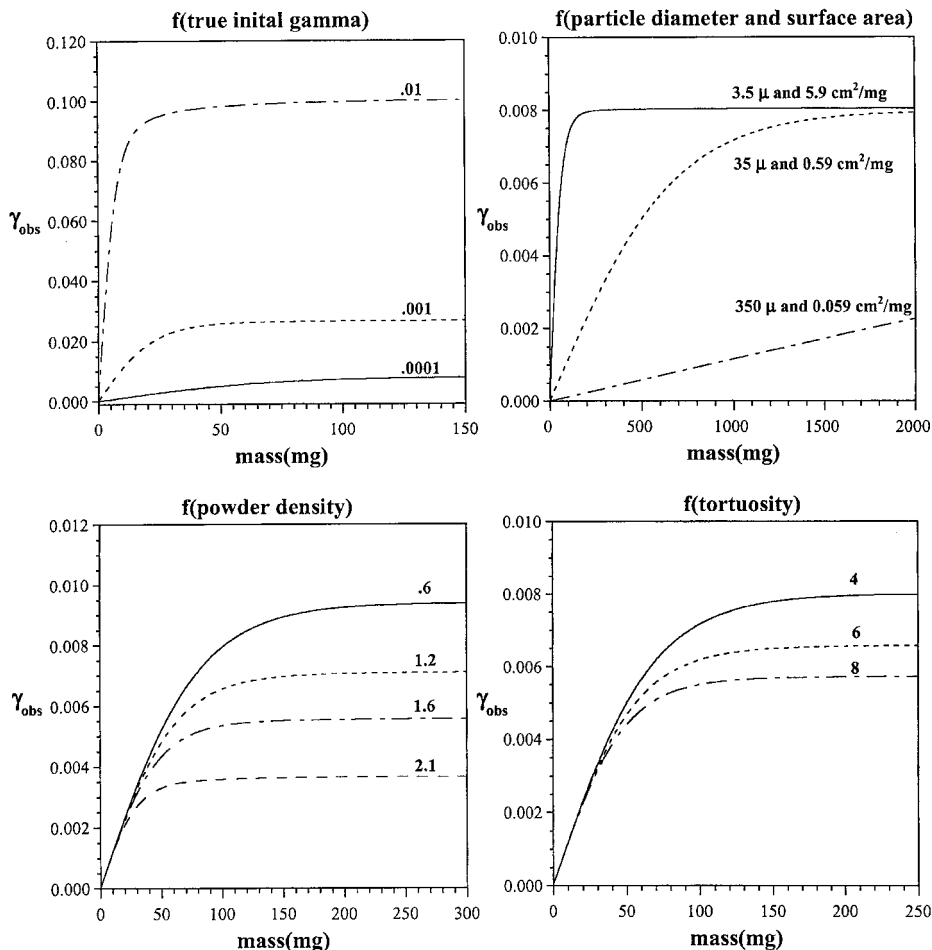


Figure 7. Plots of γ_{obs} versus mass (or sample thickness) expected for powdered samples. The KML model is used to simulate the γ_{obs} versus mass curves. The simulations show the expected changes in the shape of these curves as a function of the true initial gamma, surface area, tortuosity and powder density. Unless otherwise noted, the following parameters are used in the simulation: true initial uptake coefficient $\gamma_{0,t} = 1 \times 10^{-4}$; tortuosity $\tau = 2$; bulk density $\rho_b = 0.96 \text{ g cm}^{-3}$; true density $\rho_t = 2.93 \text{ g cm}^{-3}$; particle diameter $d = 3.5 \times 10^{-4} \text{ cm}$; surface area of the powder, $S_{\text{BET}} = 5.9 \text{ cm}^2 \text{ mg}^{-1}$.

It is important to note the two regimes evident in these curves. The first regime is seen at low masses. In this regime, the observed initial uptake coefficient has a linear dependence on the sample mass and the number of particle layers. This linear dependence arises because, for very thin samples, the probe or interrogation depth of the reactant gas molecules is greater than the depth of the powdered sample and the entire sample can be accessed on the time scale of the measurement; this time scale is of the order of seconds. In this situation, the entire sample area contributes to the observed uptake coefficient and extracting the true uptake coefficient from the observed uptake coefficient requires consideration of both the entire reactive area and the resultant increase in the number of collisions that a molecule makes within the depth of the powdered sample. As shown below, this leads to a very simple

correction factor that will work for any adsorbate–powder system for which this linear mass regime can be measured. The second regime occurs at higher masses and is termed the plateau regime. In the plateau regime, the value of γ_{obs} is independent of sample mass. This independence of sample mass arises because in the plateau regime the gas molecules only diffuse through a portion of the powder on the time scale of the measurement. It is obvious from these curves that, when no mass dependence is reported in these types of experiment, it is because the experiments are being carried out in the plateau region. It can be seen in the simulations that the extent of the linear regime depends on the value of the true uptake coefficient, the particle size and BET area, the powder density and the tortuosity whereas the slope of the linear regime depends only on the true uptake coefficient and the size and surface area of the particles.

These two regimes have been observed in kinetic measurements of the heterogeneous uptake coefficient measured for NO_2 , HNO_3 , sulphur dioxide (SO_2) and carbonyl compounds on oxide, carbonate, soot and authentic dust samples. Two examples of this type of experimental data measured in our laboratory are shown in figure 8 for the heterogeneous uptake of NO_2 on ferric oxide ($\alpha\text{-Fe}_2\text{O}_3$) and HNO_3 on magnesia (MgO). The data shown in figure 8 have been fitted to the KML model (solid curve). The parameters used in the simulation are given in the figure caption. One problem with the KML model is that there are two fitting parameters: the true uptake coefficient and the tortuosity.

As briefly mentioned, there is a simple way to determine the true uptake coefficient using a simple correction factor that will work for any gas–powder system in which the linear mass regime can be measured. In the linear region the incoming molecules can access all the particles and a correction for the ‘internal’ collisions in the lower layers of the powdered sample must also be found. In this way, the observed uptake coefficient γ_{obs} can be broken down into two components: one from the reaction with the external area, γ_e , and the other from the reaction with the internal surface area, γ_i .

The geometric area A_s of the sample holder is equivalent to the area A_p of the top layer of particles projected on to the top layer plane plus the area A_v of the voids:

$$A_s = A_p + A_v. \quad (11)$$

The ratio A_v/A_s , which is defined as the pore ratio X , is the fraction of the surface that is ‘open’. It is equal to 9.3% for hcp particles and 21.5% for ccp particles. Frequently, however, especially for very small particles, neither close-packed arrangement is achieved and the surface pore ratio is even higher. Thus, it is not surprising that diffusion into the underlying layers is a facile and significant process. The net effect is that molecules that approach the surface are likely to enter the underlying layers where they will make many collisions with the sample before they are adsorbed or exit the sample. These extra collisions will significantly amplify the observed uptake coefficient. As shown below, extracting true uptake coefficients from observed uptake coefficients is then a matter of determining the amplification in γ_{obs} brought about by the extra collisions with the underlying layers.

Since the Knudsen cell dimensions are substantially less than the mean free path of the molecules in the chamber, homogeneous gas-phase collisions are extremely rare and can be neglected. This is known as the Knudsen flow regime and under these conditions the average number Z of collisions that a particle makes before exiting the cell is independent of the cell’s configuration and equal to the inverse of

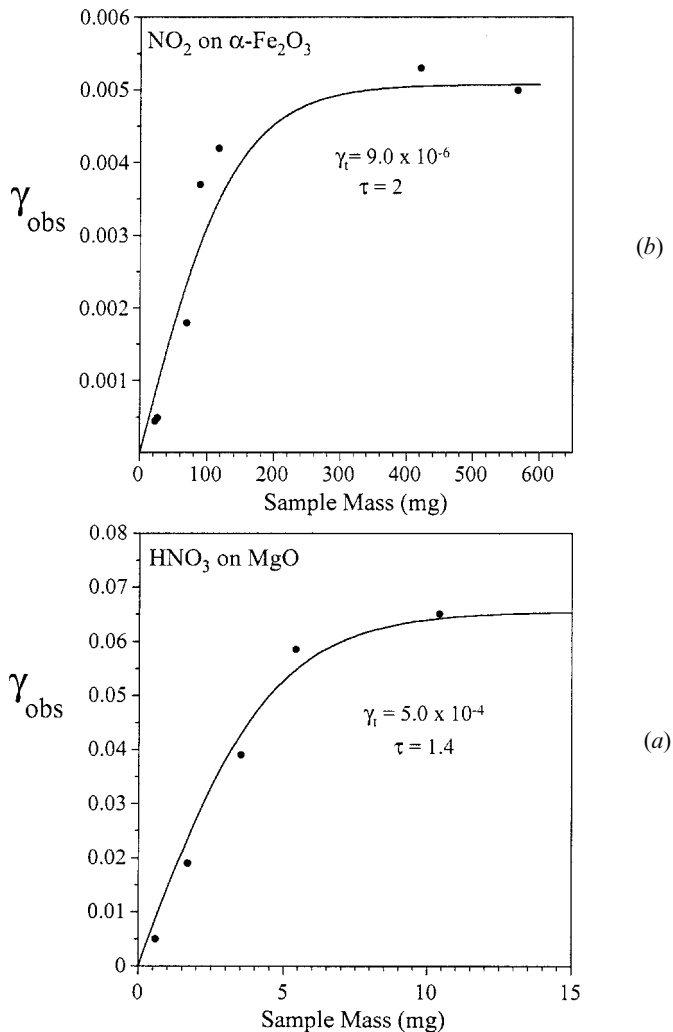


Figure 8. The initial uptake coefficients for (a) HNO_3 on MgO and (b) NO_2 on $\alpha\text{-Fe}_2\text{O}_3$ measured as a function of sample mass: (—), results of the KML model using the following experimental and fitting parameters. For HNO_3 uptake on MgO , the experimental parameters are the bulk density of the powder, $\rho_b = 0.69 \text{ g cm}^{-3}$, the true density $\rho_t = 3.58 \text{ g cm}^{-3}$, the particle diameter $d = 2 \times 10^{-4} \text{ cm}$, the surface area of the powder, $S_{\text{BET}} = 150 \text{ cm}^2 \text{ mg}^{-1}$ and the fitting parameters are the tortuosity $\tau = 1.4$ and the true initial uptake coefficient $\gamma_{0,t} = 5 \times 10^{-4}$. For NO_2 on $\alpha\text{-Fe}_2\text{O}_3$, the experimental and fitting parameters are $\rho_b = 1.1 \text{ g cm}^{-3}$, $\rho_t = 5.2 \text{ g cm}^{-3}$, $d = 2 \times 10^{-4} \text{ cm}$, $S_{\text{BET}} = 18 \text{ cm}^2 \text{ mg}^{-1}$, $\tau = 2$ and $\gamma_{0,t} = 9 \times 10^{-6}$.

the fractional probability of colliding with the escape aperture. Thus, Z is equivalent to the total interior surface area A_{cell} of the cell divided by the area A_h of the escape aperture. Additionally, if there were more than one escape aperture, the areas would be additive and Z would be equal to $A_{\text{cell}}/(A_{h1} + A_{h2} + A_{h3} + \dots)$.

Since the dimensions of the interparticle void space are much smaller than those of the Knudsen cell, and the pressure inside these voids must be less than or equal to that in the cell, the gas flow inside the powdered sample must also be in the Knudsen

flow regime. Therefore, the entire sample can be thought of as a virtual Knudsen chamber with the ‘holes’ between particles in the top layer acting as escape apertures and the internal area acting as the cell walls. The average number Z of collisions for a molecule in this virtual chamber will be

$$Z = \frac{\text{total interior area of cell}}{\text{total void area of top layer}} \quad (12)$$

$$= \frac{A_{\text{BET}} - \frac{1}{2}A_{\text{top}} + A_s + A_{\text{sw}}}{XA_s} \quad (13)$$

$$\approx \frac{A_{\text{BET}}}{XA_s}, \quad (14)$$

where A_{BET} is the total BET surface area ($S_{\text{BET}} \times \text{mass}$), $\frac{1}{2}A_{\text{top}}$ is the external area of the topmost layer, A_s is the area of the bottom of the sample holder, A_{sw} is the covered area of the sample compartment walls (sample depth $\times 2\pi R$) and XA_s equals the void area A_v . The simplifications made in going from equation (13) to equation (14) arise because the BET area generally dominates the other areas.

With the average number of collisions known, the relationship between γ_t and γ_{obs} can be derived. As an experiment starts, the number of gas-phase molecules in the cell has reached steady state and the flow of reactant molecules into the cell is equal to the flow out of the cell through the escape aperture. This can be expressed as

$$F = k_{\text{esc}}n_0, \quad (15)$$

where F is the flow into the cell, k_{esc} is the escape rate constant and n_0 is the steady-state number of gas molecules in the cell prior to opening the sample compartment.

When the sample compartment is opened, the sample acts as an additional sink, causing the pressure to drop. As the active sites on the sample become blocked, the pressure will stop dropping and start to return to its original value. Temporarily then, the cell is again in a steady state and the flow in is equal to the flow out minus the loss to the sample. This can be expressed as

$$F = k_{\text{esc}}n_r + k_e n_r + k_i n_r. \quad (16)$$

In equation (16), n_r is the steady-state number of gas molecules in the cell with the sample compartment open, and k_e and k_i are the reactive rate constants for loss to the external and internal sample surfaces respectively.

Since the flow into the cell does not change during the experiment, equation (15) can be set equal to equation (16) to yield

$$k_e + k_i = k_{\text{esc}} \frac{n_0 - n_r}{n_r}. \quad (17)$$

Since the rate constants in equation (17) will vary with the reactor geometry, it is convenient to express them in terms of the uptake coefficient through the following general equation:

$$\gamma_t = \frac{k}{\omega AZ}, \quad (18)$$

where k (s^{-1}) is a first-order rate constant, ω ($\text{s}^{-1} \text{cm}^{-2}$) is the flux of gas-phase molecules to the area A (cm^2) of interest and Z is the average number of collisions that the molecule makes with area A . Solving equation (21) for k_{esc} , k_e and k_i yields

$$k_{\text{esc}} = \omega A_{\text{h}}, \quad (19)$$

$$k_{\text{e}} = \omega A_{\text{p}} 2\gamma_{\text{t}}, \quad (20)$$

$$k_{\text{i}} = \omega A_{\text{v}} \frac{A_{\text{BET}}}{A_{\text{v}}} \gamma_{\text{t}}. \quad (21)$$

In equation (19), for the exit aperture, Z and γ have both been set equal to 1; for the external component (equation (20)), A is equal to A_{p} and Z has been set to $2\pi r^2/\pi r^2 = 2$. Similarly, for the internal component, $A = A_{\text{v}}$ and, as determined above, Z is equal to $A_{\text{BET}}/X A_{\text{s}} = A_{\text{BET}}/A_{\text{v}}$. Now, substituting equations (19), (20) and (21) into equation (17) yields

$$\gamma_{\text{t}} = \frac{A_{\text{h}}}{2A_{\text{p}} + A_{\text{BET}}} \frac{n_0 - n_{\text{r}}}{n_{\text{r}}}. \quad (22)$$

Since $A_{\text{BET}} \gg A_{\text{p}}$ and n is directly proportional to the experimentally observable mass spectral intensity I , equation (22) can be rewritten as follows:

$$\gamma_{\text{t}} = \frac{A_{\text{h}}}{A_{\text{BET}}} \frac{I_0 - I_{\text{r}}}{I_{\text{r}}} = \frac{A_{\text{s}}}{A_{\text{BET}}} \gamma_{\text{obs}}. \quad (23)$$

Equation (23) gives a simple correction factor with which the true uptake coefficient, corrected for multiple collisions with the entire BET sample area, can be extracted from the observed value, which assumes no diffusion into the underlying layers. Not surprisingly the correction factor, like the number of collisions, scales with the BET area. It is interesting to note that both A_{p} and A_{v} cancel out during the derivation and the density of the powder is unimportant in the linear regime.

A final consideration sometimes ignored in the analysis of Knudsen cell data is that of site blocking. If the impingement rate of the reactant molecules is too high, the incoming gas molecules may start to saturate the limited amount of reactive sites before the first data point is collected, this is especially true when γ is high. If the reacted sites passivate the surface to further reaction, the measured uptake coefficient will be artificially lowered because the measured value for γ will reflect collisions with both active (empty) sites and occupied sites. If the occupied sites can undergo further reaction, the subsequent reaction will almost certainly have a different uptake coefficient. As such, the measured value will be skewed to higher or lower values depending on the relative values of the two reaction probabilities. In either case, the effect will be manifest as a pressure dependence in the observed uptake coefficient. This 'limited accommodation' effect can be avoided experimentally by reducing the impingement rate (or pressure), by reducing the data acquisition time, or by a combination of the two. Of course there is a trade-off here in that, as the pressure is reduced, so is the signal intensity and thus a compromise must be struck to achieve reasonable signal-to-noise ratios.

In fundamental studies of sticking coefficients on single-crystal surfaces in ultrahigh vacuum, site-blocking effects can be avoided by limiting the number of reactant molecules colliding with the sample (King and Tomkins 1968). Over the time period of a single data acquisition point, less than 10% of the total number of surface sites should be occupied (King and Tomkins 1968). For a 10 cm^2 sample, the number of surface sites available for reaction is about $5 \times 10^{14} \text{ sites cm}^{-2} \times 10 \text{ cm}^2 = 5 \times 10^{15}$ sites and the data acquisition time is approximately 0.5 s; this impingement rate would be $(0.1 \times 5 \times 10^{15})/0.5 = 10^{15} \text{ molecules s}^{-1}$. This impinge-

ment rate corresponds to a maximum pressure of about $3 \mu\text{Torr}$ as determined from equation (2) and ideal-gas behaviour. This calculation is based on an assumed uptake coefficient of 1.0; a lower value would both fill the available sites more slowly and yield a greater effective diffusion coefficient which would allow the reactant to probe a greater number of surface sites. As a result, for a given sample-reactant combination, the upper limit of the impingement rate is likely to be greater than the value resulting from the simple calculation above. However, if the chemistry is mediated by defect sites, the active site density will be substantially lower than $5 \times 10^{14} \text{ sites cm}^{-2}$ and the impingement rate will need to be reduced to avoid the effects of limited accommodation. Thus, unless the microscopic details of the reaction are known, the maximum impingement rate that will yield a pressure-independent uptake coefficient will have to be experimentally determined. If that value cannot be determined or cannot be reached experimentally, or if the environmentally relevant pressure of the reactant gas is greater than that value, then the pressure dependence should be considered before the reported values are incorporated into atmospheric chemistry models.

2.3.2. Kinetic measurements utilizing transmission infrared spectroscopy

A major limitation of the Knudsen cell reactor is that experiments can only be made under dry conditions. In order to investigate heterogeneous reaction rates under conditions of relative humidity closer to that of the troposphere, time course FTIR measurements have been made. As discussed in the last section, for heterogeneous reactions, the uptake of a gas on a solid is most often quantified in terms of an uptake coefficient or reaction probability γ . This can be written as the rate of adsorption divided by the gas-phase collision rate and is given as

$$\gamma = \frac{dN_a/dt}{\text{flux}}, \quad (24)$$

where the numerator in this case is the rate of formation of surface-bound species on the surface of the particles in units of molecules per square centimetre per second and the denominator is the flux or collision rate per unit area in units of molecules per square centimetre per second. The flux is calculated according to the kinetic theory of gases:

$$\text{flux} = \frac{PN}{(2\pi MRT)^{1/2}}, \quad (25)$$

where P is the pressure of the gas, N is Avogadro's number, M is the molecular weight of the gas, R is the gas constant and T is the temperature. The first-order rate of formation of surface-bound species on the oxide particles upon reaction with a gas can be described by the rate law

$$\frac{dN_a}{dt} = k_a(1 - \theta)N_sP, \quad (26)$$

where dN_a/dt is the rate of formation of surface-bound species, k_a is the rate constant of adsorption, $1 - \theta$ is the number of sites on the particles available for adsorption and $\theta = N_a/N_s$, with N_s the saturation coverage on the oxide particles and P the pressure of the gas. As previously discussed with respect to kinetic measurements on the heterogeneous uptake of NO_2 on NaCl (Vogt and Finlayson-Pitts 1994, Peters and Ewing 1996) and alumina (Al_2O_3) (Borenson *et al.* 2000), if the

pressure P is constant and the number $1 - \theta$ of sites on the oxide particles is large compared with the number θ of surface-bound species formed then the rate dN_a/dt of formation of surface-bound species on the oxide particles upon reaction with HNO_3 vapour is proportional to the slope of a plot of N_a versus time.

2.3.3. Aerosol reaction chamber

The two methods discussed above, namely Knudsen cell reactor and time-course FTIR experiments of the formation of surface-bound species, are carried out using bulk powdered samples. In order to measure the rates of heterogeneous reactions of aerosols, an aerosol reaction chamber has been recently designed and constructed. In these studies, a well-characterized powder sample is suspended in a chamber and mixed with the reactive gas of interest in a humidity-controlled atmospheric pressure environment. Subsequent chemistry is monitored by FTIR and UV-visible absorption spectroscopy, and a fast-sampling quadrupole mass spectrometer. More sensitive laser-based probe techniques can also be applied, when appropriate. The aerosol and reagent gas concentrations are adjusted to yield a time scale for reaction that is compatible with the sensitivity and time resolution of the probe methods. Use of a suspended aerosol will circumvent problems associated with studying particles in bulk powder form. Mass transport phenomena in the chamber will closely mimic the situation in the actual atmosphere.

A schematic diagram of the recently constructed aerosol reaction chamber is depicted in figure 9. The stainless steel chamber has a total volume of 151 L and a surface-to-volume ratio S/V of 11 m^{-1} . All the interior surfaces of the aerosol

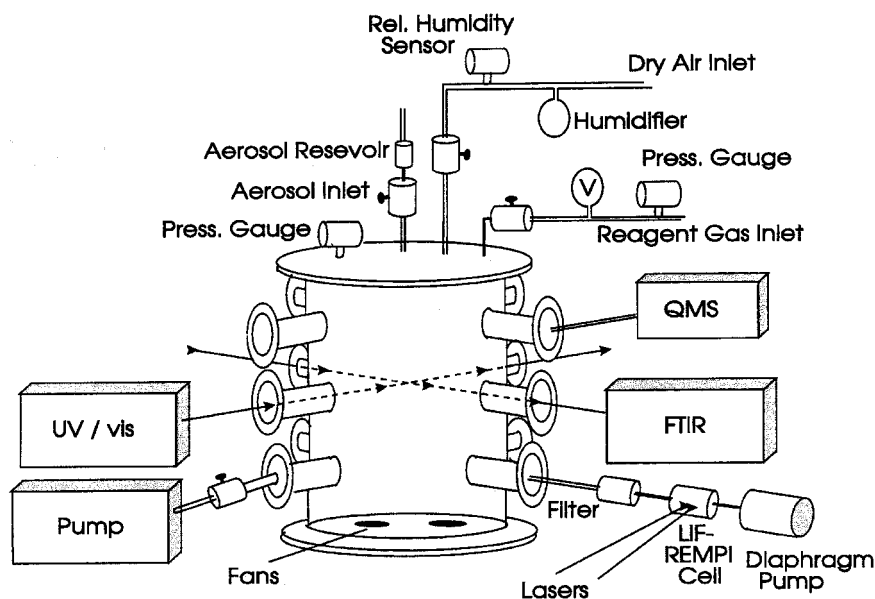


Figure 9. A schematic diagram of the aerosol reaction chamber that has been recently constructed to measure heterogeneous uptake coefficients on suspended particles. A variety of spectroscopic techniques can be used in these studies including laser-based techniques: QMS, quadrupole mass spectrometry; FTIR, Fourier transform infrared technique; LIF-REMPI cell, LIF resonance-enhanced multiphoton ionization cell; UV/vis, UV-visible spectroscopy.

reaction chamber are Teflon coated to inhibit wall reactions. One set of side arms is sealed with quartz windows and mounts to hold fibre-optic collimators for the UV-visible spectrometer (Ocean Optics model SD2000). The spectrometer has two identical charge-coupled device array detectors (2048 elements; approximately 1.3 nm resolution) so that broad-band (220–800 nm) dual-beam spectra may be recorded in real time. Data collection times as fast as 5 ms for the entire wavelength range are achievable. Perpendicular to the UV-visible probe beam path are side arms holding the IR windows for the FTIR spectrometer (Mattson Infinity 60AR; 0.125 cm⁻¹ resolution). A high-speed data transfer connection to the controlling personal computer permits a time resolution of the order of a 1–3 min with good signal-to-noise ratio for lower resolution (approximately 1 cm⁻¹) spectra. Germanium windows are employed instead of salt windows so that reactions do not occur on the windows with gases such as HNO₃. Another port is connected to the capillary sample inlet of the quadrupole mass spectrometer (SRS model QMS200). The use of a capillary and differential pumping permit the spectrometer to sample at atmospheric pressure while maintaining a time response of less than 200 ms. Spectroscopic and mass spectrometric sensitivities are characterized by measuring signals from a known concentration of reagent gas. An absolute pressure transducer (MKS) is used to calibrate quantitatively the response of our instruments to reactants and products.

Sample gas is prepared in a separate sample vacuum line attached to the main chamber. A calibrated plenum volume and an accurate pressure gauge will be used to deliver known quantities of reagent gas to the reaction chamber. Dried air for the chamber is provided by a commercial filtration system and will be rehumidified to the desired RH prior to flushing and filling the chamber. The chamber temperature is measured with thermocouples and controlled in the range 220–300 K with an external cooling jacket. The chamber pressure is also monitored with a capacitance manometer. The reagent gas and humidified air are allowed to mix in the chamber. The influence of wall reactions are quantified by detecting loss of reagent species in the absence of added particulate. In some cases, it may be necessary to passivate the chamber prior to making kinetic measurements. A precisely weighed aerosol sample is placed in an antechamber connected to the main chamber by a large-bore valve. The aerosol is also exposed to the humidified air flow for a sufficient time for the surface-adsorbed H₂O to reach equilibrium saturation. The antechamber is then pressurized prior to opening the valve and rapidly injecting the aerosol powder into the reaction vessel. Turbulent mixing results from the injection of the aerosol sample. The decay and growth of gas-phase species are monitored with the probe techniques described above. The time resolution is limited by the time required for mixing, which will be of the order of minutes.

The adsorption rate constant can be determined by measuring the first-order exponential decay of the gas phase at low coverages such that the approximation $1 - \theta = 1$ is good. The first-order rate constant can be expressed as follows;

$$k_a = \frac{\bar{c}\gamma S}{4V} = \frac{\bar{c}\gamma S_{\text{BET}} \times \text{mass}}{4V}, \quad (27)$$

where \bar{c} is the average molecular velocity of the gas-phase species and $S_{\text{BET}} \times \text{mass} = N_s$, the number of surface sites per area of aerosol surface. The value of γ calculated from equation (27) using the experimentally determined rate constant k_a depends critically on the specific surface area measured for a given aerosol sample.

2.4. Atmospheric chemistry models and equations used in the box-model analysis

To study the interactions between aerosols and the photochemical oxidant cycle it is necessary to treat particles and the gas-phase chemistry processes in a coupled fashion. Zhang *et al.* (1994) and Zhang and Carmichael (1999) have developed a combined aerosol–gas-phase chemistry model for this purpose, in which the detailed multicomponent aerosol dynamics and heterogeneous chemistry on the aerosol surface are explicitly included in the model formulation. It is their model and modelling analysis that are described here. In the model, aerosol interactions with the photochemical oxidant cycle arise through the sorption of trace species and the gas-to-particle conversions of nitrogen and sulphur species during the aerosol growth and surface heterogeneous reaction processes. Gas-to-particle conversion, coagulation and deposition are important dynamic processes that are also treated. Box model simulations were performed using the gas phase mechanism that is in the STEM-II model (Carmichael *et al.* 1991). The gas-phase chemical mechanism is based on that of Lurmann *et al.* (1986) but has been modified to include low-NO_x conditions and an explicit treatment of isoprene. It consists of 83 chemical species and 185 gas-phase reactions. The effect of aerosol on the actinic flux is also included in the analysis through the use of a two-stream radiation model (Crist *et al.* 1996, Hotchkiss 1996).

The interactions between the gas and aerosol phases were modelled using the kinetics approach. This approach has been taken by several investigators for the purpose of modelling the interaction between the gas-phase species and the dust–aerosol particles (Zhang *et al.* 1994, Dentener *et al.* 1996, Sander and Crutzen 1996, Saylor 1997). For the calculation of dC_i/dt , where C_i is the adsorbed species concentration, the following equations are used (Fuchs and Sutugin 1970, Zhang *et al.* 1994, Dentener *et al.* 1996, Saylor 1997):

$$\frac{\partial C_i}{\partial t} = \int_{r_2}^{r_1} 4\pi r^2 F(r) \frac{dn}{dr} dr, \quad (28)$$

$$F(r) = \frac{D_j(C_j - C_j^e)/r}{1 + f(K_n, \gamma)K_n}, \quad (29)$$

$$f(K_n, \gamma) = \frac{1.333 + 0.71K_n^{-1}}{1 + K_n^{-1}} + \frac{4(1 - \gamma)}{3\gamma}, \quad (30)$$

where C_j is the gas-phase concentration of the absorbing species j and C_j^e is the equilibrium gas-phase concentration of species j that would be in equilibrium with the surface-adsorbed species (this term can be related to surface coverage and surface saturation effects), D_j ($\text{cm}^2 \text{s}^{-1}$) is the gas-phase diffusion coefficient, K_n is the dimensionless Knudsen number (equal to λ/r), λ is the effective free path of a gas molecule in air, r is the particle radius, $F(r)$ ($\text{molecules cm}^{-2} \text{s}^{-1}$) is the flux of the trace species to the surface of the aerosol particle with radius r , dn/dr is the number–size distribution of aerosol particles and γ is the accommodation or uptake coefficient (sometimes denoted as α). Although it is formally possible to separate the uptake coefficient into an adsorption component and a reaction component, no such distinction is made here and γ represents the net loss to the sample as it does in the laboratory measurements.

These equations show that the molecular flux on to free-molecular-regime particles ($K_n > 10$) is proportional to the second moment of the size distribution,

whereas the molecular flux on to continuum-regime particles ($K_n < 0.1$) is proportional to the first moment. Since the aerosol size distributions used in this modelling study range from free-molecular to continuum regimes, the actual molecular flux on to aerosol particles falls between these two limits.

3. Heterogeneous uptake of NO_2 and HNO_3 on oxide and mineral dust particles

3.1. The importance of heterogeneous uptake of nitrogen oxides in the troposphere

Heterogeneous reactions that affect NO_x and HNO_3 chemistry have important implications for tropospheric chemistry. Consequently, an understanding of processes that control NO_x concentrations is key to the development of models that can accurately describe tropospheric O_3 . For example, one problem encountered by present modelling efforts that rely on gas-phase chemical processes alone is that the calculated HNO_3 -to- NO_x ratio is typically over-predicted by a factor of five to ten (Liu *et al.* 1992, Chatfield 1994, Singh *et al.* 1996). Therefore, heterogeneous processes that preferentially remove HNO_3 or recycle NO_x from HNO_3 more efficiently than HNO_3 photolysis or reactions with OH could potentially reconcile the predictions and the observations.

Dentener and Crutzen (1993) modelled N_2O_5 and NO_3 reactions on tropospheric sulphate aerosols ($\text{N}_2\text{O}_5 + \text{H}_2\text{O} \rightarrow 2\text{HNO}_3$; $\text{NO}_3 \rightarrow \text{products}$) using a three-dimensional global atmospheric chemistry model. By including these reactions on aerosols, they were better able to simulate observed nitrate wet deposition patterns. These reactions resulted in a decrease in the global average NO_x burden by 50% (80% in winter and 20% in summer). In addition, the annual global O_3 and OH burdens were lowered by about 10%, with values decreased by over 25% in the northern hemisphere in various seasons.

Very little is known about reactions of NO_x and HNO_3 on other aerosol surfaces (e.g. mineral aerosols and organic aerosols). Dentener *et al.* (1996) investigated the impact of irreversible reactions of HNO_3 , N_2O_5 , NO_3 , HO_2 , O_3 and SO_y on dust surfaces through modelling analysis. Those results illustrate that mineral aerosol may have a significant impact on the chemistry of the troposphere. In the case of sulphur, a significant fraction of sulphate is predicted to be associated with mineral aerosols. An even larger fraction of gas-phase HNO_3 may be neutralized by mineral aerosols. The regions where at least 40% of the total nitrate is found on the mineral aerosol cover vast portions of the northern and southern hemispheres. During the months of February, March and April the region covers almost all of Asia and extends throughout the central and northern regions of the Pacific Ocean basin, and the tropical and subtropical Atlantic and Indian Oceans. Only the regions of western and central Europe, the eastern parts of North and Central America, and the high latitude (above 60°) zones are predicted to have relatively small portions of HNO_3 associated with mineral aerosols. The effect of dust interactions can be intensified on regional scales during high-dust periods, where surface areas of mineral aerosols can be an order of magnitude higher than the monthly averaged values calculated by the global model (Zhang *et al.* 1994, Phadnis and Carmichael 2000).

The model calculations discussed above, while extremely valuable in assessing the potential role of heterogeneous reactions on aerosols, remain highly uncertain because there is little information on heterogeneous reaction mechanisms and reaction rates, especially for mineral aerosol surfaces (Schurath and Naumann 1998). Therefore, it is essential to determine the heterogeneous reaction chemistry

of particles present in the troposphere. In our laboratory, we have investigated the heterogeneous reactivity of NO_2 and HNO_3 on oxide particles as well as authentic mineral dust particles from desert regions. As discussed below, spectroscopic and kinetic measurements have been made in order to develop a molecular-level understanding of the heterogeneous chemistry of NO_2 and HNO_3 on mineral aerosol. The details of the laboratory investigation are then incorporated in a box model for further analysis.

3.2. Spectroscopic measurements following adsorption and reaction of NO_2 and HNO_3 on oxide particles

It is well known that NO_2 and NO can react on oxide surfaces to yield a number of different surface species that in principle can be differentiated by IR spectroscopy. NO_2 adsorption can result in the formation of both adsorbed nitrate (NO_3^-) and nitrite (NO_2^-) (Pozdnyakov and Filimonov 1973, Busca and Lorenzelli 1981, Hadjiivanov *et al.* 1994, 1995, Navio *et al.* 1996, Hadjiivanov 2000). The coordination of nitrate, nitrite and nitric oxide (NO) in inorganic complexes has been discussed in the literature in some detail and provides a useful guide for the interpretation of the IR absorption bands of adsorbed species (Nakamoto 1970, Hitchman and Rowbottom 1982, Davydov 1990).

The FTIR spectra of Al_2O_3 , Fe_2O_3 and TiO_2 following exposure to NO_2 in the pressure range 5–350 mTorr are shown in figure 10. The spectra were recorded after evacuation of gas-phase NO_2 . Single-beam spectra of the surface after exposure to NO_2 were referenced to single-beam spectra of the clean oxide prior to NO_2 adsorption. At the lowest pressures, features are apparent in the spectra which can be assigned to a chelating nitrite surface species, specifically bidentate nitrito species (table 2). These bands grow in intensity as the NO_2 pressure is increased to approximately 30 mTorr. Besides the increase in intensity of the nitrite bands with increasing NO_2 pressure, several new bands become evident in the 1650–1150 cm^{-1} region as the NO_2 pressure increases. These new absorption bands can be assigned to the ν_3 mode of oxide-coordinated monodentate, bidentate and bridging nitrate. This band is degenerate for the free nitrate ion, however, it splits into two bands upon adsorption because of a loss of symmetry. In the case of Al_2O_3 , absorptions at 1411 and 1302 cm^{-1} are also apparent in the spectra. These bands are assigned to H_2O -solvated nitrate and have been observed previously (Miller and Grassian 1998). Although the Al_2O_3 particles have been pumped overnight, there appears to be residual H_2O left on the surface.

UV–visible diffuse reflectance spectroscopy was used to provide further evidence for the identification of adsorbed products from heterogeneous reactions of NO_2 . The UV–visible spectra of nitrate and nitrite ions are well known. Both nitrate and nitrite have two electronic transitions in the 200–400 nm range (Hitchman and Rowbottom 1982). The lowest-energy transition, that is the $n \rightarrow \pi^*$ transition, is forbidden and therefore relatively weak. This transition has maxima near 300 and 350 nm for the nitrate and nitrite respectively. The next-lowest-energy transition is an allowed $\pi \rightarrow \pi^*$ transition and is therefore stronger. The absorption maxima for this transition are near 200 and 210 nm for the nitrate and nitrite ion respectively. Therefore, UV–visible diffuse reflectance spectroscopy should be useful in distinguishing between adsorbed nitrate and nitrite as the wavelength maximum for the $n \rightarrow \pi^*$ transition for nitrate and nitrite are sufficiently different that, even if there

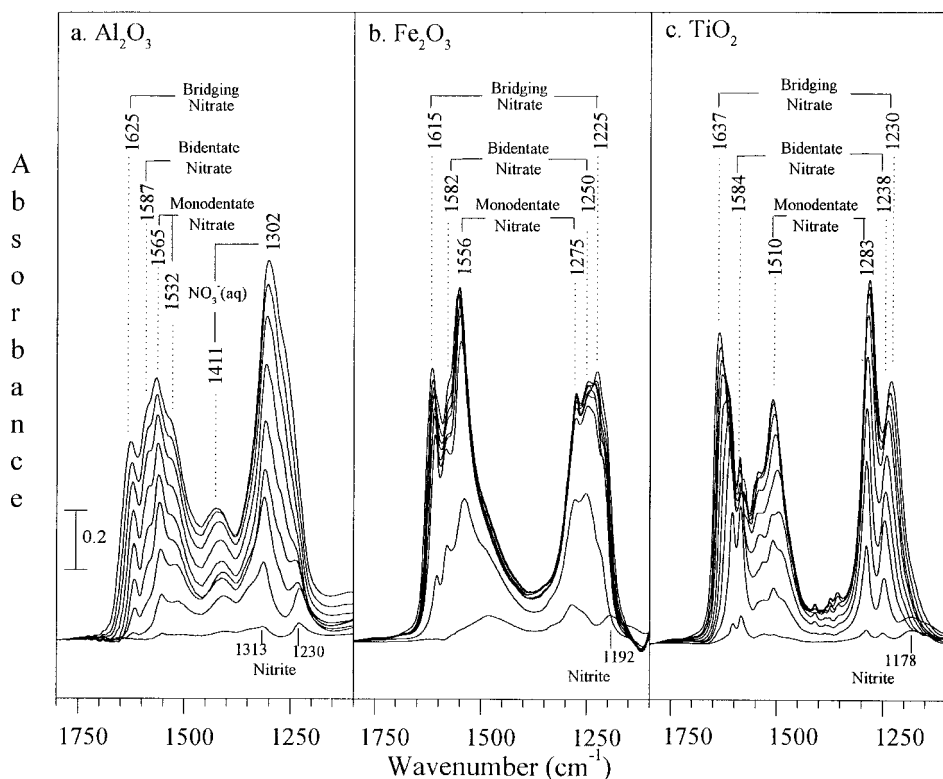


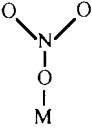
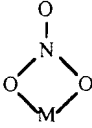
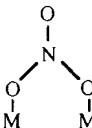
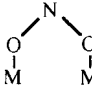
Figure 10. Transmission FTIR spectra of (a) Al_2O_3 , (b) Fe_2O_3 and (c) TiO_2 after exposure to NO_2 . The spectra were recorded after evacuation of the gas phase following exposure of the oxides to NO_2 in the pressure range 5–350 mTorr. As discussed in the text, the absorption features indicate a conversion of nitrite to nitrate as coverage increases. Nitrate is seen to adsorb in different bonding configurations. See table 2 for the assignment of the vibrational bands. (Reproduced with permission from Underwood *et al.* (1999).)

were some shift in the absorption maximum due to adsorption, there should be no ambiguity between which ion is present.

In the UV–visible experiments, the powdered sample is packed and there is limited diffusion through the packed powder. Because of this, it is difficult to know exactly how much NO_2 reaches the sample closest to the fumed SiO_2 window where the light intensity is greatest. Therefore, in these experiments, NO_2 exposures are made using higher pressures of NO_2 gas and different exposures are obtained by introducing NO_2 into the sample cell for different amounts of time.

The UV–visible diffuse reflectance spectra following NO_2 adsorption on Al_2O_3 is shown by the dotted curve in figure 11. The spectra are dependent on NO_2 exposure. Initially, there are two features in the reflectance spectra at 370 and 208 nm. As discussed above, these two features can be assigned to the $n \rightarrow \pi^*$ and $\pi \rightarrow \pi^*$ transitions of adsorbed nitrite. After longer exposures to NO_2 , the reflectivity spectrum changes and two new features are observed near 270 and 201 nm. These two features are associated with the adsorbed nitrate ion. The 270 nm band for nitrate adsorbed on Al_2O_3 is red-shifted relative to uncoordinated nitrate ions or nitrate ions in a salt environment. Thus, there is agreement between the FTIR and

Table 2. Assignment of vibrational bands of adsorbed nitrogen oxides on Al₂O₃, Fe₂O₃ and TiO₃ from NO₂ adsorption.

Surface species	Representation	Assignment	Vibrational band (cm ⁻¹)		
			Al ₂ O ₃	Fe ₂ O ₃	TiO ₂
Monodentate nitrate		ν_3 low ν_3 high	^a 1565, 1532	1275 1556	1283 1510
Bidentate nitrate		ν_3 low ν_3 high	^a 1587	1250 1582	1238 1584
Bridging nitrate		ν_3 low ν_3 high	^a 1625	1225 1615	1230 1637
Solvated nitrate	NO ₃ ⁻ (aq)	ν_3 low ν_3 high	1302 1411	1305 ^b ^c	1303 ^b 1435 ^b
Bidentate nitrito		ν_3 ν_1	1230 1313	1192 1272	1178 1286

^a Bands hidden under solvated nitrate absorption.

^b Only observed when H₂O (about 10% RH) is introduced into the IR cell.

^c High-frequency band not observed.

UV-visible results in that the predominant surface species is initially found to be adsorbed nitrite, then forming nitrate as the reaction proceeds. This is consistent with previous work in which NO₂ reaction with mineral dust particles produced adsorbed nitrate (Cunningham *et al.* 1974, Mamane and Gottlieb 1990).

The FTIR spectra following adsorption of HNO₃ on Al₂O₃, TiO₂ and Fe₂O₃ particles as a function of increasing HNO₃ exposure show the presence of surface bound nitrate, that is HNO₃ undergoes dissociation on the surface to yield adsorbed NO₃⁻ and H⁺. The proton may go on to react with hydroxyl groups on the surface to give adsorbed H₂O. There is no evidence for the formation of a nitrite species as was observed at low coverages for NO₂ adsorption nor is there evidence for the formation of any other nitrogen-containing product (Goodman *et al.* 2001). Adsorption of HNO₃ on calcium oxide (CaO) and MgO also show the presence of adsorbed nitrate.

Surface-bound species are not the only products that form from the reaction of NO₂ with mineral oxide surfaces. For each pressure to which the oxides were exposed, FTIR spectra of the gas phase were also taken. The spectra of the gas phase in the region from 1800 to 2300 cm⁻¹ and at a pressure of approximately 300 mTorr are shown in figure 12. The gas-phase IR data show that significant amounts of NO and, in the case of Al₂O₃, some N₂O are present in the IR cell. No other gas-phase

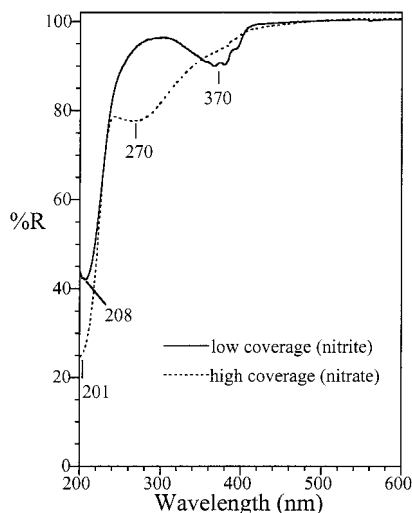


Figure 11. UV-visible diffuse reflectance spectra of Al_2O_3 as a function of NO_2 exposure. In the initial spectrum (—), there are two features in the reflectivity spectrum at 370 and 208 nm after NO_2 adsorption. These two features in the reflectivity spectra are characteristic of nitrite absorptions, similar to nitrate absorptions, there is an $n \rightarrow \pi^*$ transition at lower energies and a more intense $\pi \rightarrow \pi^*$ transition at higher energies. At higher NO_2 exposures (-----), a decrease in the reflectivity spectrum is seen at 270 and 201 nm. These are due to absorptions from adsorbed nitrate on the Al_2O_3 surface.

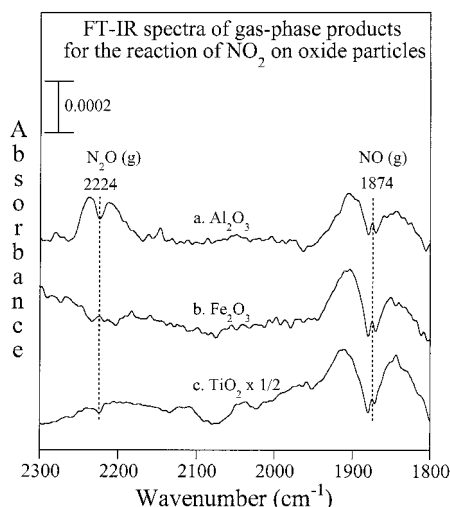


Figure 12. Transmission FTIR spectra of the gas-phase products formed from reaction of NO_2 on the surface of Al_2O_3 particles (curve a), Fe_2O_3 particles (curve b) and TiO_2 particles (curve c) at an ambient pressure near 300 mTorr. Two gas-phase products are present: NO at 1874 cm^{-1} and N_2O at 2224 cm^{-1} .

products were detected. As measured in our laboratory, the extinction coefficient of N_2O is approximately 20 times that of NO . From this we estimate that N_2O accounts for less than 1% of the gas-phase products, even for Al_2O_3 . Experiments where NO_2 was added to the FTIR cell in the absence of mineral oxides also show some NO and N_2O formation; however, the amount formed is much less than when the mineral

oxide particles are present. These control experiments show that wall reactions do occur but only account for a small fraction of the gas-phase products. Because of these small but non-negligible wall reactions, and the large disparity in extinction coefficients it is difficult to quantify the amount of NO and N₂O from the IR data. However, experiments carried out with the Knudsen cell reactor, described in the next section, can be used to quantify gas-phase product formation. No gas-phase nitrogen-containing products are found for HNO₃ uptake on the surfaces investigated.

3.3. Knudsen cell measurements of NO₂ and HNO₃ on oxide particles and authentic dust samples

Heterogeneous reaction kinetics of NO₂ and HNO₃ measured on Saharan sand, Gobi dust and six different oxide samples including SiO₂, Al₂O₃, Fe₂O₃, TiO₂, CaO and MgO. For each of the samples investigated except for SiO₂, gaseous NO₂ adsorbs on the surface, initially, without the production of gas-phase products; as the reaction proceeds concomitant with the conversion of surface nitrite to nitrate, gaseous NO₂ is reduced to gaseous NO. For each of the samples investigated, no gas-phase products are observed for the uptake of HNO₃.

Representative Knudsen cell data are presented in figures 13 (a) and (b) for the heterogeneous reaction of NO₂ on TiO₂ and on China loess from the Gobi desert region respectively. It can be seen from the data shown in figure 13 that, when the sample holder is opened, the NO₂ signal ($m/e = 46$) drops as it reacts on the surface of the particles and, when it is closed, the NO₂ flow rate returns to its original steady-state value. The sample compartment is closed intermittently over the course of the experiment to check for any baseline drift. In figure 13, the periods of time during which the sample is exposed are delineated with the rectangular boxes labelled OPEN at the bottom of each figure.

The shape of the reactivity curves obtained while the sample is open can also yield some information as to the processes taking place during reaction. For example, the data in figure 13 show a sharp drop in signal followed by a slow increase back towards the steady-state value. This behaviour can be explained as a site-blocking effect; that is, as the reaction proceeds, the number of available surface sites decreases. This reduces the probability that an incoming molecule will find an active site and thus the observed uptake coefficient decreases. This process continues until all the sites are occupied, at which point the NO₂ signal returns to its original steady-state level and further opening and closing the sample lid has no effect on the NO₂ signal. These experiments were performed at relatively high pressures (about 8 mTorr) so that saturation coverages could be determined in a reasonable amount of time.

In addition to NO₂, the mass spectrometer is also set to monitor other mass channels including NO ($m/e = 31$) and nitrous oxide (N₂O) ($m/e = 44$). Although no detectable amount of N₂O was formed, the reaction did produce gas-phase NO. Since NO⁺ is a fragment of NO₂, the NO signal was corrected for the fragmentation of NO₂. The mass spectrometer signal for NO was then converted to flow. The formation of gas-phase NO from reaction of NO₂ does not occur initially but evolves as the reaction on the surface proceeds. To facilitate the direct comparison of the NO produced to the NO₂ reacted, the NO₂ flow data were offset by the experimental steady-state value and then inverted. In this way the number of NO₂ molecules that have reacted with the surface as well as the amount of NO produced, for the

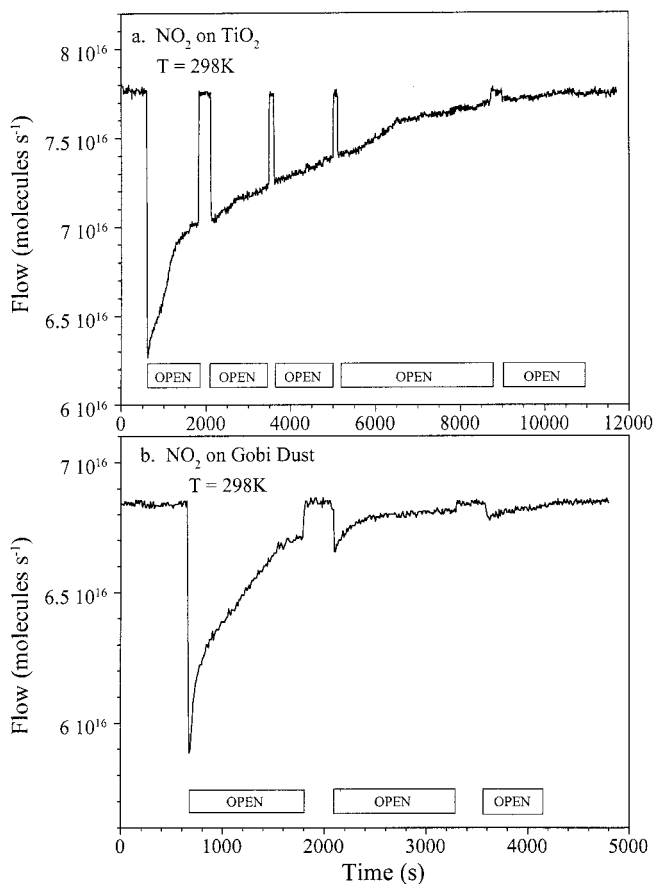


Figure 13. Representative Knudsen cell data for the heterogeneous reaction of NO₂ on (a) TiO₂ and (b) China loess from the Gobi desert region. When the sample holder is opened, the flow of NO₂ drops as it reacts on the surface of the particles and, when it is closed, the NO₂ flow rate returns to its original steady-state value. The sample compartment is closed intermittently over the course of the experiment to check for baseline drift. The rectangular boxes labelled OPEN at the bottom of each figure delineate the periods of time during which the sample is exposed to the gas.

experiments shown in figures 13 (a) and (b) have been plotted in figures 14 (a) and (b) respectively.

Several interesting and important observations can be made from the data presented in figure 14. First, there is adsorption of NO₂ before the production of gas-phase NO begins. This implies that the surface must have a minimum amount of adsorbed NO₂ before NO is produced. The experimentally determined average value for this coverage is 30%. Second, by integrating the area under the curves the total number of molecules of NO₂ reacted and NO produced during the course of the experiment can be determined. For each of the oxides studied the resultant NO₂-to-NO ratio is very close to 2 to 1. In addition, by measuring the initial sample mass and knowing the BET surface area, the total number of NO₂ molecules that react per square centimetre can be determined for each sample. As discussed in the next section, the measured value of $8.6 \times 10^{14} \text{ cm}^{-2}$, for the TiO₂ sample implies a surface nitrate coverage of $4.3 \times 10^{14} \text{ cm}^{-2}$. Similar coverages were determined for all the

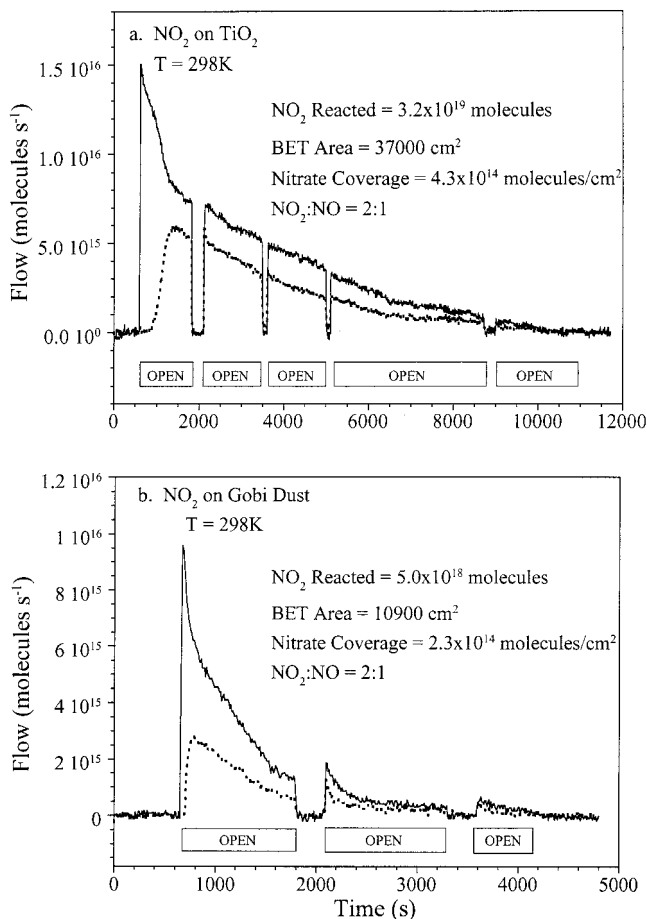
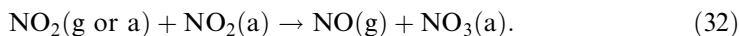


Figure 14. The number of NO₂ molecules that have reacted with the surface as well as the number of NO molecules produced are shown as a function of time, for the experiments shown in figures 13(a) and (b) respectively. As can be seen, the formation of gas-phase NO does not occur initially but evolves as reaction on the surface proceeds. Reaction stoichiometry and coverage information are determined from integration (see text for further details).

oxides studied with the coverages of the authentic dust samples being slightly lower. Perhaps most importantly, this demonstrates that using the geometric area of the sample compartment would give physically unreasonable values for the surface nitrate coverage, that is about 10¹⁸ cm⁻². This observation provides definitive evidence that there is gas diffusion into the underlying layers of the oxide particles.

The Knudsen cell data for heterogeneous reactions of NO₂ on mineral oxides can be summarized as two reactions:



As the coverage on the surface increases, nitrate forms concurrent with the production of gaseous NO from reaction of two nitrite species or nitrite plus gas-

phase NO_2 as shown in reaction (32). Thus, NO_2 undergoes a stepwise disproportionation reaction on the surface to yield surface nitrate and gas-phase NO . The reaction of NO_2 on oxide particles is stoichiometric and not catalytic. A recent study investigating the heterogeneous reaction of NO_2 on Al_2O_3 particles confirms our observation that surface nitrite is converted to nitrate as the reaction proceeds (Borensen *et al.* 2000).

As discussed in section 2.3.1, the observed uptake coefficient γ for sufficiently thin powdered samples shows a linear dependence on sample mass. The linear mass-dependent regions of the observed initial uptake coefficients for NO_2 on the authentic dust and mineral oxide samples studied were examined (Underwood *et al.* 2001). All these experiments were carried out at a much lower pressure, of the order of $4 \mu\text{Torr}$. In each case the observed initial uptake coefficients are plotted as a function of sample mass together with a linear least-squares fit to the data of the form $y = mx$ so that the fit is forced through the origin. Efforts were made to replicate precisely experimental conditions such as pump-down time, background levels and operating pressure for each experiment. This was necessary to achieve the high correlation coefficients (greater than 0.96) for each set of experiments.

The slope of the best fit can be used to determine the true uptake coefficient as follows:

$$\gamma_{0,t} = \text{slope (mg}^{-1}\text{)} \frac{A_s \text{ (cm}^2\text{)}}{S_{\text{BET}} \text{ (cm}^2 \text{mg}^{-1}\text{)}}. \quad (33)$$

Using equation (33) and the measured S_{BET} values from table 1 with the best-fit slopes, $\gamma_{0,t}$ values for the oxides and authentic dust samples were calculated. These values are presented in table 3. It can be seen that the largest observable initial uptake coefficient is for CaO with a value of 2.2×10^{-5} while the smallest observable value is 2.0×10^{-8} for $\gamma\text{-Al}_2\text{O}_3$. The initial uptake coefficient for most of the other oxides falls in the 10^{-6} range as they do for the authentic Gobi and Saharan samples.

Table 3. The experimentally determined true initial uptake coefficients for the reaction of NO_2 with the oxide particles and authentic dust samples used in these experiments.

Sample	Slope (mg^{-1})	Correlation coefficient	$\gamma_{0,t}$ ^a
$\alpha\text{-Al}_2\text{O}_3$	1.1×10^{-4}	0.995	9.1×10^{-6b}
$\gamma\text{-Al}_2\text{O}_3$	1.7×10^{-6}	0.997	2.0×10^{-8b}
$\alpha\text{-Fe}_2\text{O}_3$	3.5×10^{-5}	0.974	7.7×10^{-6c}
$\gamma\text{-Fe}_2\text{O}_3$	1.7×10^{-4}	0.969	4.0×10^{-6b}
TiO_2	5.6×10^{-6}	0.999	1.3×10^{-7b}
SiO_2	—	—	—
MgO	3.5×10^{-4}	0.996	1.2×10^{-5c}
CaO	1.7×10^{-4}	0.998	2.2×10^{-5c}
Gobi dust	4.5×10^{-5}	0.994	2.1×10^{-6c}
Saharan sand	7.2×10^{-6}	0.994	1.2×10^{-6c}

^a Calculated using equation (33) (see text).

^b Sample holder area, 11.88 cm^2 .

^c Sample holder area, 5.07 cm^2 .

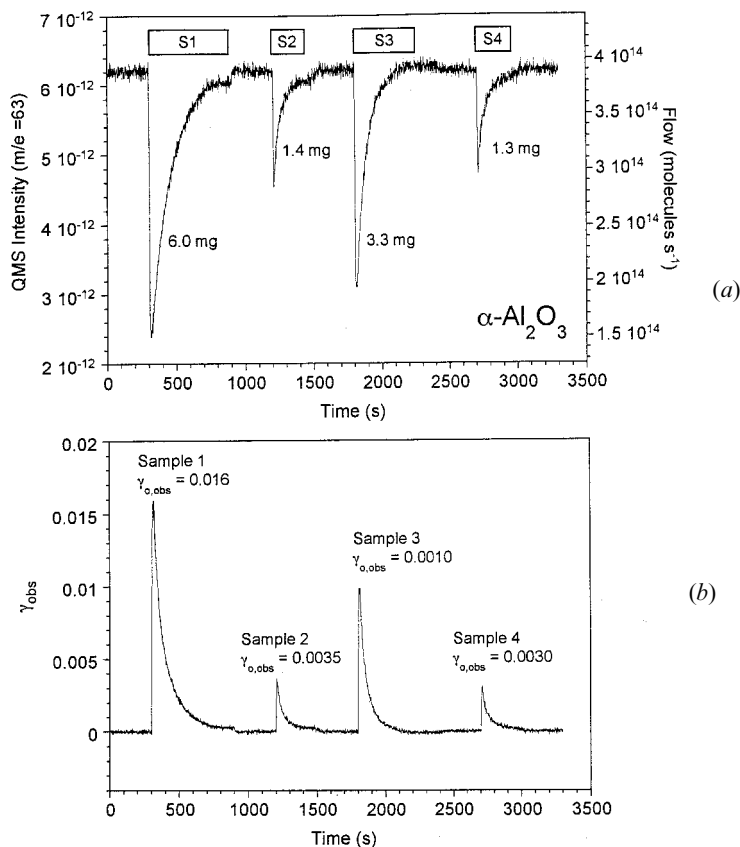
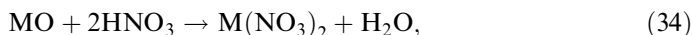


Figure 15. (a) Typical Knudsen cell data for the uptake of HNO_3 on four different samples S1–S4 of $\alpha\text{-Al}_2\text{O}_3$ represented in both QMS intensity ($m/e = 63$) (left axis) and flow (right axis). The rectangular boxes denote the times during which the sample compartments were opened. (b) The uptake coefficients calculated for the data shown in (a) using equation (8) with an escape aperture with $A_h = 0.0484 \text{ cm}^2$ and $A_s = 5.07 \text{ cm}^2$. The initial pressure in the Knudsen cell is $40 \mu\text{Torr}$ (1.3×10^{12} molecules/ cm^3).

The heterogeneous reaction kinetics for the uptake of HNO_3 on oxides and authentic dust samples was also measured. As discussed above, reaction of HNO_3 on most of the oxides appears to be simple adsorption with no detectable gas-phase products. However, reaction with both MgO and CaO appears to produce H_2O . One possible explanation for this is the neutralization reaction



where M is either Mg^{2+} or Ca^{2+} .

As with NO_2 , the observed initial uptake coefficients for HNO_3 were measured as a function of sample mass and the true initial uptake coefficients were then determined. Representative Knudsen cell data using the multisample-holder cell are shown in figure 15; both the raw data and the observed uptake as functions of time are plotted. As with NO_2 , the observed initial uptake coefficient for HNO_3 on $\alpha\text{-Al}_2\text{O}_3$ is clearly dependent on mass.

Table 4. The experimentally determined true initial uptake coefficients for the reaction of HNO_3 with the oxide particles and authentic dust samples used in these experiments.

Sample	Slope (mg^{-1})	Correlation coefficient	$\gamma_{0,t}^{a,b}$
$\alpha\text{-Al}_2\text{O}_3$	5.8×10^{-3}	0.995	9.7×10^{-5}
SiO_2^c	2.9×10^{-4}	0.999	2.9×10^{-5}
$\alpha\text{-Fe}_2\text{O}_3$	2.4×10^{-4}	0.999	5.3×10^{-5}
MgO	1.1×10^{-2}	0.994	4.0×10^{-4}
CaO	4.7×10^{-2}	0.999	6.1×10^{-3}
Gobi dust	1.3×10^{-3}	0.999	5.2×10^{-5}
Saharan sand	1.2×10^{-4}	0.980	2.0×10^{-5}

^a Calculated using equation (33) (see text).

^b All data collected with a sample holder area of 5.07 cm^2 .

^c Larger SiO_2 particles were used in these experiments with a surface area of $500 \text{ cm}^2 \text{ mg}^{-1}$.

Plots of $\gamma_{0,\text{obs}}$ determined via equation (8), as functions of sample mass were determined for several oxides and authentic dust samples. For thin sample masses, $\gamma_{0,\text{obs}}$ versus mass was found to be linear. The slopes of these plots and values of $\gamma_{0,\text{obs}}$ determined using equation (33) are presented in table 4 where it can be seen that the HNO_3 values are one to two orders of magnitude greater than the corresponding values of the uptake coefficient determined for NO_2 . Adsorbed H_2O has also been shown to play an important role in HNO_3 uptake on salt particles (Beichert and Finlayson-Pitts 1996, Davies and Cox 1998). There also appears to be a strong dependence on the amount of H_2O present on the surface of the samples in these experiments as the uptake of HNO_3 is enhanced in the presence of adsorbed H_2O . Experiments to determine uptake coefficients as a function of RH are discussed in section 4.

Although the uptake coefficients presented in tables 3 and 4 represent true uptake coefficients, that is the fraction of molecules that will adsorb or react on a per collision basis, they are not necessarily the values that should be incorporated into atmospheric models. The reason for this is that it is assumed within the models that each time that a reactant molecule approaches an aerosol particle it collides only once. Because the authentic mineral aerosols are not smooth spherical particles but rather rough crystalline granules, it is likely that a single approach will lead to multiple collisions. An estimate for the number of collisions can be made by considering R_G , the ratio of the microscopic surface area of the particle, defined as the BET surface area, to the surface area of a smooth particle of the same diameter (King and Tomkins 1967). The effect of these multiple collisions can then be incorporated into the model calculations by using an effective uptake coefficient determined by simply multiplying the true uptake coefficient by the average number R_G of collisions per approach. These values are presented for reaction with both NO_2 and HNO_3 in table 5.

3.4. Model analysis of the heterogeneous uptake of NO_2 and HNO_3 on mineral dust aerosol

In order to assess the importance of the heterogeneous reaction of NO_2 and HNO_3 on mineral oxides and dust, a box-model analysis was performed for various

Table 5. The experimentally determined uptake coefficients for NO_2 and HNO_3 adjusted for multiple collisions caused by the roughness of the individual particles, that is $\gamma^* = \gamma_{0,t} R_G$.

Material	R_G	$\gamma_{\text{NO}_2}^*$	$\gamma_{\text{HNO}_3}^*$
$\gamma\text{-Fe}_2\text{O}_3$	1.0	4×10^{-6}	—
TiO_2	1.0	9×10^{-6}	—
$\gamma\text{-Al}_2\text{O}_3$	1.1	2.2×10^{-8}	—
$\alpha\text{-Fe}_2\text{O}_3$	1.3	1.1×10^{-5}	6.9×10^{-5}
MgO	1.8	1.8×10^{-5}	7.2×10^{-4}
CaO	2.7	5.4×10^{-5}	1.6×10^{-2}
$\alpha\text{-Al}_2\text{O}_3$	9.4	8.5×10^{-5}	9.1×10^{-4}
Saharan sand	^a	$1 \times 10^{-6} R_G$	$2 \times 10^{-5} R_G$
Gobi dust	22	4.4×10^{-5}	1.1×10^{-3}

^a Unable to calculate owing to a large size distribution.

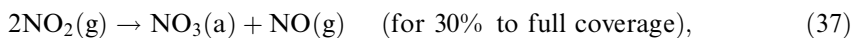
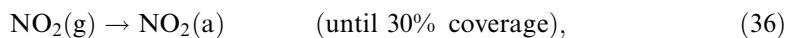
chemical regimes. Conditions representative of Cheju, South Korea, were considered. Cheju is an island located in the East China Sea, which is impacted by anthropogenic pollution and mineral aerosol during the frequent continental outflow events in the spring. A series of simulations were conducted to explore a range of chemical and physical conditions, as summarized in table 6. The values used for emission rates and dry deposition rates were taken from Sander and Crutzen (1996).

The heterogeneous uptake rate constant for the specified size distribution were calculated using a log-normal distribution for the aerosol number–size distribution (Jaenicke and Hanusch 1993, Zhang *et al.* 1994). The log-normal number–size distribution is expressed in the following manner:

$$\frac{dN(r)}{d(\log r)} = \sum_{i=1}^3 \frac{n_i}{\log \sigma_i (2\pi)^{1/2}} \exp\left(\frac{-[(\log r)/R_i]^2}{2(\log \sigma_i)^2}\right), \quad (35)$$

where r (μm) is the particle radius, $N(r)$ (cm^{-3}) is the cumulative particle number distribution for particles larger than r , R (μm) is the mean particle radius, n is the integral of the normal function and $\log \sigma$ is a measure of particle polydispersity. The parameters for the Cheju simulation were taken from Zhang *et al.* (1994): $n = 7.98$, $r = 0.88 \mu\text{m}$ and $\sigma = 0.23$. For these parameters the geometric surface area is $0.85 \text{ m}^2 \text{ g}^{-1}$. Although the laboratory data show that there are some differences in the uptake coefficients determined for different oxides and dust samples, the current model does not take into account chemical heterogeneity of the mineral dust particles.

To mimic the experimental findings the following reaction sequence was assumed:



The effects of the heterogeneous reactions of NO_2 for the base conditions (300 K) are shown in figure 16. Also shown are results where the heterogeneous reaction was ignored (i.e. gas-phase reactions only). Plotted are O_3 , NO_x and HNO_3 mixing ratios over a 120 h period. Under these conditions, O_3 quickly increases. However, the NO_x

Table 6. Summary of the initial physical and chemical simulation conditions used.

Initial conditions	
Species	Concentration (ppb)
NO	1.5
NO ₂	0.5
HNO ₃	0.0005
NH ₃	1.0
SO ₂	8.0
H ₂ SO ₄	0.8
O ₃	50.0
C ₂ H ₆	2.853
C ₃ H ₈	1.379
ALKANE ^a	1.233
C ₂ H ₄	3.461
ALKENE ^b	0.692
Aromatic	6.290
C ₂ H ₂	0.895
H ₂ O ₂	2.0
Isoprene	5.0
Dimethylsulphide	0.005
H ₂ S	0.001
CO	150.0

Meteorological and other factors	
	Value
Temperature	300 K
RH	80%
With and without surface emissions of NO	5×10^4 molecules cm ⁻² s ⁻¹
Dry deposition included	
γ_{NO_2} ^c	{ 10^{-5} , 10^{-4} , 10^{-3} , 10^{-2} }
γ_{HNO_3} ^c	{ 10^{-4} , 10^{-3} , 10^{-2} , 10^{-1} }
With and without reactions leading to the recycling of NO(g)	
Mass loading	160–400 $\mu\text{g m}^{-3}$

^a ALKANE denotes a higher alkane than propane.

^b ALKENE denotes a higher alkene than ethene.

^c Values adjusted for roughness effects (see table 5).

in the system is rapidly converted (about 2 h) to other forms (PAN, HNO₃, etc.), the O₃ production rate decreases quickly, and the system switches to a net O₃ destructive environment after about 15 h. After this time, O₃ decreases owing to chemical destruction and dry deposition. The effect of the NO₂ heterogeneous reaction is to accelerate the NO_x loss rates and to reduce the net O₃ production and the HNO₃ concentrations. Under these simulated conditions, γ_{NO_2} must be 10^{-4} (i.e. adjusted values $R_G \gamma_{0,t}$) to have an effect on the chemistry. The maximum calculated effect on O₃ is about 10% at $\gamma_{\text{NO}_2} = 10^{-2}$, as shown in table 7.

The number of molecules adsorbed was calculated and is also shown in figure 16. For $\gamma_{\text{NO}_2} < 10^{-4}$ the surface coverage of the adsorbed NO₂ remains well below

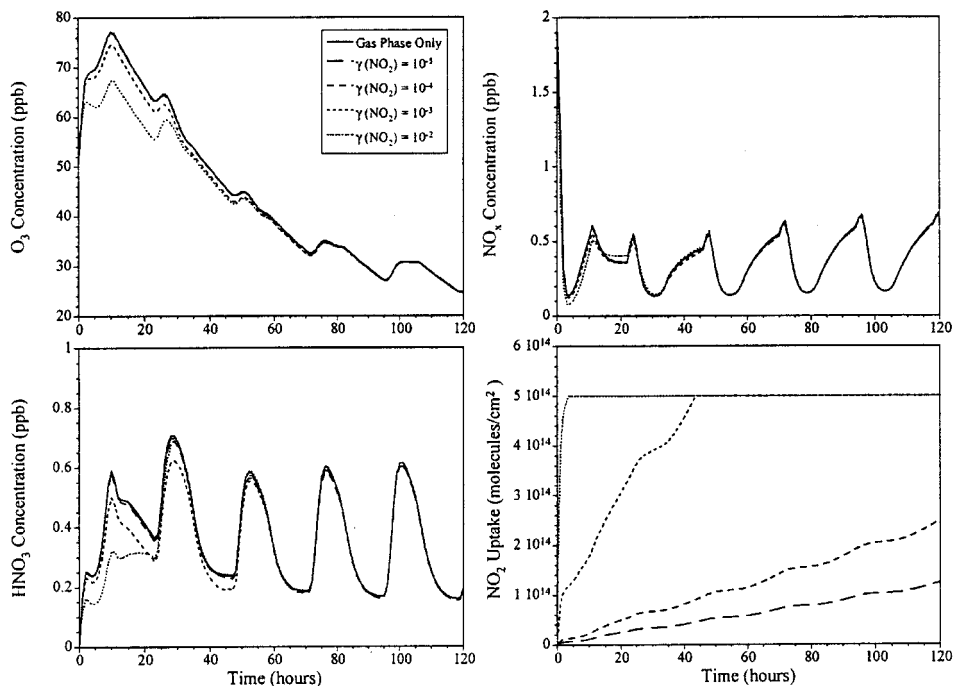


Figure 16. The effects of the heterogeneous reactions of NO_2 for the case with emission sources of NO into the box at 300 K. Complete simulation details are presented in table 6. Shown are O_3 , HNO_3 and NO_x concentrations over a 120 h period. Surface coverage as a function of time is also presented.

Table 7. The effect of increasing the uptake coefficient γ on atmospheric mixing ratios. The values are calculated relative to the no-surface-reaction case.

γ_{NO_2}	$\Delta[\text{O}_3]_{\text{max}}$ (%)	$\Delta[\text{NO}_x]_{\text{max}}$ (%)	$\Delta[\text{HNO}_3]_{\text{max}}$ (%)
10^{-5}	-0.13	-0.19	-0.83
10^{-4}	-0.39	-0.39	-1.86
10^{-3}	-3.37	-7.50	-15.3
10^{-2}	-12.8	-18.1	-45.6

monolayer coverage (taken as 5×10^{14} molecules cm^{-2}); thus no saturation effects are expected. For larger values of γ_{NO_2} , saturation effects are important. For example, for $\gamma_{\text{NO}_2} = 10^{-3}$, the surface is saturated after about 40 h. Although the uptake coefficient is time dependent, or more accurately coverage dependent, we have assumed a single-valued γ throughout the simulation until surface saturation. At the saturation coverage of 5×10^{14} molecules cm^{-2} , γ was then set equal to zero.

For $\gamma_{\text{NO}_2} > 10^{-4}$, significant effects on modelled O_3 and HNO_3 are found (see table 7). However, owing to surface saturation, the effects are limited to the first 40 h. As such, we also investigated the case where the surface maintains its reactivity without saturating (this could be as a result of site reactivation due to photodesorption or reaction with another species or due to continuous uptake by a layer of H_2O for example). In this case, the process was modelled by reactions (36) and (37), with

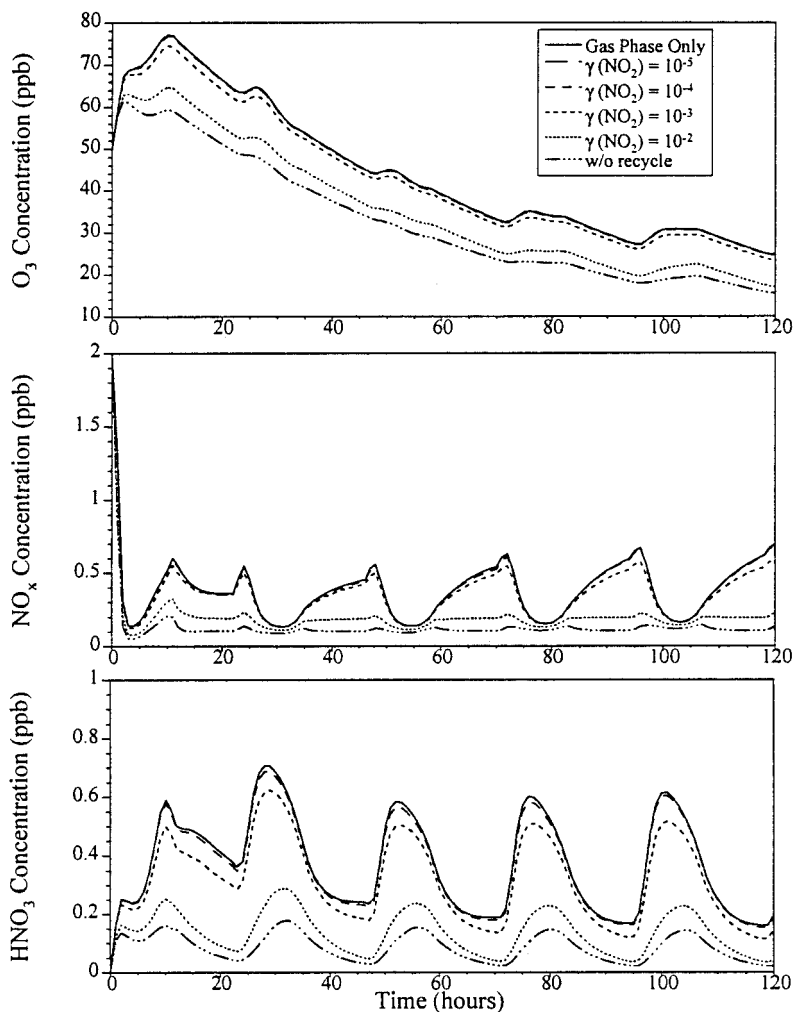


Figure 17. O_3 , HNO_3 and NO_x concentrations over a 120 h period under the same conditions as those in figure 16, but for the case where the surface reaction of NO_2 proceeds without saturation (i.e. reaction sequence (36) and (37) only). Also shown are results for the case of no recycle reaction producing $NO(g)$.

reaction (37) lasting throughout the simulation. These results, presented in figure 17, represent the upper limit to the influence of NO_2 surface uptake. $\gamma_{NO_2} > 10^{-4}$ is shown to have a large influence on both HNO_3 and O_3 concentrations.

Also shown in figure 17 is the effect of the recycle channel in which the NO_2 surface reaction produces $NO(g)$ (i.e. reaction (37)). The additional case when reaction (38) was disabled is also plotted. As shown, O_3 , NO_x and HNO_3 concentrations are greatly reduced.

The impact of aerosol mass loading in determining the importance of the heterogeneous reaction of NO_2 was also studied. The results are summarized in table 8 where it can be seen that the magnitude of the effect of the surface reaction on O_3 , NO_x and HNO_3 concentrations increases approximately linearly with increasing mass loading. The effect of mean mineral aerosol radius was also investigated by

Table 8. The effect of the aerosol distribution (dust mass loading) on atmospheric mixing ratios. The units are calculated relative to the no-surface-reaction case. Results are for $\gamma_{\text{NO}_2} = 10^{-3}$; all other conditions are the same as those used in figure 21.

n	m ($\mu\text{g m}^{-3}$)	$\Delta[\text{O}_3]_{\text{max}}$ (%)	$\Delta[\text{NO}_x]_{\text{max}}$ (%)	$\Delta[\text{HNO}_3]_{\text{max}}$ (%)
7.98	160	-3.37	-7.50	-15.3
10.0	201	-4.27	-9.42	-18.8
15.0	302	-6.22	-14.2	-26.9
20.0	403	-7.51	-16.9	-31.2

Table 9. The effect of the aerosol distribution (peak radius) on atmospheric mixing ratios (m (dust mass loading) = $160 \mu\text{g m}^{-3}$; $\log \sigma = 0.23$). The units are calculated relative to the no-surface-reaction case. Results are for $\gamma_{\text{NO}_2} = 10^{-3}$; all other conditions are the same as those used in figure 21.

n	R (μm)	$\Delta[\text{O}_3]_{\text{max}}$ (%)	$\Delta[\text{NO}_x]_{\text{max}}$ (%)	$\Delta[\text{HNO}_3]_{\text{max}}$ (%)
5.43	1.0	-2.72	-7.47	-12.9
7.98	0.88	-3.37	-7.50	-15.3
15.8	0.70	-3.63	-8.24	-16.3
43.5	0.50	-4.66	-10.9	-20.3

simulations at a fixed mass loading and varying R in equation (35). As the particle size distribution shifts to smaller mean radii, the impact of the surface reaction with NO_2 increases (table 9).

The impact of the heterogeneous reaction of HNO_3 on mineral surfaces was also simulated and the results are shown in figure 18. Values of $\gamma_{\text{HNO}_3} > 10^{-4}$ are shown to represent a major loss mechanism of HNO_3 . The heterogeneous loss of HNO_3 results in a large decrease in predicted HNO_3 (and HNO_3 -to- NO_x ratios); however, the effect of a pure heterogeneous loss of HNO_3 on O_3 and NO_x levels is small. The effects of the direct surface reaction of HNO_3 at $\gamma_{\text{HNO}_3} = 10^{-3}$ on the HNO_3 concentration are approximately twice the effects of the NO_2 reaction on HNO_3 with $\gamma_{\text{NO}_2} = 10^{-3}$. This difference is related to the fact that the initial HNO_3 concentrations are much lower than NO_x concentrations and thus are more affected by available dust surface area.

Box-model simulations showed that γ_{NO_2} and γ_{HNO_3} must be greater than 10^{-4} for these process to be important under the conditions studied. The laboratory results presented in this paper suggest that the NO_2 reaction is at the lower end of importance, while the HNO_3 reaction is clearly significant. This is illustrated in a model run using $\gamma_{\text{NO}_2} = 10^{-5}$ and $\gamma_{\text{HNO}_3} = 10^{-3}$ and reaction sequence (36)–(38) (figure 19). No effect is found in the calculated mixing ratios of O_3 or NO_x while that of HNO_3 is reduced by 30%. The conclusions based on the models are for NO_x -limited regimes as most regions are NO_x limited. For a NO_x -saturated regime, the loss of NO_x to dust is expected to lead to an increase in O_3 levels.

The results presented here for NO_x -limited regimes should be viewed as lower-limit estimates for a variety of reasons. One important consideration is that these experimental results represent very dry conditions. As discussed in section 4, γ_{HNO_3} is

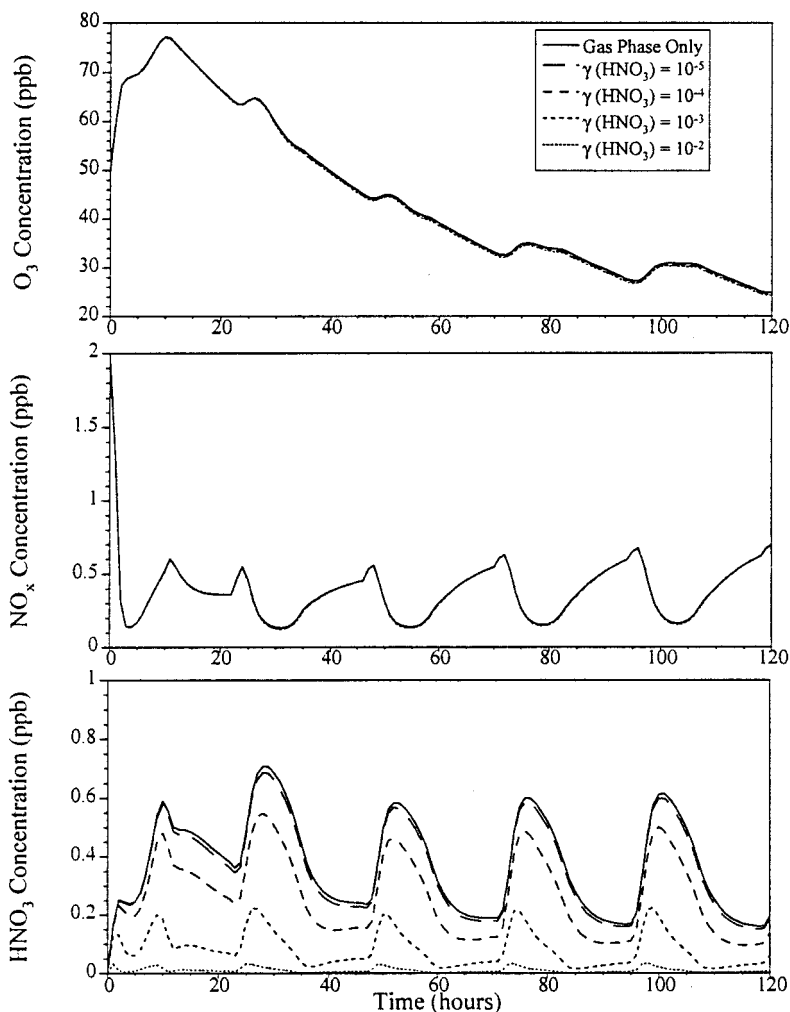


Figure 18. The effect of heterogeneous uptake of HNO_3 on O_3 , NO_x and HNO_3 concentrations. The conditions are the same as those in figure 16, but with $\gamma_{\text{NO}_2} = 0$.

greatly enhanced by surface-adsorbed H_2O . Under conditions that more closely simulate the atmosphere, that is 20–90% RH it is shown next that γ_{HNO_3} is significantly increased. The effect of adsorbed H_2O on the NO_2 surface reaction rate is less clear at this time; however, the observation that H_2O reacts directly with NO_2 on SiO_2 surfaces to yield nitrous acid (HONO) (see section 5 and Goodman *et al.* (1999)) suggests that it will also affect γ_{NO_2} values on other oxide surfaces. Another consideration is the effects of mass loading and size distribution. As shown, increasing the mass loading or reducing the mean radius increases the importance of these reactions. We are currently investigating all these effects as well as the effect of particle ageing (i.e. the adsorption of an external sulphate or nitrate layer). The further quantification of the uptake of NO_2 is important, as each molecule of NO_2 that is converted to nitrate via heterogeneous surface reaction represents a net reduction in O_3 production rates. Thus such reactions may play a key role in determining the net effect of anthropogenic NO_x emissions on tropospheric O_3

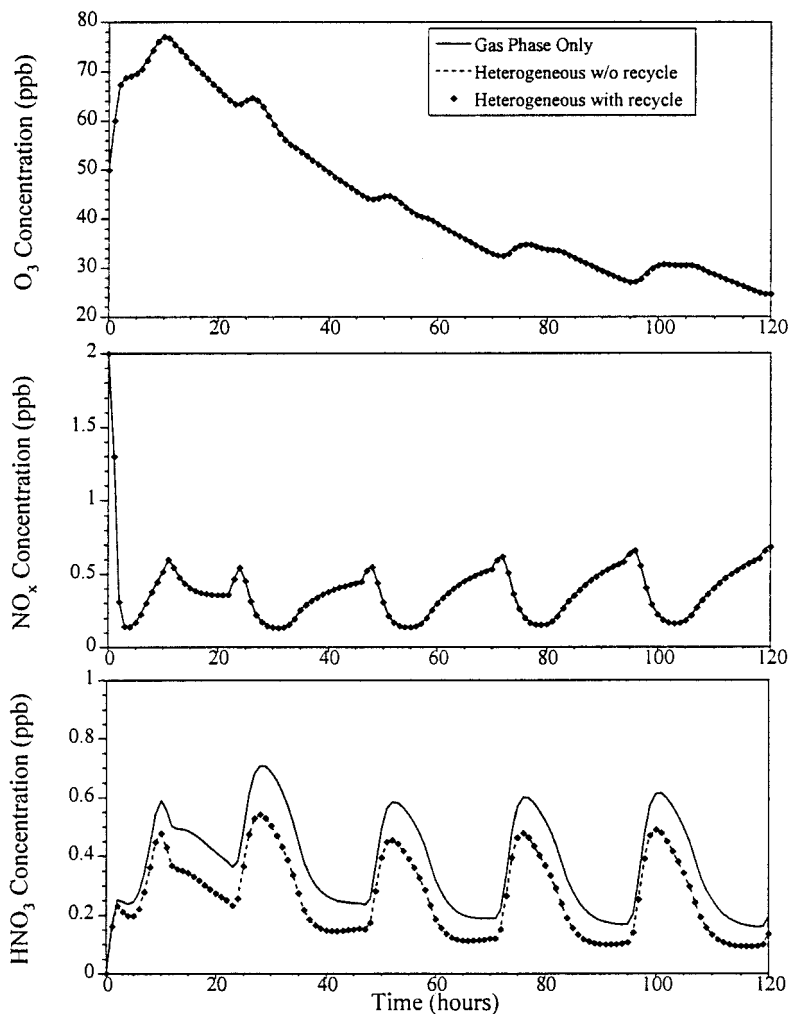


Figure 19. Simulations using the best estimates of γ_{NO_2} and γ_{HNO_3} from our granular adjusted laboratory uptake measurements (i.e. $\gamma_{\text{NO}_2}^* = 10^{-3}$ and $\gamma_{\text{HNO}_3}^* = 10^{-3}$). All other conditions are the same as those in figure 20.

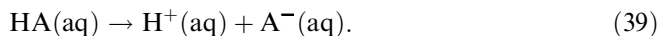
levels, as recently discussed by Parrish *et al.* (1999). In addition, at high relative humidities, the nitrate coating formed on mineral dust from heterogeneous reaction of NO_2 and HNO_3 participates in the hygroscopic deliquescence and efflorescence cycles. These cycles are influenced by the presence of mineral dust (Han and Martin 1999, Martin 2000).

4. Role of H_2O vapour and surface-adsorbed H_2O in the heterogeneous uptake of HNO_3 on oxide, carbonate and authentic dust particles

4.1. The importance of adsorbed water in heterogeneous reactions

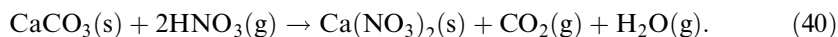
The role of adsorbed H_2O in the uptake of gases on solid aerosol surfaces is a focus of many studies. H_2O can play a dual role acting as a reactant, as in the case of the hydrolysis of N_2O_5 to give HNO_3 , and as a medium for the ionic dissociation of

gases, that is inorganic and organic acids can undergo dissociation in aqueous media as follows:



The ionic dissociation reaction will be greatly facilitated by adsorbed H_2O and a 'liquid' H_2O layer on the aerosol surface. The hypothesis of a H_2O layer or a quasiliquid layer is analogous to that discussed by Abbatt *et al.* (1992) and discussed by Molina (1994) for hydrochloric acid (HCl) on ice surfaces in which a 'quasiliquid' HCl solution with essentially the same chemical reactivity as that of a true liquid HCl solution is formed. Vogt and Finlayson-Pitts (1994) also proposed a similar picture involving a H_2O layer for the reaction of HNO_3 on NaCl particle surfaces. When H_2O is present, the nitrate ions may be in a quasiliquid state in which nitrate ions are mobile. Upon heating, the nitrate ions coalesce to form separate regions of sodium nitrate (NaNO_3) on the NaCl surface. Davies and Cox (1998) also investigated the heterogeneous reactions of HNO_3 with NaCl in the presence of H_2O vapour. They proposed a two-step process whereby adsorption of HNO_3 molecules on the surface is followed by diffusion to the defect sites where H_2O molecules were adsorbed. They also proposed that bulk reactivity of the NaCl particle was possible as these defect sites were regenerated.

In our laboratory, we have investigated the role that H_2O plays in the adsorption of HNO_3 on oxides, mineral dust and calcium carbonate (CaCO_3). Our interest in CaCO_3 comes from the suggestion that mineral aerosols containing CaCO_3 may be especially effective in removing gas-phase HNO_3 from the atmosphere as shown in the following reaction (Dentener *et al.* 1996, Tabazadeh *et al.* 1998):



This heterogeneous pathway may provide a significant chemical sink for HNO_3 especially if the reaction is not limited to the surface of the CaCO_3 particle but can react into the bulk of the particle. Song and Carmichael (2001) modelled reaction (40) with aerosols containing CaCO_3 and found the HNO_3 -to- NO_x ratio to decrease by a factor of two to six when compared with models containing only gas-phase processes. Even using the recently measured rate for the oxidation of NO_2 by hydroxyl radicals (Donahue *et al.* 1997) which is 20–30% lower than previously reported, it is found that heterogeneous loss of HNO_3 is still significant in the modelling results (Song 1999, Song and Carmichael 2001). Tabazadeh *et al.* (1998) have also suggested that heterogeneous reactions on biomass aerosols, as well as mineral dust containing CaCO_3 , can irreversibly remove HNO_3 from the gas phase and provide an important sink for HNO_3 . As discussed in detail below, surface-adsorbed H_2O which is a function of the RH, greatly increases the extent and rate of reaction of HNO_3 on oxide, carbonate and mineral dust.

4.2. *In-situ spectroscopic measurements of the heterogeneous reaction of HNO_3 on CaCO_3 particles in the presence of H_2O*

The reaction of gaseous HNO_3 on CaCO_3 particles with varying amounts of H_2O has been investigated using FTIR spectroscopy at 295 K. Upon exposure of HNO_3 to dry CaCO_3 particles, very few changes in the gas-phase spectrum and the solid-particle spectrum are observed. When CaCO_3 is exposed to HNO_3 in the presence of H_2O vapour corresponding to 20% RH, there are several interesting changes in both the IR spectrum of the gas phase and of the CaCO_3 particles. First, in the spectral

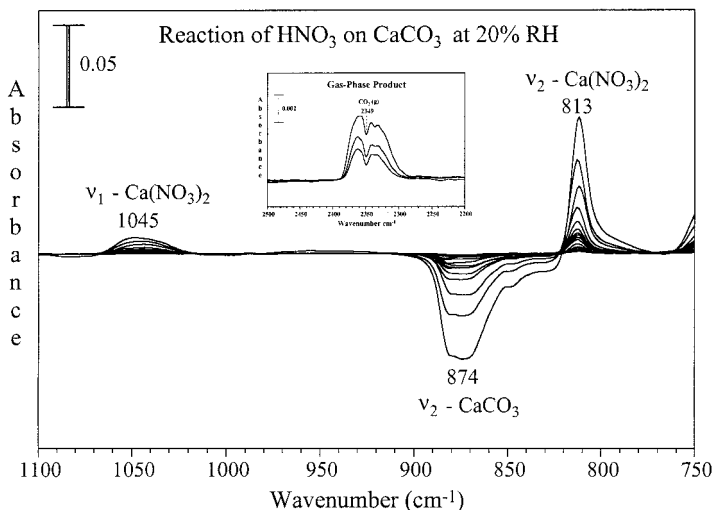


Figure 20. Transmission FTIR difference spectra of adsorbed products on CaCO₃ in the spectral range between 1100 and 750 cm⁻¹. FTIR spectra of CaCO₃ were recorded as a function of HNO₃ exposure (millitorr pressure range) in the presence of gas-phase H₂O (20% RH). The negative features are due to the loss of CaCO₃ and the positive features are due to the growth of Ca(NO₃)₂. The inset shows the growth of the absorption band due to the production of gas-phase CO₂ as the reaction proceeds.

range extending between 1100 and 750 cm⁻¹, absorption bands at 813 and 1045 cm⁻¹ due to adsorbed calcium nitrate (Ca(NO₃)₂) continuously grow in intensity as CaCO₃ is exposed to HNO₃ in the presence of H₂O vapour (figure 20) and there is no evidence of surface saturation. Second, CO₂ absorptions appear in the gas phase spectrum as shown in the inset of figure 20. Third, as CaCO₃ reacts with HNO₃ to form Ca(NO₃)₂ a broad band between 3000 and 3750 cm⁻¹ continuously grows in intensity (figure 21). This broad band is composed of three peaks at 3280, 3530 and 3605 cm⁻¹ which are assigned to the OH stretching vibrations of H₂O adsorbed on the particle surface. As discussed below, this increase in H₂O adsorption at a constant H₂O vapour pressure can be explained by the increase in the amount of Ca(NO₃)₂ on the particle surface. Ca(NO₃)₂ is approximately 105 times more soluble than CaCO₃ (Lide 1991). Therefore, as HNO₃ is reacted with CaCO₃ in the presence of H₂O, CaCO₃ is converted to Ca(NO₃)₂, allowing more H₂O to adsorb on to the surface.

The spectrum of H₂O adsorbed on CaCO₃ particles reacted with HNO₃ is distinctly different from the spectrum of adsorbed H₂O on CaCO₃ particles not exposed to HNO₃. For example, in the early stages of the reaction when CaCO₃ particles are exposed to HNO₃ in the presence of H₂O vapour, the surface H₂O band is first detected as a single asymmetric broad band centred at 3500 cm⁻¹. As the reaction progresses, three distinct peaks at 3605, 3530 and 3280 cm⁻¹ within the broad band between 3750 and 3000 cm⁻¹ become apparent.

Peters and Ewing (1997) have investigated H₂O adsorption on NaCl(100) under ambient conditions. In their studies, they found that at coverages less than two monolayers, H₂O adsorbed on NaCl(100) surfaces behaves similar to that of condensed H₂O. However, as coverage increases above two monolayers, they found that Na⁺ and Cl⁻ ions are incorporated into the H₂O layer, although the H₂O layer

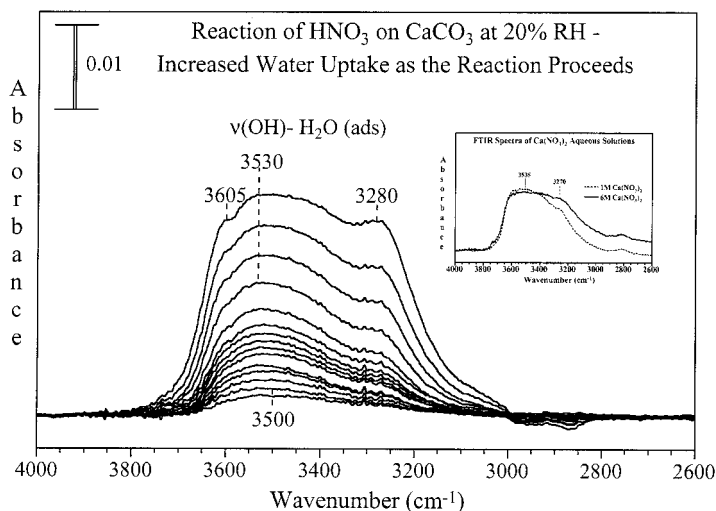


Figure 21. Transmission FTIR difference spectra of adsorbed products on CaCO₃ in the spectral range between 4000 and 2600 cm⁻¹. FTIR spectra of CaCO₃ were recorded as a function of HNO₃ exposure (millitorr pressure range) in the presence of gas-phase H₂O (20% RH). The IR data show that, as the reaction proceeds, there is growth in the IR absorption band due to adsorbed H₂O on the particle surface. The inset shows the transmission FTIR spectra of concentrated solutions of Ca(NO₃)₂ in H₂O at concentrations of 1 and 6 M. There is similarity between the aqueous solution phase spectra and the spectra of adsorbed H₂O on the HNO₃-reacted CaCO₃ particles.

does not yet have properties of a bulk salt solution. At coverages greater than three monolayers, the H₂O film has properties of a bulk brine solution. This observation is consistent with the work of Barraclough and Hall (1974), who showed that, after adsorption of the first two H₂O layers on NaCl, the H₂O–NaCl isotherms behaved as if a saturated solution of NaCl were present. The H₂O adsorption spectra shown here on HNO₃-reacted CaCO₃ can be interpreted in a similar manner. FTIR spectra of 1 and 6 M Ca(NO₃)₂ solutions in the spectral range extending from 2600 to 4000 cm⁻¹ are shown in figure 21. In these spectra there is a broad absorption band between 3000 and 3800 cm⁻¹ with two bands at 3270 and 3535 cm⁻¹ on top of the broad spectrum. Although there is some shift in the frequency of the bands, the spectra of the Ca(NO₃)₂ solutions look very similar to the spectra obtained by exposing H₂O to CaCO₃ particles that were reacted with HNO₃. The solution phase data support the fact that Ca²⁺ and NO₃⁻ ions are being incorporated into the H₂O film on the CaCO₃ particles and are perturbing the hydrogen-bonding network of the H₂O film.

4.3. Transmission electron microscopy measurements of the carbonate particles

TEM measurements of the CaCO₃ particles after reaction of HNO₃ and CaCO₃ in the presence of H₂O also provided insight about the particle reactivity. A comparison of the electron micrographs of reacted CaCO₃ particles and unreacted CaCO₃ particles are shown in figure 22. The unreacted CaCO₃ particles are mostly spherical in shape and on the length scale shown in the image have well-defined smooth edges. CaCO₃ particles reacted with HNO₃ at a RH of 20% are irregular in

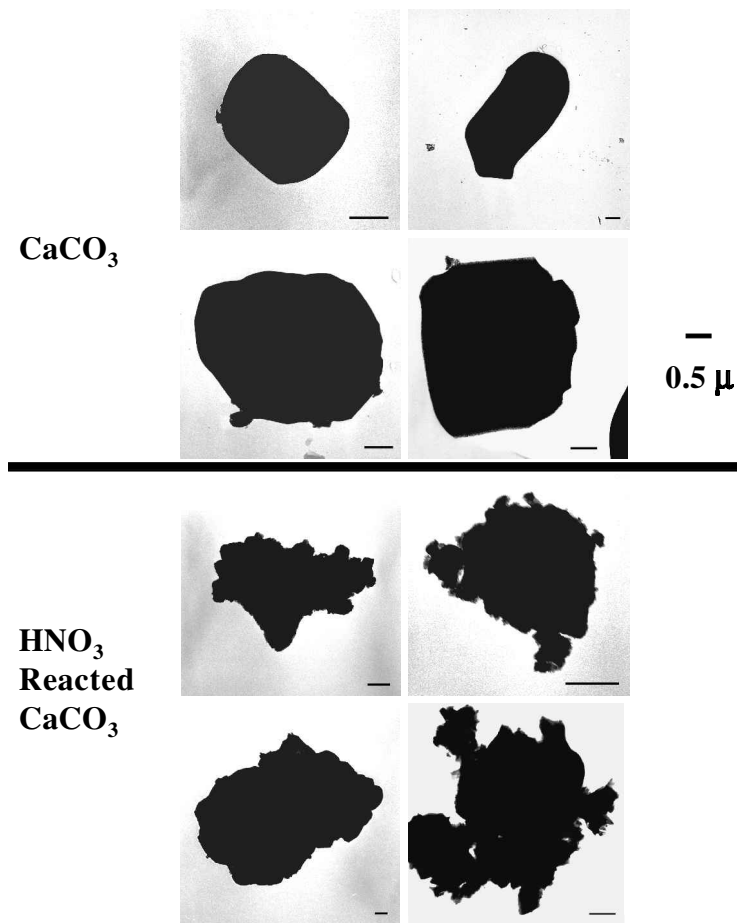


Figure 22. Transmission electron micrographs of CaCO₃ particles that have not been exposed to HNO₃ vapour compared with CaCO₃ particles that have been exposed to HNO₃ vapour in the presence of H₂O vapour. The particles that have not been exposed are nearly spherical and the particle surface appears smooth on the 1 μm length scale (bar, 0.5 μm). In contrast, particles that have been exposed become irregularly shaped with rougher surfaces.

shape and have jagged edges. These images show that the smooth edges of the CaCO₃ particles become highly irregular in shape after reaction with HNO₃ and thus increase the surface area of the CaCO₃ particles. From these changes in surface morphology, one can speculate on a mechanism as to how HNO₃ reacts on the surface and into the bulk of the CaCO₃ particle. When CaCO₃ particles are exposed to HNO₃ in the presence of H₂O vapour, Ca(NO₃)₂ forms. When H₂O vapour is present, a H₂O layer may be available on the particle surface in which nitrate ions are mobile. Upon evacuation of the vapour phase, the nitrate ions are no longer mobile and form islands of Ca(NO₃)₂ on the CaCO₃. The formation of Ca(NO₃)₂ islands would then expose areas of fresh CaCO₃ particles to be available for further reaction when the sample is exposed to a new exposure of HNO₃ and H₂O. Another possibility is that, when CaCO₃ is reacted with HNO₃ in the presence of H₂O, a thin

H₂O layer may form, allowing the HNO₃ to dissolve into solution on the particle surface. The product Ca(NO₃)₂ would form in the liquid layer until the concentration increased enough to reach the saturation point, at which Ca(NO₃)₂ would precipitate from solution and form on the CaCO₃ surface. Further microscopy studies are needed to differentiate these mechanisms.

Several important findings come from the TEM and IR measurements together with gravimetric analysis that has been described by Goodman *et al.* (2000). First, these experiments show that the HNO₃ reaction on CaCO₃ is not limited to the surface but can react with the bulk of the particles. This is important as the reactivity is not limited to one layer and a surface coverage of about 5×10^{14} molecules cm⁻². Second, the uptake of HNO₃ on CaCO₃ is found to be irreversible. Third, the ability of the particle to adsorb H₂O is greatly enhanced and suggests that a significant H₂O layer will be involved in the subsequent reactivity of the particle.

4.4. *In-situ spectroscopic measurements of the heterogeneous reaction of HNO₃ on oxide particles in the presence of H₂O*

Similar to the irreversible uptake of HNO₃ on CaCO₃ particles, HNO₃ also irreversibly adsorbs at 295 K on nearly all the oxides investigated, Al₂O₃, Fe₂O₃, TiO₂, CaO and MgO, with the exception of SiO₂ (Goodman 2000, Goodman *et al.* 2001). Surface-limited reactions are observed for Al₂O₃, Fe₂O₃ and TiO₂ whereas, for the basic oxides CaO and MgO, surface and bulk reactivity, similar to that found for CaCO₃, are found to occur in the presence of H₂O vapour. The rate of HNO₃ uptake on oxide particles as a function of RH was determined by time course FTIR experiments. Kinetic experiments were done on two different oxides α -Al₂O₃ and CaO.

Representative spectra collected for HNO₃ uptake on α -Al₂O₃ and CaO under dry conditions as functions of time are shown in figure 23. For α -Al₂O₃ and CaO particles, the particles were exposed to 9 mTorr corresponding to 2.9×10^{14} molecules cm⁻³ and spectra were recorded every 7 s (four scans per spectrum) at an instrument resolution of 4 cm⁻¹. The extent of HNO₃ uptake on α -Al₂O₃ was determined by integrating the entire region extending from 1189 to 1822 cm⁻¹. A plot of the integrated absorbance as a function of time is shown in the inset of the spectrum in figure 23 (a). The region extending from 1189 to 1822 cm⁻¹ corresponds to absorption of predominantly oxide-coordinated nitrate as well as a small amount of molecularly adsorbed HNO₃. For CaO, the peak height of the absorption band at 815 cm⁻¹, corresponding to the out-of-plane bend of the ion coordinated nitrate ion, was measured as this was found to be the best method for determining the extent of nitrate adsorption on CaO. The peak height is plotted versus time in the inset shown in the spectrum in figure 23 (b). The main reason for performing these experiments is to determine whether the heterogeneous kinetics are affected by the presence of H₂O vapour and an adsorbed H₂O layer. The rate of HNO₃ uptake on α -Al₂O₃ and CaO particles has been investigated in the presence of differing coverage of adsorbed H₂O. The water coverage was varied by doing experiments at different RHs. The same experimental procedure described above was followed except that the oxide particles in the IR cell were exposed to mixtures of HNO₃ and H₂O vapour. The uptake of HNO₃ on α -Al₂O₃ and CaO particles in the presence of H₂O vapour was complete somewhere between 3 and 30 s after the experiment began, which is many times faster than the uptake of HNO₃ on particles under dry conditions. Therefore, spectra were collected at the maximum data acquisition rate of 1.67 s scans per

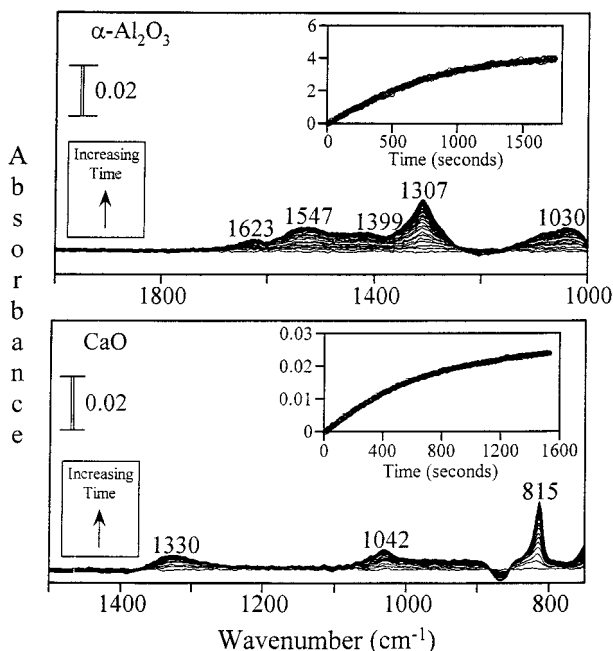


Figure 23. Transmission FTIR spectra of HNO_3 uptake on $\alpha\text{-Al}_2\text{O}_3$ and CaO particles as a function of time. For clarity, only every tenth spectrum collected is shown in the main portion of the figure. The integrated absorbance (or peak height) for the absorption bands of adsorbed HNO_3 is plotted as a function of time in the inset. The integrated absorbance of every spectrum collected is used and plotted in the inset.

second (one scan per spectrum) at an instrument resolution of 8 cm^{-1} . At RHs greater than 17%, the reaction of HNO_3 on $\alpha\text{-Al}_2\text{O}_3$ and CaO saturated in less than 3 s, thus limiting our ability to measure reactive uptake coefficients much above 17% RH.

The kinetic data collected under dry and conditions were analysed according to the procedure described in section 2.3.2. The integrated absorbances (or peak heights) were calibrated to surface coverage (molecules per square centimetre) using volumetric methods (Goodman 2000). Together with the calibration, the linear portion of the integrated absorbance versus time curves is used to calculate the adsorption rate dN_a/dt . The flux is calculated from the gas-phase pressure according to equation (25). For the experiments with H_2O vapour present, it was necessary to increase the HNO_3 concentration as some of the gas-phase HNO_3 was lost in the H_2O layer on the reaction vessel walls. The increased uptake on the walls was determined in separate experiments. Therefore, the measured uptake is a lower limit as the gas flux to the surface is overestimated in the analysis of γ .

In order to determine how adsorbed H_2O affects the heterogeneous kinetics, it is necessary to quantify the amount of adsorbed H_2O on the oxide particle surface as a function of RH. The spectra of H_2O adsorbed on the surface of $\alpha\text{-Al}_2\text{O}_3$ particles at H_2O vapour pressures between 0.430 and 20.3 Torr, corresponding to 2–96% RH, are shown in figure 24. The O—H stretching and H_2O bending adsorption bands are centred at about 3390 and at about 1640 cm^{-1} respectively for $\alpha\text{-Al}_2\text{O}_3$. Although the O—H region is the most thoroughly studied spectral region of liquid H_2O , overlapping frequencies of the asymmetric and symmetric O—H stretching modes and

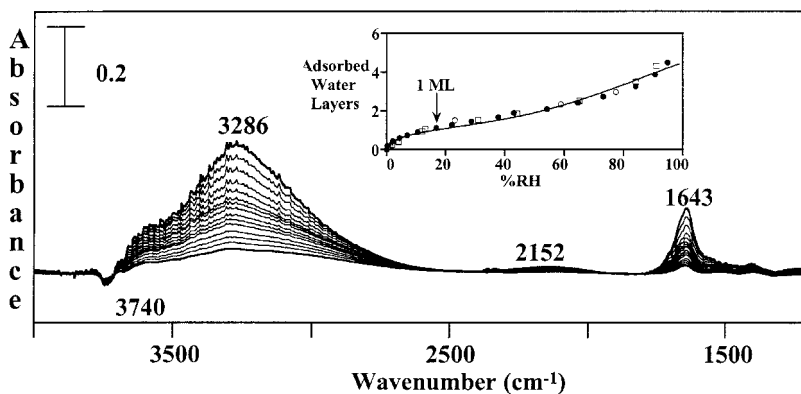


Figure 24. Transmission FTIR spectra of H_2O adsorption on $\alpha\text{-Al}_2\text{O}_3$ at 296 K as a function of pressure between 2 and 96% RH corresponding to H_2O pressures of 0.430 to 20.3 Torr. FTIR spectra of adsorbed water were recorded in the presence of the H_2O vapour. Each spectrum was referenced to the appropriate clean $\alpha\text{-Al}_2\text{O}_3$ spectrum prior to exposure to H_2O vapour. Gas-phase absorptions were then subtracted from each spectrum. The inset shows the amount of adsorbed H_2O quantified in terms of the number of H_2O layers, which is achieved using the integrated absorbance of the bending mode of adsorbed H_2O at 1643 cm^{-1} , as described in the text: (●), experimental data for H_2O uptake on oxide particles not reacted with HNO_3 ; (○), data for $\alpha\text{-Al}_2\text{O}_3$ measured as a function of decreasing H_2O vapour to show that there is no hysteresis in the adsorption and desorption of H_2O on this oxide; (—), BET fit of the experimental data; (□), experimental data for H_2O uptake on nitrate-coated $\alpha\text{-Al}_2\text{O}_3$ particles, that is oxide particles that had been previously reacted with HNO_3 . One monolayer of adsorbed H_2O is indicated by an arrow.

the H_2O bending mode overtone together with the contribution of the hydroxyl groups terminated on the oxide particle surface make this region difficult to analyse when quantifying the coverage of surface-adsorbed H_2O . In comparison, the spectral region of the H_2O bending mode only contains this vibration. Therefore, the integrated absorbance of the H_2O bending absorption band is used to quantify H_2O coverage on oxide particles and should introduce much less uncertainty and complexity compared with the O—H stretching region. The coverage of adsorbed H_2O on $\alpha\text{-Al}_2\text{O}_3$ (as well as other oxide surfaces) can be quantified by generating adsorption isotherm curves, where the H—O—H bending absorption band of surface-adsorbed H_2O was integrated (as discussed in detail below, integrated absorbance was converted to the number of H_2O layers) and plotted against RH P/P_0 (full circles). The number of adsorbed H_2O molecules was assumed to be a linear function of the integrated absorbance of the bending mode. The data, represented by full circles, exhibit the shape of a type II or s-shaped adsorption isotherm curve, which indicates that multilayer adsorption is occurring and the data were modelled using a BET analysis (Flood 1967, Gregg and Sing 1967).

If adsorption takes place on a uniform surface and an infinite number of layers ($n = \infty$) build up on the surface at the saturation vapour pressure of the adsorbing gas, then most type II adsorption isotherms can be fitted to the two-parameter BET equation

$$V = \frac{V_m c P / P_0}{(1 - P / P_0)(1 - P / P_0 + c P / P_0)}, \quad (41)$$

where V is the volume of gas adsorbed at equilibrium pressure P , V_m is volume of gas necessary to cover the surface of the adsorbent with a complete monolayer, P is the equilibrium pressure of the adsorbing gas and P_0 is the saturation vapour pressure of the adsorbing gas at that temperature. The parameter c is the temperature-dependent constant related to the enthalpies of adsorption of the first and higher layers through

$$c = \exp\left(-\frac{\Delta H_1^0 - \Delta H_2^0}{RT}\right), \quad (42)$$

where ΔH_1^0 is the standard enthalpy of adsorption of the first layer, ΔH_2^0 is the standard enthalpy of adsorption on subsequent layers and is taken as the standard enthalpy of condensation, R is the gas constant and T is the temperature.

In most cases, the two-parameter BET equation shown above does not fit most experimental data at the highest pressures when the adsorption isotherm rises indefinitely and an infinite number of layers ($n = \infty$) of adsorbing gas is predicted to build up on the surface whereas a three-parameter BET equation limits the number of layers of gas adsorbing at high values of P/P_0 by allowing n to be an adjustable parameter. The three-parameter BET equation is then

$$V = \frac{V_m c P/P_0}{1 - P/P_0} \frac{1 - (n+1)(P/P_0)^n + n(P/P_0)^{n+1}}{1 + (c-1)P/P_0 - c(P/P_0)^{n+1}}, \quad (43)$$

where P , P_0 , V , V_m and c are defined as they were in equations (41) and (42), and n is the maximum number of layers of the adsorbing gas and is related to the pore size and properties of the adsorbent. As a result, multilayer formation of adsorbing gas is limited to n layers at large values of P/P_0 . Equation (43) models experimental data well when a finite number of layers are observed for adsorption of gases on a porous surface.

The three-parameter BET equation was used to obtain a fit to the experimental data. The parameters n , V_m and c can be calculated according to the method described by Joyner *et al.* (1945), in which equation (43) is rearranged into the linear form

$$\frac{\Phi(n, x)}{V} = \frac{1}{V_m C} + \frac{\theta(n, x)}{V_m}, \quad (44)$$

where

$$\Phi(n, x) = \frac{X[(1 - X^n) - nX^n(1 - X)]}{(1 - X)^2}, \quad (44 a)$$

$$\theta(n, x) = \frac{X(1 - X^n)}{1 - X} \quad (44 b)$$

and

$$X = \frac{P}{P_0}. \quad (44 c)$$

Plots of $\Phi(n, x)/V$ versus $\theta(n, x)$ are made while changing the value of n from 1 to 9 until the best straight line through the experimental data points is determined. The constants V_m and c are then calculated from the slope and intercept of the straight line.

The coverage of adsorbed H₂O on α -Al₂O₃ particles is quantified in terms of the number of adsorbed H₂O layers in the following way. Since the IR data were analysed in terms of the integrated absorbance of the bending mode, V_m is replaced by I_m (units of integrated absorbance) in the above equations, and V is replaced by I (the integrated absorbance of the H₂O bending absorption mode of surface-adsorbed H₂O). The integrated absorbance I_m for one monolayer is determined from plots of $\Phi(n, x)/I$ versus $\theta(n, x)$, in the same way as V_m is determined in the discussion above. The number of adsorbed H₂O layers at any value of P/P_0 is just the integrated absorbance at that pressure divided by I_m (i.e. the number of H₂O layers which is equal to I/I_m). Using this analysis, the number I/I_m of adsorbed H₂O layers versus RH P/P_0 is shown as the line through the data in the inset in figure 24. The RH, corresponding to one monolayer of H₂O adsorbed on the oxide surfaces is indicated in the figure. From this analysis for α -Al₂O₃ and other oxide particles, the following number of H₂O layers are estimated to be on the surface of oxide particles: about one monolayer at 20% RH, two to three adsorbed H₂O layers at 50% RH and three to four adsorbed H₂O layers at 85% RH, depending on the oxide surface. Our coverage estimates agree with studies of H₂O adsorption versus RH on α -Al₂O₃ powder, which show that, under typical atmospheric conditions (298K and 50–60% RH), about three monolayers of H₂O are adsorbed on Al₂O₃ surfaces (Yan *et al.* 1987).

The standard enthalpy ΔH_1 of adsorption of H₂O vapour on the oxide surfaces was calculated from the parameter c in equation (42). The ΔH_1 value is determined to be $-52.0 \text{ kJ mol}^{-1}$ and is greater than the standard enthalpy of condensation of H₂O vapour: $\text{H}_2\text{O(g)} \rightarrow \text{H}_2\text{O(l)}$, $\Delta H_2 = -44.0 \text{ kJ mol}^{-1}$.

The water adsorption isotherm shown in the inset of figure 24 was also measured as a function of decreasing RH. Full circles represent data when H₂O vapour was added to the IR cell containing the oxide particles with increasing RH. Open circles represent data when the H₂O vapour pressure has been evacuated and lowered. Because the number of H₂O layers decreases when the H₂O vapour pressure is lowered (as indicated by the open circles) and follows the same path as integrated absorbance for increasing RH, H₂O adsorption on the hydroxylated-covered α -Al₂O₃ surface shows no significant hysteresis, indicating reversible adsorption. In addition, there is no change in the H₂O adsorption isotherm for α -Al₂O₃ that has been previously reacted with HNO₃ (as indicated by the open squares). The only change observed in the FTIR spectrum is the nitrate ion spectrum which goes from oxide-coordinated to H₂O-solvated nitrate as a function of RH. The uptake of H₂O on nitrate-covered α -Al₂O₃ demonstrates this change (figure 25).

The uptake coefficient for reaction of HNO₃ on α -Al₂O₃ and CaO in the presence and absence of H₂O vapour is calculated via equation (24) by the same procedure outlined above. The uptake coefficient for HNO₃ on α -Al₂O₃ and CaO increased by as much as two orders of magnitude as RH increased from 0 to 16%. The increase in the uptake coefficient on the wetted surface as a function of RH is shown in figure 26. The open circles represent the enhancement in the reactive uptake coefficient $\gamma_{\text{wet}}/\gamma_{\text{dry}}$ of HNO₃ on α -Al₂O₃ and CaO particles as a function of RH. The data are collected only up to 17% RH because the rate of adsorption became too fast to measure. The solid curve represents the BET isotherm fitted for H₂O adsorption on α -Al₂O₃ and CaO particles in which the parameter V_m , the volume of adsorbed H₂O on the oxide particles corresponding to a coverage of one monolayer, was replaced by γ_m , the uptake coefficient measured at a H₂O coverage of one monolayer, in

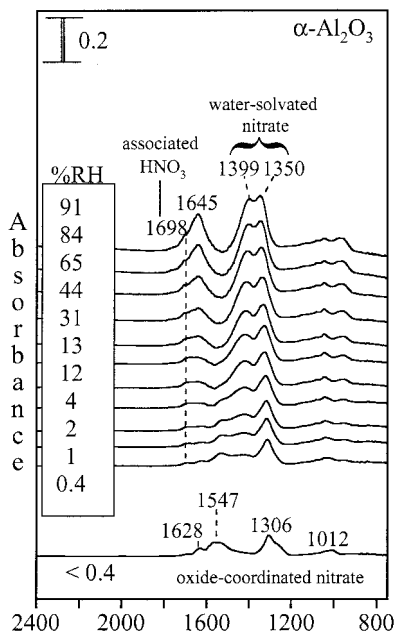


Figure 25. FTIR spectra of H_2O uptake on $\alpha\text{-Al}_2\text{O}_3$ particles previously reacted with HNO_3 . The spectra show conversion of oxide-coordinated surface nitrate to H_2O -solvated nitrate with increasing RH.

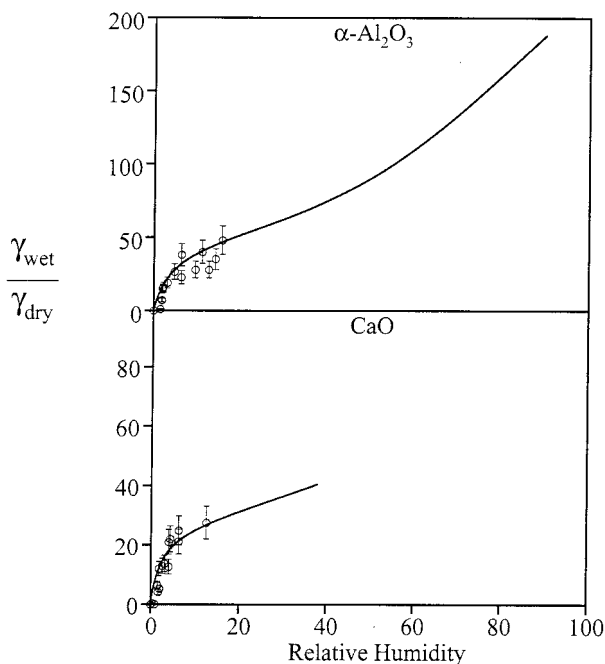


Figure 26. Enhancement of the reactive uptake as a function of RH for heterogeneous reaction of HNO_3 on $\alpha\text{-Al}_2\text{O}_3$ and CaO particles: (O), $\gamma_{\text{wet}}/\gamma_{\text{dry}}$ as a function of RH; (—), modified BET isotherm fit for H_2O adsorption on $\alpha\text{-Al}_2\text{O}_3$ and CaO particles as determined previously except now calibrated to $\gamma_{\text{m,wet}}$ (see text for further details).

equation (43), as suggested in a recent paper by Davies and Cox (1998) for HNO₃ uptake on NaCl. This equation can be written as

$$\gamma_{\text{wet}} = \frac{\gamma_{\text{wet,m}} c P/P_0}{1 - P/P_0} \frac{1 - (n+1)(P/P_0)^n + n(P/P_0)^{n+1}}{1 + (c-1)P/P_0 - c(P/P_0)^{n+1}}. \quad (45)$$

Thus, the BET parameters for the isotherm curve for H₂O uptake on α -Al₂O₃ particles become $\gamma_{\text{wet,m}} = 1.82 \times 10^{-6}$ at 16% RH with $c = 25.2$ and $n = 8$. In the case of CaO, the BET isotherm curve for H₂O uptake on nitrate-covered CaO particles was used to model the γ dependence. Similar to CaCO₃, the H₂O uptake capacity of CaO increased after reaction with HNO₃. The parameters for CaO are $\gamma_{\text{wet,m}} = 9.90 \times 10^{-6}$ at 13% RH with $c = 39.7$ and $n = 4.1$. The ratio $\gamma_{\text{wet}}/\gamma_{\text{dry}}$ as a function of RH and the calculated $\gamma_{\text{wet}}/\gamma_{\text{dry}}$ from the H₂O isotherm curve shows that the HNO₃ uptake rate on oxide particles is enhanced in the presence of H₂O vapour and that this enhancement can be understood in terms of the increased adsorbed H₂O layers on the oxide particles.

4.5. Knudsen cell studies on the effect of surface-adsorbed H₂O on the heterogeneous reactivity of HNO₃ on oxide and mineral dust particles

Some investigations into the effect of surface H₂O were also performed in the Knudsen cell apparatus. It has been demonstrated by IR spectroscopy that, even after pumping overnight, oxide powders can still retain some adsorbed H₂O. The reactivity of these comparatively 'wet' samples were compared with samples which had been heated. The results for CaO and Gobi dust are plotted in figure 27 where it can be seen that even a small change in the amount of H₂O on the surface can have a significant effect in the uptake coefficient (a factor of 27 for CaO and a factor of ten for Gobi dust), similar to what is observed in some IR experiments.

4.6. Corrections needed to the box-model analysis

The data presented in this section demonstrate that atmospheric chemistry models that include heterogeneous reactions should also include RH dependence for these reactions. In the case of HNO₃ uptake, we have clearly demonstrated that there is a strong dependence on RH and adsorbed H₂O on the reactive uptake. The reaction rate is significantly enhanced (20–50 times) for a particle that contains one to two layers of adsorbed H₂O compared with a dry particle surface. In addition, it is shown for some mineral aerosol particles that the reaction may not just be limited to the surface of the particle. The heterogeneous reaction of HNO₃ modelled in section 3 under dry conditions showed that this reaction can have an effect on gas-phase HNO₃ concentrations. This effect is certainly even greater under conditions of RH found in the troposphere.

5. Heterogeneous formation of HONO on solid aerosol particles

5.1. The importance of HONO in the troposphere

Hydroxyl radical is the most important trace species in atmospheric oxidation mechanisms (Chan *et al.* 1976, Cox 1984). While it is clear that O₃ photolysis is the main source of OH radicals in the stratosphere, mechanisms for OH radical formation in the troposphere are still being debated. One source of hydroxyl radical is from the photodissociation of HONO, as HONO undergoes photolysis at wavelengths between 330 and 380 nm (Baulch *et al.* 1982):

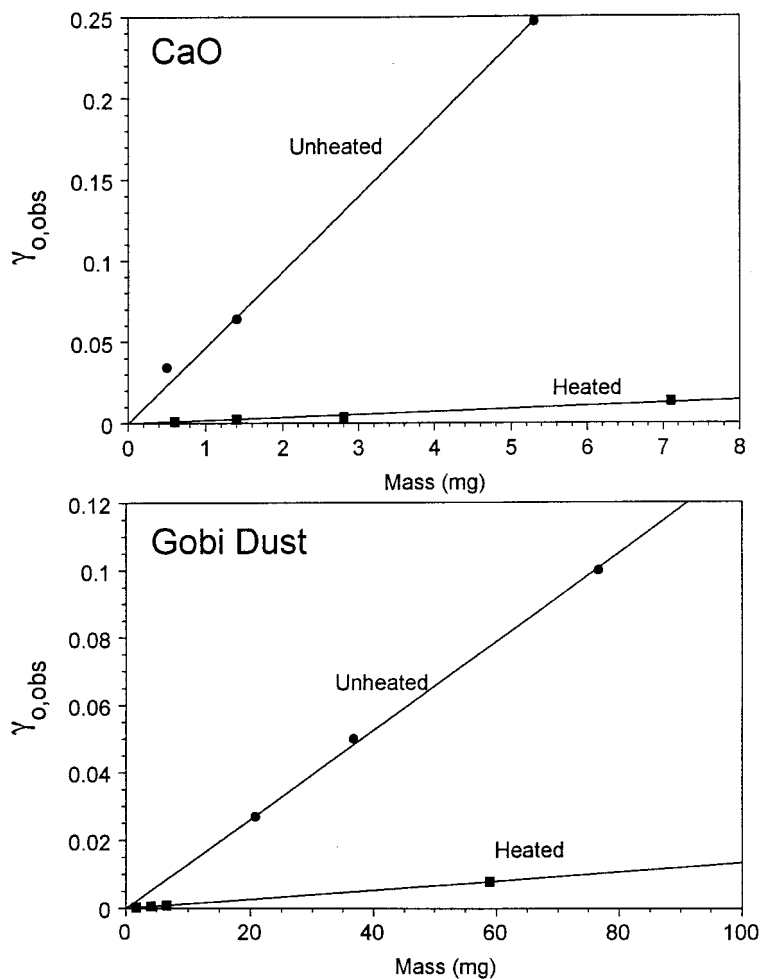
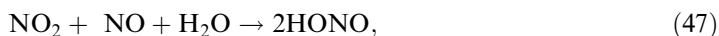


Figure 27. Initial uptake coefficients calculated using equation (8) for unheated and heated samples of both CaO and Gobi dust: (●), samples that have been evacuated overnight but not heated and thus have a small amount of H₂O adsorbed on the surface; (■), samples for which much of the H₂O has been removed by heating to 40°C overnight under vacuum. For CaO, the slopes of the liners are $y = 0.0467x$ and $y = 0.0017x$ for unheated and heated samples respectively. Using equation (33) and the information in table 1, the initial uptake coefficients become 6.2×10^{-3} and 2.3×10^{-4} for unheated and heated samples respectively.



Although HONO concentrations up to 14 ppb have been observed in polluted urban environments, HONO formation is not well understood (Appel *et al.* 1990, Febo *et al.* 1996). Lee and Schwartz (1981) have shown that the following reactions are too slow in the gas and aqueous phases to be relevant under atmospheric conditions:



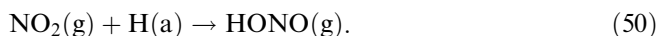
Evidence suggests, however, that these reactions may occur at a faster rate by a heterogeneous or surface-catalysed mechanism (Kaiser and Wu 1977, Sakamaki *et al.* 1983, Pitts *et al.* 1984, Finlayson-Pitts and Pitts 1986, Svensson *et al.* 1987, Jenkin *et al.* 1988, Febo and Perrino 1991, Junkermann and Ibusuki 1992, Notholt *et al.* 1992, Becker *et al.* 1996, Harrison *et al.* 1996, Lammel and Cape 1996, Kleffmann *et al.* 1998). In fact, surface reactions may be responsible for as much as 95% of all the HONO found in the troposphere (Pitts *et al.* 1984, Svensson *et al.* 1987, Jenkin *et al.* 1988). A recent review article discussed the evidence presented for heterogeneous reaction of NO₂ to produce gas-phase HONO in humid environments (Lammel and Cape 1996). The reaction proceeds over a wide variety of surfaces including those of glass, sodium halides, metals and metal oxides.

Several laboratory studies have reported that heterogeneous HONO formation via reaction (48) is first order in both NO₂ and H₂O (Pitts *et al.* 1984, Svensson *et al.* 1987, Jenkin *et al.* 1988, Lammel and Cape 1996, Finlayson-Pitts and Pitts 1986),

$$\frac{d[\text{HONO}]}{dt} = k[\text{NO}_2][\text{H}_2\text{O}], \quad (49)$$

with the rate-limiting step being adsorption of NO₂. Using environmental chambers containing NO₂ and H₂O, Sakamaki *et al.* (1983) and Pitts *et al.* (1984) proposed that reaction (48) provides the best model for the heterogeneous formation of HONO although no HNO₃ was directly detected. Therefore, without full characterization of all the reactants and products in reaction (48), the reaction has been considered somewhat speculative (Finlayson-Pitts and Pitts 1986). The lack of any observable HNO₃ in the gas phase has been explained by the suggestion that it sticks to the walls of the environmental chamber. This suggestion is supported in some recent experiments in which HNO₃ was detected via *ex-situ* measurements (Kleffmann *et al.* 1998).

Heterogeneous reactions on carbonaceous aerosol may also provide a reactive surface for formation of HONO in the atmosphere. The heterogeneous reaction of nitrogen oxides, and in particular NO₂, on carbonaceous aerosol has been studied by several groups using a variety of experimental techniques (Akhter *et al.* 1984, Smith *et al.* 1988, Chughtai *et al.* 1990, Rogaski *et al.* 1997, Ammann *et al.* 1998, Gerecke *et al.* 1998, Kalberer *et al.* 1999a, b, Kleffmann *et al.* 1999, Longfellow *et al.* 1999). It has been shown that NO₂ can react with soot particles to produce HONO (Ammann *et al.* 1998, Gerecke *et al.* 1998, Kalberer *et al.* 1999a, b, Kleffmann *et al.* 1999, Longfellow *et al.* 1999). It has been proposed that this reaction on soot (reaction (50)) may account for the high concentration of HONO observed during the nighttime when the homogeneous reaction is insignificant:



However, there is a range of values reported for the heterogeneous uptake coefficient of NO₂ on soot, from 0.095 to 10⁻⁶, a range that spans nearly five orders of magnitude. This discrepancy in the values of the uptake coefficient arises in part because soot samples are often from different sources. Commercial soot differs from freshly prepared soot and even the latter can be prepared in different ways using different hydrocarbons. This means that, from study to study, soot particles can have different chemical composition, different sizes, different BET surface areas and, therefore, different reactivities. Experimental conditions such as temperature, RH and pressure of NO₂ also varied from one study to study. Another source of

discrepancy is that the accessible surface area for reaction must be accurately accounted for when calculating uptake coefficients. NO_2 is believed to diffuse to the pores of soot samples and to access underlying layers of particles in bulk samples (Aumont *et al.* 1999, Kleffmann *et al.* 1999). However, in some of the above studies (Rogaski *et al.* 1997, Gerecke *et al.* 1998, Longfellow *et al.* 1999), only uptake on the first layer of soot was considered and thus the exposed geometric area of soot was used in calculating γ . This may explain the very high γ values reported in some studies compared with others. In addition, in all the studies discussed above, surface areas were not measured for the soot samples under investigation. This is usually done using the BET method and N_2 as the adsorbent molecules. Instead, values were taken from the literature which may or may not accurately represent the true values because of differences in sample preparation. The fractal nature of soot also makes the characterization of the available surface area difficult. As noted by Longfellow *et al.* (1999), in order to apply laboratory measurements of the heterogeneous uptake measurements to the atmosphere, the surface area of the soot must be considered. One other difference in the literature values is that the initial uptake coefficients are reported in some cases whereas a steady state or an average value is reported in others. This means that the reactivity of a surface covered with adsorbed molecules is compared with the reactivity of the unreacted surface. Because of site-blocking, adsorbate–adsorbate interactions and electronic effects, uptake coefficients are typically coverage dependent and usually decrease as a function of coverage (Masel 1996).

In order to have a greater understanding of heterogeneous formation of HONO in the global troposphere, FTIR, Knudsen cell and aerosol chamber experiments have been conducted for the NO_2 reaction on wetted SiO_2 particles, to investigate reaction (48), and soot, to investigate reaction (50). These experiments are described in the following sections.

5.2. Spectroscopic measurements of the heterogeneous reaction of NO_2 on soot and wetted SiO_2 particles

In contrast with the oxides investigated in section 2, there is little change in the spectrum of SiO_2 upon exposure of dehydrated SiO_2 to NO_2 (figure 28, curve *a*). However, when NO_2 is added to the IR cell containing hydrated SiO_2 with a surface coverage of approximately 0.08 monolayers of adsorbed H_2O , absorption bands appear in the SiO_2 spectrum at 1677, 1399 and 1315 cm^{-1} (figure 28, curve *b*). As discussed below, these bands can be assigned to the vibrational modes of adsorbed HNO_3 . In the presence of gas-phase H_2O at a RH of 4%, the bands assigned to HNO_3 increase in intensity and an increase in intensity of the bending mode of adsorbed H_2O at 1624 cm^{-1} (figure 28, curve *c*) is also observed. As discussed above, there is an increase in the amount of adsorbed H_2O on the surface by a factor of nearly ten for the surface labelled 4% RH relative to that labelled hydrated. The assignment of the bands to adsorbed HNO_3 is confirmed by the spectrum of an authentic sample of HNO_3 adsorbed on SiO_2 (figure 28, curve *d*). The three bands in the spectrum can be assigned to the $\nu_a(\text{NO}_2)$ (1677 cm^{-1}), $\delta(\text{OH})$ (1399 cm^{-1}) and $\nu_s(\text{NO}_2)$ (1315 cm^{-1}) modes of adsorbed HNO_3 . These bands are shifted by 10–68 cm^{-1} from the gas-phase HNO_3 frequencies (Shimanouchi 1977) but compare well with the IR spectrum of HNO_3 in highly concentrated aqueous solution which has absorptions at 1670 and 1300 cm^{-1} that are assigned to the $\nu_a(\text{NO}_2)$ and $\nu_s(\text{NO}_2)$ modes respectively (Leuchs and Zundel 1978). The OH stretching region

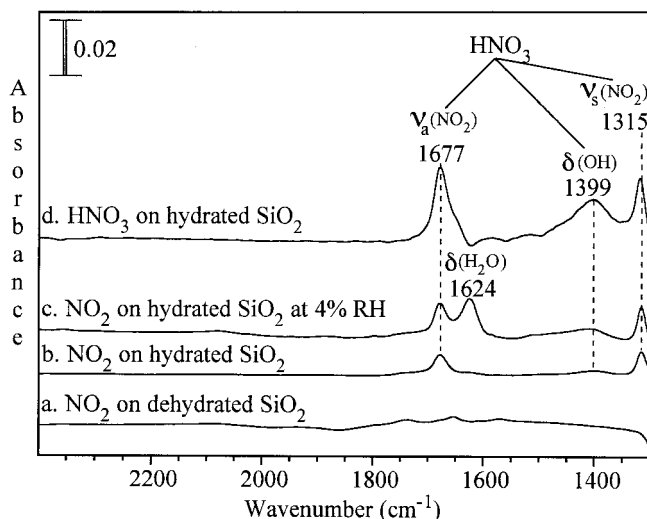


Figure 28. Transmission FTIR spectra of SiO_2 particles that differ in H_2O coverages. For samples labelled dehydrated SiO_2 , the particles were heated to 673 K to remove all adsorbed H_2O and some surface hydroxyl groups. For samples labelled hydrated SiO_2 , the particles were exposed to H_2O vapour at 10 Torr or more and subsequently evacuated to pressures of the order of 1×10^{-4} Torr. For samples labelled 4% RH SiO_2 , the particles were in equilibrium with gas-phase H_2O corresponding to a RH of 4%. (Reproduced with permission from Goodman *et al.* (1999). Copyright 1999 American Chemical Society.)

(not shown) is complicated and showed an intense broad absorption band extending from 3700 cm^{-1} to as low as 2700 cm^{-1} . This broad band is most probably due to the hydrogen bonding interaction between HNO_3 and H_2O . Experiments carried out with adsorbed D_2O confirm these assignments (Goodman *et al.* 1999)

According to reaction (48), the production of gas-phase HONO is also expected from the heterogeneous reaction of NO_2 on hydrated SiO_2 particles. The gas-phase spectrum obtained by reacting NO_2 on hydrated SiO_2 followed by the addition of gas-phase H_2O at a RH of 24% is shown in figure 29, curve *a*. Because absorption bands of H_2O overlap the region where HONO bands are expected, the H_2O spectrum, as shown in figure 29, curve *b*, was subtracted from the spectrum shown in figure 29, curve *a*. In the difference spectrum (figure 29, curve *c*), bands at 3591 , 1703 and 1264 cm^{-1} became apparent. Based on literature assignments, the bands at 3591 , 1703 and 1264 cm^{-1} are assigned to the $\nu(\text{OH})$, $\nu(\text{N}=\text{O})$ and $\delta(\text{HON})$ modes respectively of gas-phase *trans*-HONO (Jacox 1990). In these experiments, NO is also present in the spectrum at 1876 cm^{-1} . Sakamaki *et al.* (1983) and Pitts *et al.* (1984) also reported NO production and suggested that NO may come from wall reactions of HONO. In other experiments, we have observed some NO production from wall reactions of NO_2 as well.

Previous to this study, a full *in-situ* characterization of the products of the reaction $2\text{NO}_2(\text{g}) + \text{H}_2\text{O}(\text{a}) \rightarrow \text{HONO}(\text{g}) + \text{HNO}_3(\text{a})$ has not been made. This is the first direct evidence for the surface reaction between gas-phase NO_2 and adsorbed H_2O to yield both adsorbed and gas-phase products.

The NO_2 soot reaction was also examined by FTIR spectroscopy (Al-Abadleh and Grassian 2000). The FTIR data show that adsorbed products remain on the surface for the NO_2 -soot reaction as well. Figure 30 shows the FTIR spectra of

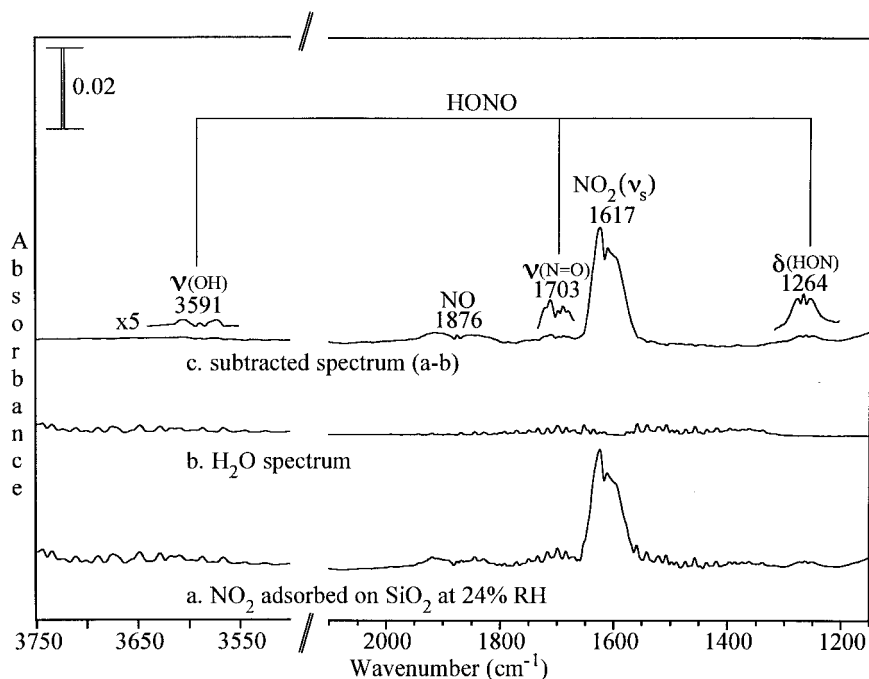


Figure 29. FTIR spectra of the gas phase after reaction of NO_2 (3.404 Torr) with hydrated SiO_2 in the presence of H_2O vapour (24% RH) (curve a) and of gas-phase H_2O (curve b), together with the difference spectrum (curve c, obtained from curve a minus curve b) to remove H_2O bands from spectrum a is shown. Absorptions due to *trans*-HONO (3591, 1703 and 1264 cm^{-1}), NO_2 (1617 cm^{-1}) and NO (1876 cm^{-1}) are present in the spectrum. (Reproduced with permission from Goodman *et al.* (1999) Copyright 1999 American Chemical Society.)

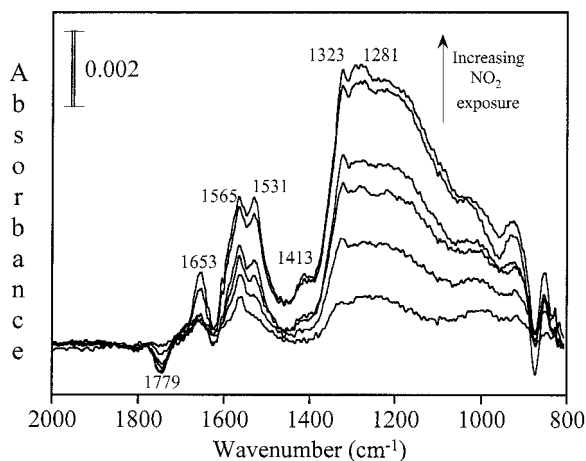


Figure 30. FTIR spectra of the hexane soot surface recorded as a function of NO_2 exposure. The assignment of these peaks are as follows; 1281 cm^{-1} , $-\text{R}-\text{ONO}$; 1323 cm^{-1} , $-\text{R}-\text{NO}_2$; 1413 cm^{-1} , $-\text{CO}_3^-$; 1531 cm^{-1} , $-\text{R}-\text{NO}_2$; 1565 cm^{-1} , $-\text{R}-\text{N}-\text{NO}_2$; 1653 cm^{-1} , $-\text{R}-\text{ONO}$; 1777 cm^{-1} , lactone and alkyl carbonyl groups. (Reproduced with permission from Al-Abadleh and Grassian (2000). Copyright 2000 American Chemical Society.)

hexane soot (1 mg) as a function of NO_2 exposure. The IR spectra recorded as a function of increasing exposure of NO_2 by increasing the pressure from 5 to 100 mTorr are shown in figure 30. These spectra were recorded in the presence of gas-phase NO_2 ; the unreacted soot surface is taken as the reference background spectrum. The spectra showing only surface-bound products show bands at 1281, 1323, 1413, 1531, 1565 and 1653 cm^{-1} that increase as the coverage of NO_2 is increased. These bands are associated with the following functional groups: 1281 cm^{-1} , $-\text{R}-\text{ONO}$; 1323 cm^{-1} , $-\text{R}-\text{NO}_2$; 1413 cm^{-1} , $-\text{CO}_3^{2-}$; 1531 cm^{-1} , $-\text{R}-\text{NO}_2$; 1565 cm^{-1} , $-\text{R}-\text{N}-\text{NO}_2$; 1653 cm^{-1} , $\text{R}-\text{ONO}$.

There is a decrease in the intensity of the band at 1777 cm^{-1} , suggesting the loss of $\text{C}=\text{O}$ group from the carbonyl surface, presumably owing to the formation of gas-phase carbon dioxide (CO_2) or carbon monoxide (CO) as has been observed in other studies performed at high pressures of NO_2 (Chughtai *et al.* 1990). Upon evacuation of the gas phase, the IR spectrum of the surface remains nearly identical with only a small decrease (less than 5%) in the intensity of the bands between 1400 and 1675 cm^{-1} .

5.3. Knudsen cell measurements of the heterogeneous reaction of NO_2 on wetted SiO_2 and soot

Knudsen cell measurements provided additional insight into the reaction of NO_2 and H_2O . In these experiments, the SiO_2 particles were covered with a lid while a steady-state flow of NO_2 was established. Once steady-state flow was reached, the lid was then opened to expose the particles to the gas. These measurements were carried out on SiO_2 particles that contained different amounts of adsorbed H_2O . SiO_2 particles evacuated overnight to a pressure of less than 1×10^{-6} Torr (labelled dehydrated SiO_2) showed no measurable loss of NO_2 from the gas phase, as seen in figure 31. SiO_2 particles evacuated for shorter periods of time did show a measurable amount of NO_2 uptake. Data are presented in figure 31 for SiO_2 particles that were exposed to H_2O at 10 Torr and 298 K followed by evacuation for 20 min. There is a decrease in the NO_2 flow rate and reaction on hydrated SiO_2 particles when the lid was open. There is an initial spike in the NO_2 flow rate, but then the flow rate approaches the steady-state value. The lid was closed again for 300 s and subsequently the oxide particles were exposed. The second time that the lid was open there was less of a decrease in the NO_2 signal and the reaction, as indicated by the NO_2 signal, dies off quickly.

The H_2O flow rate for the two SiO_2 samples, dehydrated and hydrated, is also shown in figure 31. The H_2O signal increases when the lid is open, indicating that H_2O is outgassing from the SiO_2 sample. There are several points that can be made concerning the H_2O desorption from the SiO_2 samples. First, the amount of H_2O coming from the SiO_2 sample labelled dehydrated is a factor of 100 times less than the SiO_2 . Second, the amount of adsorbed H_2O on the hydrated sample significantly decreases as the H_2O outgassed from the sample. Third, there is a concomitant decrease in the NO_2 uptake with the decrease in the amount of adsorbed H_2O . It was difficult to determine an uptake coefficient for this reaction as it is not clear how H_2O is distributed through the sample in these experiments; thus, the coverage of adsorbed H_2O is unknown.

It is easier to quantify the NO_2 soot reaction. In these experiments, soot is directly deposited on to the Knudsen cell sample holder which has an area of 11.95 cm^2 . The initial uptake coefficient for the reaction of NO_2 with hexane soot was

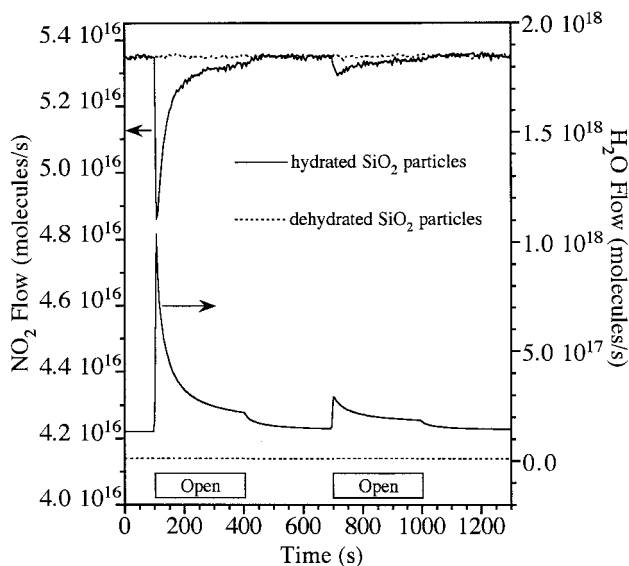


Figure 31. Flow cell reactor mass spectral data for the reaction of NO_2 on SiO_2 . The flow rate in molecules per second is shown for two gas-phase molecules, NO_2 (scale for the NO_2 flow is shown on the y axis on the left) and H_2O (scale for H_2O flow is shown on the y -axis on the right) during reaction on dehydrated and hydrated SiO_2 . At time $t = 100$ s, the sample holder is opened and there is a drop in the NO_2 flow rate as NO_2 reacts on the surface of hydrated SiO_2 particles (i.e. particles exposed to H_2O at 10 Torr overnight and evacuated for 20 min) but not dehydrated SiO_2 particles (i.e. particles evacuated overnight). The sample holder is then closed and the NO_2 signal returns to its baseline value. The process of exposing the surface to NO_2 was repeated once again. The plot also shows that there is a significant amount of H_2O outgassing from the hydrated but not from the dehydrated sample. (Reproduced with permission from Goodman *et al.* (1999). Copyright 1999 American Chemical Society.)

measured as a function of sample mass (and thus sample thickness). Representative Knudsen cell data are shown in figure 32. The QMS intensity of NO_2 ($m/e = 46$) was monitored during the experiment (figure 32 (a)). When the sample lid is open and the soot particles are exposed to the reactive gas, there is a decrease in the QMS intensity. The QMS intensity of NO_2 is then converted to the observed uptake coefficient via equation (8), as shown in figure 32 (b). The initial observed uptake coefficient $\gamma_{0,\text{obs}}$ is taken as the maximum value for γ and found to be 0.018 from the data shown in figure 32 (b). It can be seen from the data plotted in figure 32 (b) that over time the value of the uptake coefficient decreases as the reaction proceeds. This decrease occurs because the surface becomes less reactive with continued reaction of NO_2 and is interpreted as a coverage-dependent uptake coefficient.

HONO is detected as a product in the NO_2 reaction with soot. The QMS intensity for the parent ions of NO_2 and HONO, $m/e = 46$ and 47, respectively, were calibrated and converted to molecular flow through the Knudsen cell. These data are shown in figure 32 (c). The flow of NO_2 has been offset and inverted to show the amount of NO_2 that reacts per second. The $m/e = 47$ signal from the mass spectrometer contains two contributions: the parent ions of HONO and the natural abundance ^{15}N labelled NO_2 . Calibration of the $m/e = 47$ signal for HONO production was carried out according to the procedure outlined in section 2. From the calibrated data presented in figure 32 (c), the amount of HONO produced per

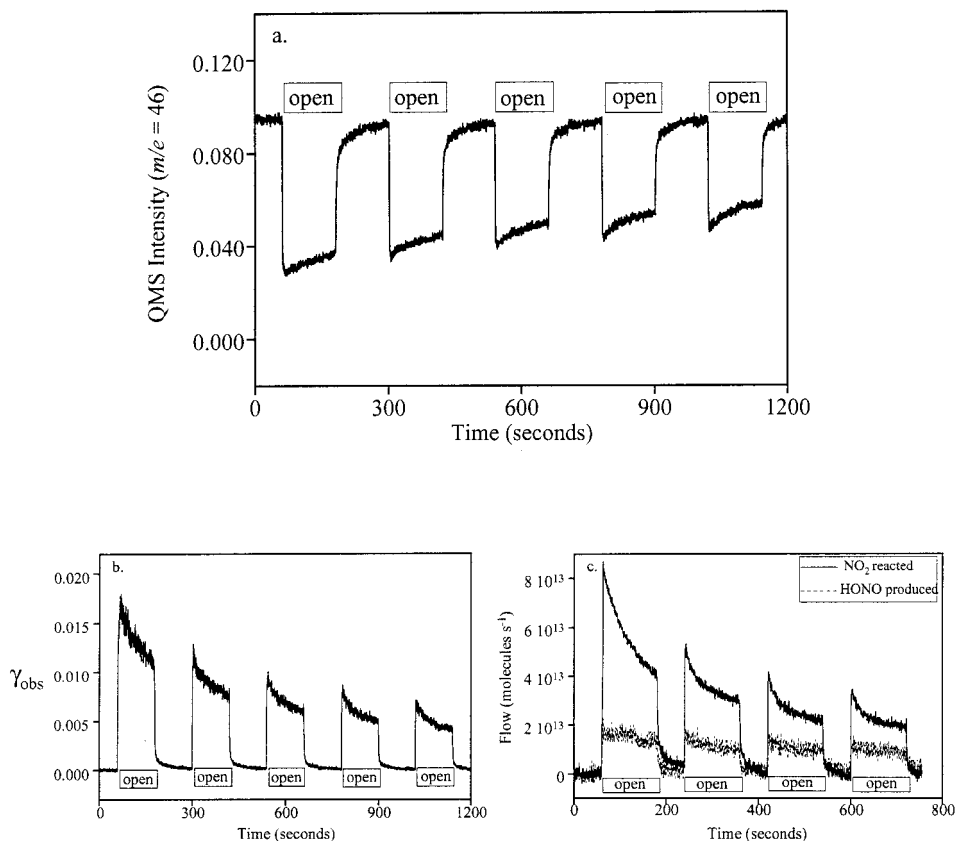


Figure 32. (a) Knudsen cell data for the heterogeneous reaction of NO_2 on soot (15.1 mg sample). The QMS intensity for $m/e = 46$ is shown. (b) Observed uptake coefficient calculated via equation (8) from the data shown in (a). (c) Calibrated flow of NO_2 reacted and HONO produced (7.7 mg sample).

NO_2 reacted is determined to be $36 \pm 5\%$. The remaining NO_2 taken to the surface may correspond to the formation of surface-bound products (*vide infra*) and other gas products such as NO. The percentage of HONO produced in this study is lower than that reported in another Knudsen cell study (Gerecke *et al.* 1998). This may be a result of using different hydrocarbon as a soot generator and collecting soot at different heights from the flame base.

From the calibrated data it is also possible to determine the absolute number of NO_2 molecules reacted per unit surface area (or unit mass of soot). For small masses of soot (less than 1 mg), complete saturation of the surface can be obtained by continuing the reaction until no further uptake of NO_2 is observed. This means that over time the uptake coefficient goes to zero. The data in figure 32(c) can be used to determine the total amount of NO_2 reacted per unit surface area. For thin- or low-mass samples, complete saturation occurs over the time period of the experiment whereas, for thicker samples with larger mass, the data are fitted to a double exponential form and the fit is then extrapolated to the limit of no further uptake of NO_2 corresponding to a saturated surface. From all the data, it is determined that the total amount of NO_2 that can react at a pressure near $8 \mu\text{Torr}$ is determined to be

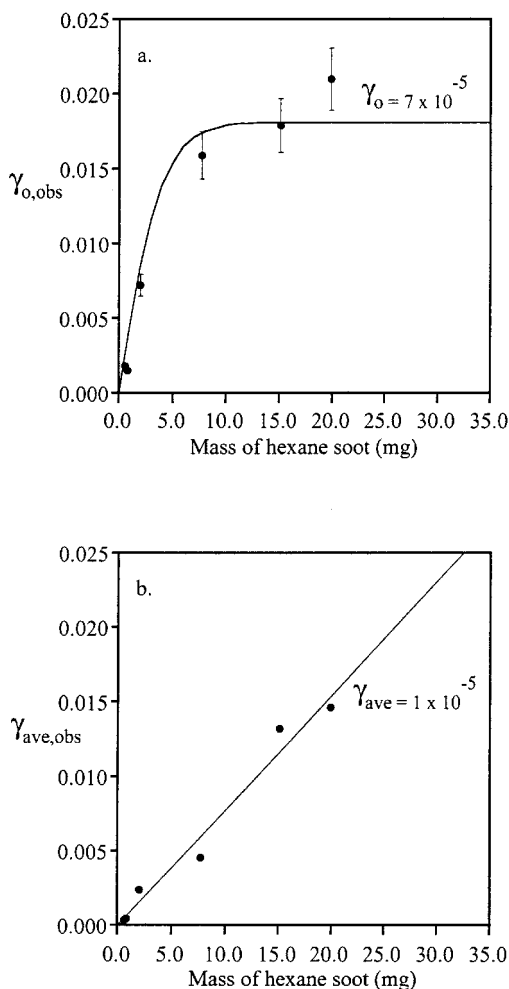


Figure 33. (a) The mass dependence (thickness dependence) of the initial uptake coefficient for the reaction of NO_2 with hexane soot: (●), experimental data; (—), result of a KML fit to the data. The experimental and fitting parameters used in the model are as follows: $\rho_b = 0.1 \text{ g cm}^{-3}$; $\rho_t = 2.0 \text{ g cm}^{-3}$; $d = 3.9 \times 10^{-6} \text{ cm}$; $S_{\text{BET}} = 760 \text{ cm}^2 \text{ mg}^{-1}$; $\tau = 1$; $\gamma_{0,t} = 7 \times 10^{-5}$. (b) The mass dependence of the average uptake coefficient, averaged over 120 s: (●), experimental data; (—), linear least-squares fit to the data of the form $y = mx$. The slope of the fit is $7.7 \times 10^{-4} \text{ mg}^{-1}$ with an R factor of 0.986.

$1.4 \pm 0.5 \times 10^{13} \text{ molecules cm}^{-2}$. This value is used as the saturation coverage for NO_2 on soot at 295 K and a pressure of $8 \mu\text{Torr}$.

In some experiments, the parent peak of HNO_3 ($m/e = 63$) was monitored. No change in the mass spectral intensity of HNO_3 was observed, suggesting that HNO_3 is not formed as a gaseous reaction product. This result agrees with the study by Kalberer *et al.* (1999) in which HNO_3 was not detected either in the gas phase or adsorbed on the aerosol particles or the walls of the reactor.

The value of the observed initial uptake coefficient is found to depend on the number of layers of soot present. The observed initial uptake coefficient measured as a function of the sample mass is plotted in figure 33(a). Since the sample holder is of a fixed area, 11.95 cm^2 , increasing the sample mass increases the number of layers of

soot. The line through the data is determined from the KML gas diffusion model as discussed in section 2.3.1. This is an empirical model that accounts for gas diffusion into porous samples and corrects the observed uptake coefficient for contribution from underlying layers of particles. The parameters listed in the figure caption were used as input data in the diffusion model for the reaction of NO_2 with hexane soot. There are two parameters that are adjusted in order to obtain a good fit: the true initial uptake coefficient $\gamma_{0,t}$ that takes into account the accessible surface area of the underlying layers and the tortuosity τ which is related to the diffusion of the molecules through the sample. A value of 1 for the tortuosity and a value of 7×10^{-5} for the true initial uptake gave the best fit to the data.

As discussed previously, there are two distinct regions in the plot shown in figure 33(a). The region that extends from 0 to approximately 8 mg shows that the observed initial uptake coefficient has a nearly linear dependence on sample mass. The portion of the plot above 8 mg shows that the observed initial uptake coefficient is independent of the sample mass. The region above 8 mg shows that the probe depth of the gas-phase molecules measured during this initial time is constant and equivalent to the probe depth reached for a sample of mass of 8 mg. In other words, on the time scale of the measurement of the initial uptake coefficient, NO_2 molecules are diffusing into a portion of the soot sample estimated to be only of the order of 1000 layers. For thin samples, the time scale for the observed uptake coefficient to reach its maximum value is of the order of the residence time (approximately 2 s). For a sample mass of 7.7 mg, this time scale is slightly longer, of the order of 3.5 s for the molecules to diffuse through all the underlying layers.

Also shown in figure 33 is an average observed uptake coefficient calculated over a 120 s time period. The data plotted in figure 33(b) show $\gamma_{\text{ave,obs}}$ as a function of mass of n-hexane soot. It is seen that $\gamma_{\text{ave,obs}}$ is a linear function of sample mass over the entire range. The average uptake coefficient can be corrected for the accessible BET area using a linear least-squares fit of the line through the data points. This correction is then obtained from equation (33). The value calculated for $\gamma_{\text{ave,obs}}$ is 1×10^{-5} . This is a factor of six lower than the initial value of the uptake coefficient. Although the application of the diffusion model in figure 33(a) predicts a nearly linear mass regime to be in the range from 0 to 8 mg for the initial uptake coefficient, the dependence of the average uptake coefficient on the mass is still linear up to 19 mg.

Aerosol chamber results for the NO_2 -soot reaction are shown in figure 34. The FTIR spectra of NO_2 before and after soot is introduced into the aerosol chamber are shown in the main part of figure 34. Initially NO_2 (10 mTorr) in dry N_2 is introduced into the chamber and is monitored for 3 h in order to characterize any wall reactions. After this time, soot aerosol is injected into the chamber and FTIR spectra are collected every 3 min. The inset of figure 34 shows the FTIR data before soot injection, immediately after soot injection and several hundred minutes after soot injection. It can be seen that over time the NO_2 band at 1616 cm^{-1} decreases in intensity as the NO_2 reacts with the soot aerosol. Immediately after injection of the soot aerosol, it can be seen that the baseline of the IF spectrum is no longer flat as the suspended soot particles scatter IR light. The main part of figure 34 shows the decay of the NO_2 signal (integrated area of the 1616 cm^{-1} band) as a function of time. The decay curve is then fitted to an exponential decay and analysed as outlined in section 2.3.3. From this analysis, a time-averaged uptake coefficient is derived. From an analysis of the data shown in the inset and six other similar experiments, an

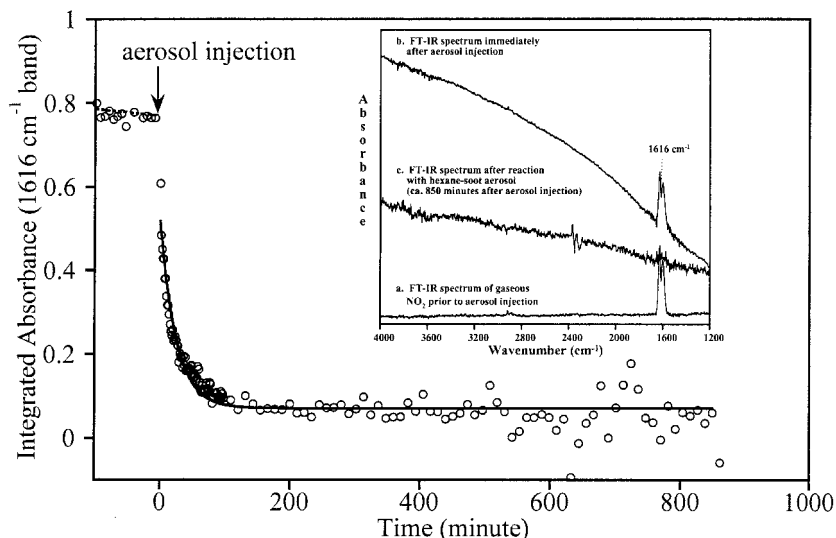


Figure 34. Heterogeneous reaction kinetics for gas-phase NO_2 on soot measured in the aerosol reaction chamber. Typical experimental data are shown above. In the main part of the figure, the integrated absorbance of the 1616 cm^{-1} band of gas-phase NO_2 is plotted as a function of time. At time $t = 0$, the soot aerosol is injected into the chamber and there is a decrease in the NO_2 integrated absorbance. The curve is fitted to an exponential decay in order to determine a first-order rate constant for the adsorption process. The uptake coefficient was then calculated from k_a via equation (27) and is found to be $3 \pm 2 \times 10^{-8}$, from an average of six experiments. The inset shows the FTIR spectrum of NO_2 prior to the injection of the soot aerosol (curve a), the FTIR spectrum of NO_2 immediately after the injection of the soot aerosol (curve b) (the shift in the baseline is due to scattering of the soot aerosol) and the FTIR spectrum after nearly all the NO_2 is reacted with the soot aerosol (curve c) (the shift in the baseline is associated with soot deposited on the IR windows and soot aerosol).

uptake coefficient of $3 \pm 2 \times 10^{-8}$ is derived. This time-averaged uptake coefficient is even smaller than that reported above because it is averaged over much longer time scales and thus longer surface coverages.

5.4. Atmospheric relevance and box-model analysis

In this study we have demonstrated that wetted SiO_2 and soot aerosol can react with NO_2 to produce HONO. Two questions that can be asked are as follows: do these reactions contribute to the formation of HONO in the global troposphere and do they contribute to NO_2 ?

The reaction probability of the heterogeneous reaction of NO_2 and H_2O , according to reaction (48) has been investigated and discussed. According to Saliba *et al.* (2000), this reaction could account for 0.9 ppb of HONO over an 8 h period. For the NO_2 reaction with soot (reaction (50)), it has been estimated that this reaction could generate over ten times more HONO than that due to the heterogeneous reaction of NO_2 and H_2O (Aumont *et al.* 1999). However, for the NO_2 -soot reaction, surface deactivation was not taken into account. The laboratory studies presented here indicate that the soot surface does in fact deactivate with time and the production of HONO from this reaction will be significantly less. Further analysis of this reaction would require additional experimentation under more

atmospherically relevant conditions that span the temperature and RH range of the troposphere. Using the uptake coefficients measured here and the modelling analysis from section 3, the loss of NO₂ from the atmosphere due to HONO production appears to be negligible.

6. Heterogeneous uptake of volatile organic compounds on oxide, carbon black and mineral dust particles

6.1. The importance of carbonyl compounds in the troposphere

Carbonyl compounds play an important role in the photochemical oxidant cycle, being produced by the photo-oxidation of most VOCs and in turn serving as an important source of peroxy radicals and peroxyacyl nitrates (Pandis and Seinfeld 1999). However, little is known about carbonyls in the troposphere, since only a few are routinely measured in monitoring programmes and measurement campaigns (most commonly measured are formaldehyde, acetaldehyde and acetone).

A recent study by Grosjean *et al.* (1996) identified 23 carbonyls (with an additional 19 tentatively identified) in the Los Angeles metropolitan area. The three most commonly measured carbonyls accounted for 28% of the total OH removal capacity by carbonyl compounds. In addition, the total OH removal capacity of the carbonyls identified is estimated to be four times that due to observed levels of toluene and isopentane, the two most abundant hydrocarbons in urban air. Recent studies have shown the presence and importance of carbonyls in regional (Tanner *et al.* 1996) and clean marine air (Ayers *et al.* 1997). Lee *et al.* (1998) assessed the role of formaldehyde as a peroxy radical source in the Nashville SOS'95 summer experiment and found it to account for 20% of the radicals during high-sun conditions, and over 60% during early morning and late afternoon. On the global scale, Singh *et al.* (1994) estimate that photolysis of acetone, one of the most dominant VOC species in the middle to upper troposphere, represents a significant source of polyacrylonitrile and free radicals. Model calculations suggest that in the upper troposphere loss of acetone by photolysis provides a HO_x source which is five times that due to the O(¹D) + H₂O reactions (Arnold *et al.* 1997, Singh *et al.* 1997). Similar reactions of other abundant higher-carbon-number carbonyls are expected to play an analogous role.

Little is known about the heterogeneous chemistry of VOCs on aerosol surfaces or its overall significance. Laboratory studies to quantify which reactions take place on aerosol surfaces and how these reactions affect the photochemical oxidant cycle are needed to address this issue. There have been some laboratory studies on the heterogeneous chemistry of some of the more abundant hydrocarbons in the atmosphere including formaldehyde (Jayne *et al.* 1996, Iraci and Tolbert 1997) and acetone (Duane *et al.* 1993, Duncan *et al.* 1999, Kane *et al.* 1999, Klassen *et al.* 1999). For acetone, it has been shown that the chemistry can be quite complex under certain conditions. For example, Duncan *et al.* (1999) and Kane *et al.* (1999) have shown that acetone can react on liquid sulphuric acid surfaces to yield higher-molecular-weight hydrocarbons including mesityl oxide (4-methyl-3-penten-2-one) and mesitylene (1,3,5-trimethylbenzene). However, Klassen *et al.* (1999) concluded that these reactions are not important under atmospheric conditions.

As discussed below, in the laboratory we undertook a systematic investigation of the heterogeneous chemistry of acetaldehyde, acetone and propionaldehyde on a variety of oxide particles including SiO₂, Al₂O₃, Fe₂O₃, TiO₂ and CaO (Li *et al.*

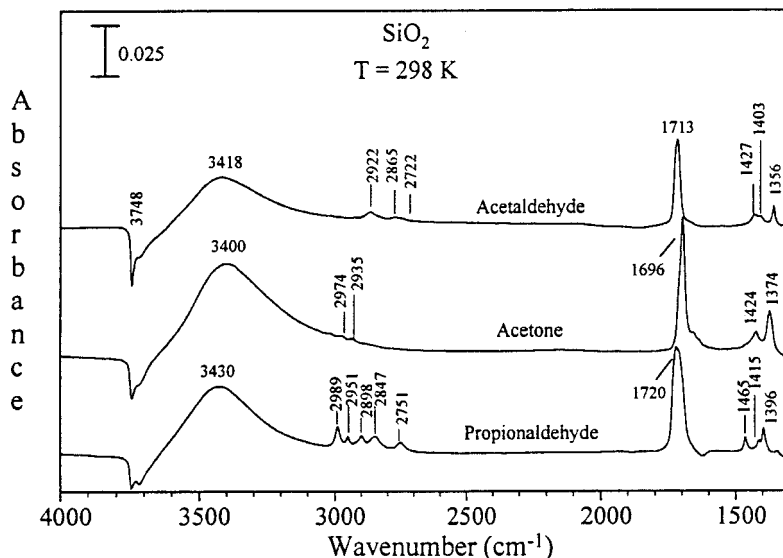


Figure 35. Transmission FTIR spectra of acetaldehyde, acetone and propionaldehyde adsorbed on SiO₂ particles in the presence of the carbonyl vapour at 20 mTorr and $T = 298$ K.

2001). These reactions are achieved at 298 K under dry conditions and the results are then incorporated into a box model for further analysis.

6.2. Transmission Fourier transform infrared and diffuse reflectance ultraviolet–visible spectroscopy of acetaldehyde, acetone and propionaldehyde adsorbed on SiO₂, α -Al₂O₃, α -Fe₂O₃, CaO and TiO₂

The adsorption of carbonyl compounds on oxide surfaces was investigated by two spectroscopic techniques: transmission FTIR spectroscopy and diffuse reflectance UV–visible spectroscopy. These two methods provide complementary spectroscopic data and are quite useful for studying the adsorption of carbonyl compounds on oxide particle surfaces. Figure 35 shows the IR spectra recorded of acetaldehyde, acetone and propionaldehyde respectively on SiO₂. The spectra were recorded in the presence of the gas phase. One of the most intense bands in the spectra near 1700 cm⁻¹ is assigned to the stretching motion of the carbonyl group. The frequencies of the absorption bands in the IR spectra for these molecules adsorbed on SiO₂ are very close to those in the gas or liquid phase. This suggests that these molecules weakly adsorb on SiO₂. The decrease in intensity of the band at 3748 cm⁻¹, associated with the isolated OH groups, and a concomitant growth of a band at lower frequencies near 3420 cm⁻¹ suggest that there is a hydrogen bonding interaction between the carbonyl compound and the surface hydroxyl groups (Pimentel and McClellan 1960, Little 1966, Hair 1967). Upon evacuation of the carbonyl vapour, the bands in the SiO₂ spectrum go away indicating that these molecules are physisorbed on the surface of these particles. UV–visible spectroscopy confirms that these molecules weakly and reversibly adsorb on the surface of the SiO₂ particles. Figure 36 shows the diffuse reflectance UV–visible spectra for several carbonyl compounds including acetaldehyde, acetone and propionaldehyde in the presence of the carbonyl vapour. The spectra show a reduction in the reflectivity of

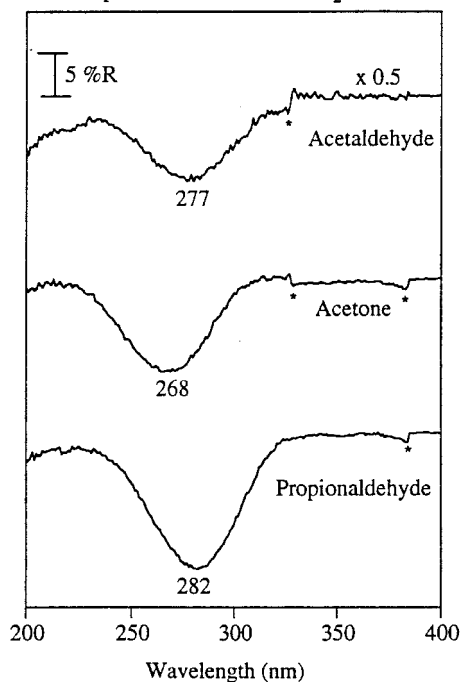
Diffuse Reflectance UV/Vis Spectra of Carbonyl Compounds Adsorbed on SiO₂ at 298 K

Figure 36. Diffuse reflectance UV-visible spectra of acetaldehyde, acetone and propionaldehyde adsorbed on SiO₂ particles in the presence of the carbonyl vapour. The asterisks (*) indicate where the filter changes, which sometimes results in a feature in the reflectivity spectrum and a change in the baseline.

the SiO₂ particles near 280 nm, very close to the wavelength maxima in the gas-phase absorption spectra observed for carbonyl compounds and is assigned to the $n \rightarrow \pi^*$ transition (Calvert and Pitts 1966).

In contrast with SiO₂, adsorption of these carbonyl compounds on all of the other oxide particles investigated is in part irreversible and the IR and UV-visible spectra of the adsorbed species show spectral features that are coverage dependent and significantly differ from the gas phase. Figure 37 shows the FTIR spectra obtained following the adsorption of acetaldehyde, acetone and propionaldehyde respectively on α -Al₂O₃ at a pressure near 20 mTorr. These spectra were recorded after the evacuation of the carbonyl vapour and thus represent the strongly bound species that remain on the surface. The spectra shown in figure 37 are very different from the spectra observed for these compounds when adsorbed on SiO₂ (Figure 35). There are many more absorption bands, suggesting that more than one species is present on the surface. It is well known that heterogeneous reactions of carbonyl compounds occur readily on the surface of oxide particles (Reichle 1980). Carbonyl compounds can undergo self-coupling reactions known as Aldol condensation reactions on oxide surfaces that have either basic or acidic properties. All the oxides studied here, except for SiO₂, have either basic or acidic properties or both (Morrison 1990). The types of reaction that are possible for acetaldehyde, acetone and propionaldehyde on acidic and basic oxides are summarized in figure 38. As discussed below, evidence for the formation of these higher-molecular-weight

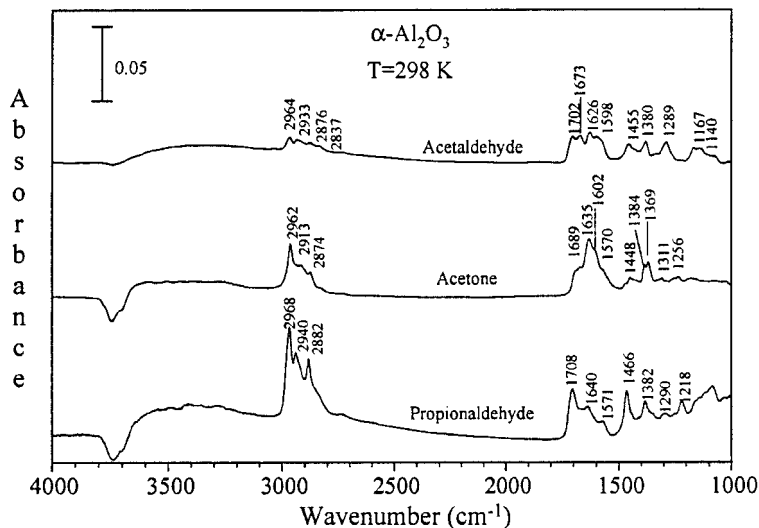


Figure 37. Transmission FTIR spectra of acetaldehyde, acetone and propionaldehyde adsorbed on $\alpha\text{-Al}_2\text{O}_3$ particles after evacuation of the carbonyl vapour at approximately 20 mTorr and $T = 298$ K.

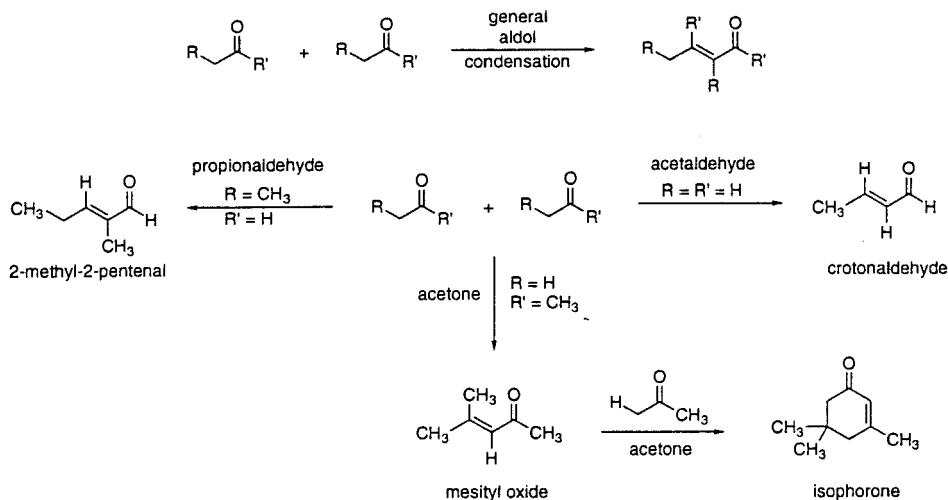


Figure 38. A reaction diagram showing the possible surface products that can form following aldol condensation reactions of acetaldehyde, acetone and propionaldehyde on oxide particles with acidic or basic properties.

carbonyl compounds on the surface of the oxide particles shown in figure 38 can be confirmed by the spectroscopic data.

Absorption bands between 1500 and 1750 cm^{-1} are characteristic features of saturated and unsaturated carbonyls. For heterogeneous reaction of acetaldehyde on $\alpha\text{-Al}_2\text{O}_3$, the spectra following exposure to acetaldehyde vapour are consistent with the formation of crotonaldehyde as indicated by the absorption bands observed in the region between 1500 and 1675 cm^{-1} . These bands are associated with the C=O and C=C stretching vibrations of an unsaturated aldehyde such as crotonaldehyde

(Rekoske and Barteau 1999). Similar types of adsorption band for unsaturated carbonyl compounds are also seen in the spectra of α -Al₂O₃ following exposure to acetone and propionaldehyde. These can be assigned to the formation of mesityl oxide and 2-methyl-2-pentenal from the aldol condensation reaction followed by dehydration of acetone and propionaldehyde respectively (Reichle 1980, Hanson *et al.* 1987, Finocchio *et al.* 1994). There is evidence for other higher-molecular-weight carbonyl compounds in the IR spectrum of α -Al₂O₃ following exposure to acetone. The band at 1635 cm⁻¹ is identified with isophorone (Hanson *et al.* 1987). There is also evidence for molecular adsorption of acetaldehyde, acetone and propionaldehyde. Absorption bands above 1690 cm⁻¹ are assigned to molecularly adsorbed species that have not undergone reaction on the surface. Absorption bands between 2800 and 3000 cm⁻¹ are assigned to the C—H stretching motions of the adsorbed carbonyls and the absorption bands between 1000 and 1475 cm⁻¹ are assigned to deformations of the methyl groups in these adsorbed carbonyls.

The UV-visible data shown in figure 39 confirm the conversion of acetaldehyde, acetone and propionaldehyde to unsaturated carbonyl compounds when adsorbed on α -Al₂O₃ from the gas phase. The features observed in the reflectivity spectra of α -Al₂O₃ following exposure to acetaldehyde, acetone and propionaldehyde vapour correlate with formation of unsaturated carbonyl compounds as determined from

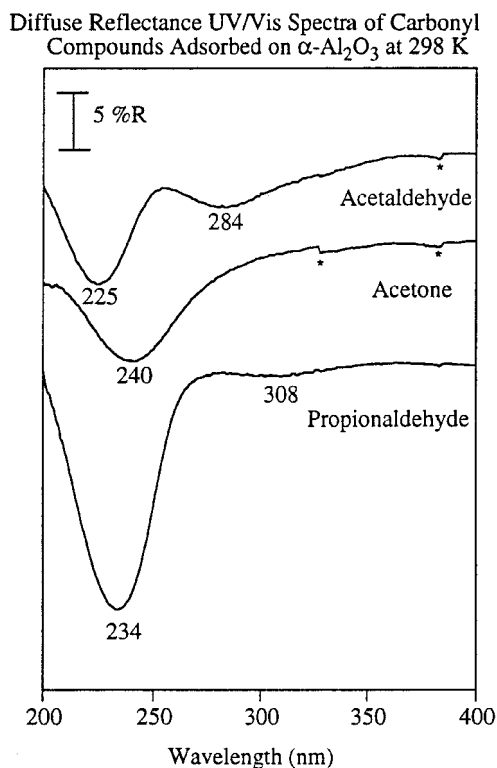


Figure 39. Diffuse reflectance UV-visible spectra of acetaldehyde, acetone and propionaldehyde adsorbed on α -Al₂O₃ particles after evacuation of the carbonyl vapour. The asterisks (*) indicate where the filter changes, which sometimes results in a feature in the reflectivity spectrum and a change in the baseline.

authentic standards (*vide infra*). From acetaldehyde adsorption, there is the formation of crotonaldehyde. The feature in the reflectivity spectrum at 225 nm is consistent with the formation of crotonaldehyde. This band is assigned to the $\pi \rightarrow \pi^*$ transition in this molecule (Calvert and Pitts 1966). Similarly, from propionaldehyde adsorption, there is the formation of 2-methyl-2-pentenal. The two bands observed in the reflectivity spectra at 234 and 308 nm are consistent with the formation of 2-methyl-2-pentenal and the two bands are also assigned to the $\pi \rightarrow \pi^*$ and $n \rightarrow \pi^*$ transitions respectively in this molecule. As indicated by the IR data, acetone adsorption results in the formation of several unsaturated carbonyl compounds on $\alpha\text{-Al}_2\text{O}_3$ including isophorone and mesityl oxide. The feature at 240 nm is similar to that observed in spectra recorded of adsorbing isophorone on $\alpha\text{-Al}_2\text{O}_3$ and is thus assigned to this species. UV-visible spectra were also recorded following direct adsorption of crotonaldehyde and 2-methyl-2-pentenal from the gas phase and confirm the assignments made above.

FTIR spectroscopy was also used to investigate the adsorption of acetaldehyde, acetone and propionaldehyde on the other oxides investigated. The three other oxides investigated, namely $\alpha\text{-Fe}_2\text{O}_3$, CaO and TiO_2 , all have either basic and acidic properties. The spectroscopic data show that, in general, these compounds remain adsorbed on the surface of the oxide particles after evacuation of the gas phase. The data also show that the saturated carbonyl compounds acetaldehyde, acetone and propionaldehyde can undergo heterogeneous reactions to yield adsorbed higher-molecular-weight unsaturated carbonyl compounds on the surface of the oxide particles, as indicated by the absorption bands observed in the region between 1500 and 1675 cm^{-1} , when the surface has basic (e.g. CaO and TiO_2) or acidic ($\alpha\text{-Al}_2\text{O}_3$, $\alpha\text{-Fe}_2\text{O}_3$ and TiO_2) properties. The question remains about the extent to which these reactions can occur on the surface of these particles. In the next section, Knudsen cell data are presented to quantify the uptake of these molecules on oxide particle surfaces and to determine the kinetics of the formation of higher-molecular-weight species on the surface of oxide particles.

6.3. Knudsen cell measurements: heterogeneous uptake kinetics for acetaldehyde, acetone and propionaldehyde on SiO_2 , $\alpha\text{-Al}_2\text{O}_3$, $\alpha\text{-Fe}_2\text{O}_3$, CaO and TiO_2

Initial uptake coefficients of acetaldehyde, acetone and propionaldehyde on SiO_2 , $\alpha\text{-Al}_2\text{O}_3$, $\alpha\text{-Fe}_2\text{O}_3$, CaO and TiO_2 were studied. Representative Knudsen cell data are shown in figure 40 for the uptake of acetaldehyde, acetone and propionaldehyde on $\alpha\text{-Al}_2\text{O}_3$. The rectangular boxes labelled open in figure 40 indicate when the sample holder lid was open so that the powder was exposed to the carbonyl vapour. The gas pressure in the Knudsen cell was lower than that used in the spectroscopic investigations described earlier. For the Knudsen cell experiments, the pressure in the Knudsen cell reactor was approximately 2 μTorr , which corresponds to a molecular density near 6×10^{10} molecules cm^{-3} (corresponding to 4 ppb in an air mass). Using equation (8), γ_{obs} was calculated as a function of time, as shown in figure 41. The initial uptake $\gamma_{0,\text{obs}}$ for the entire sample is taken as the maximum in γ_{obs} . For acetaldehyde, acetone and propionaldehyde using sample masses of 12.3, 7.2 and 3.2 mg of $\alpha\text{-Al}_2\text{O}_3$, the $\gamma_{0,\text{obs}}$ values are 4.6×10^{-3} , 1.7×10^{-3} and 1.8×10^{-3} respectively. When the entire BET area of the sample is taken into account, the initial uptake coefficients $\gamma_{0,\text{BET}}$ are calculated via equation (23) to be 3.2×10^{-5} , 2.0×10^{-5} and 4.7×10^{-5} for acetaldehyde, acetone and propionaldehyde respectively on $\alpha\text{-Al}_2\text{O}_3$. The true initial uptake coefficient is taken as $\gamma_{0,\text{BET}}$ as the experiments are

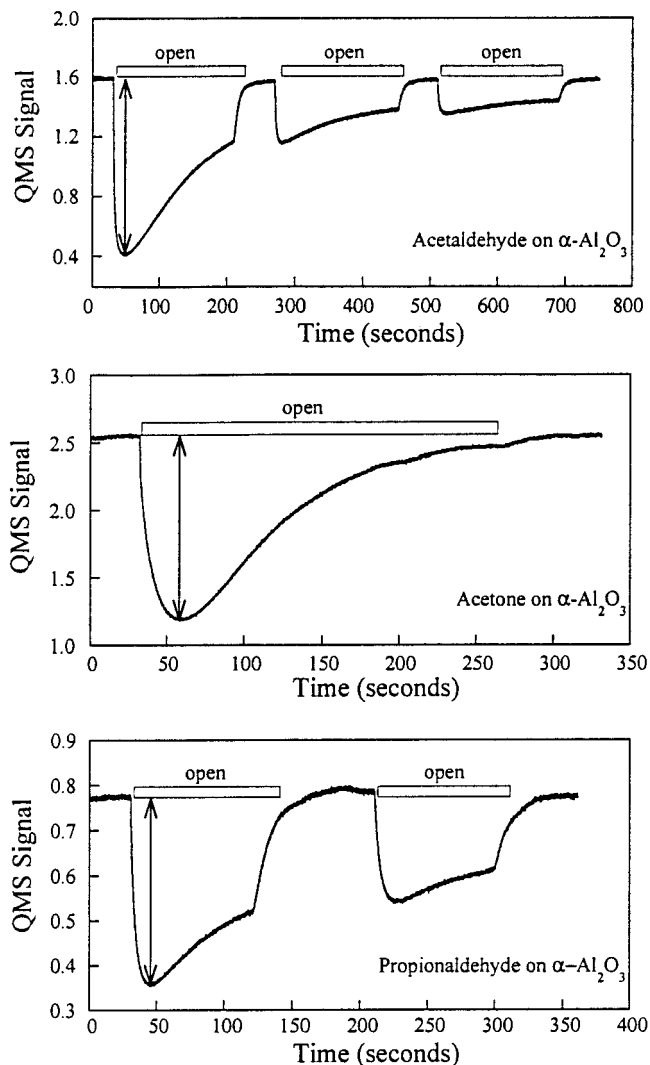


Figure 40. Representative Knudsen cell data showing the mass spectrometer signal I plotted as a function of time. The rectangular boxes labelled open indicate the time when the sample holder lid is open to the carbonyl vapour. In these experiments, heterogeneous uptake of acetaldehyde, acetone and propionaldehyde on $\alpha\text{-Al}_2\text{O}_3$ is examined.

made on small sample masses that are assumed to be in the linear mass regime. It can be seen in figure 41 that the uptake coefficient decreases as the surface becomes saturated with adsorbed molecules

Similar experiments were carried out for the other oxides investigated here and the initial uptake coefficients are reported in table 10. It can be seen that the true initial uptake coefficients for these carbonyl compounds range in order of magnitude from 10^{-4} to 10^{-6} . SiO_2 particles tend to be the least reactive having the lowest values for each of the compounds studied and CaO and TiO_2 having some of the

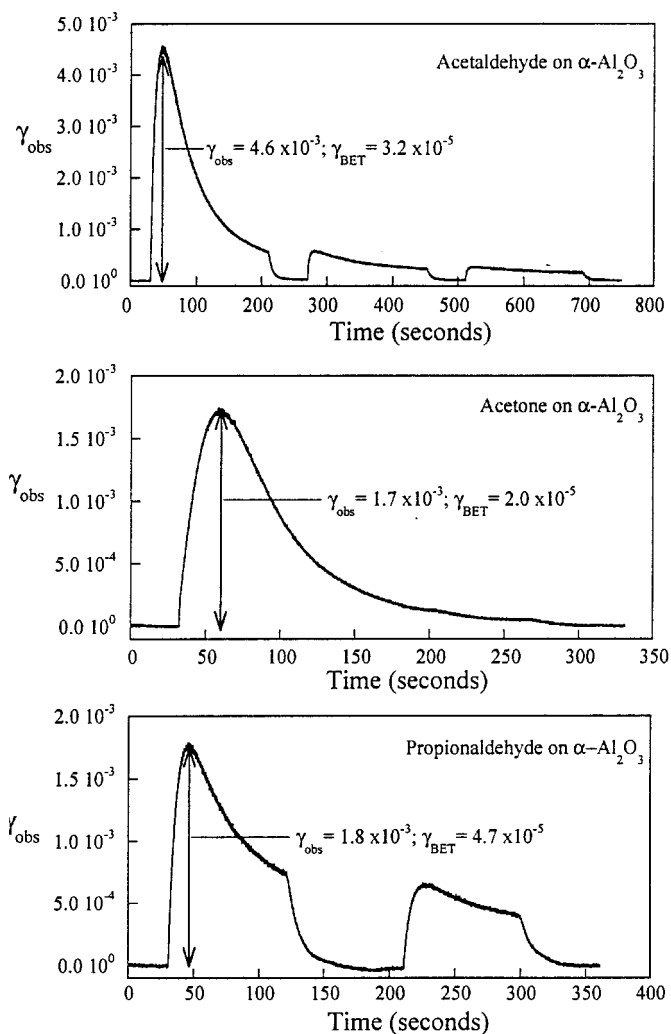


Figure 41. The mass spectral data are converted to an observed uptake coefficient γ_{obs} via equation (8). The data show that, as the reaction proceeds, the surface becomes saturated and there is a decrease in γ_{obs} from its initial value $\gamma_{0,\text{obs}}$. When the data are corrected for the BET area, via equation (23), the initial uptake is several orders of magnitude smaller than the observed uptake calculated using the geometric sample holder area. The initial heterogeneous uptake coefficients for acetaldehyde, acetone and propionaldehyde on $\alpha\text{-Al}_2\text{O}_3$ as well as on the other oxides investigated are listed in table 10.

highest values. The average values of the true initial uptake coefficient for acetaldehyde, acetone and propionaldehyde are 8.7×10^{-5} , 2.1×10^{-4} and 1.7×10^{-4} respectively, as determined using the BET area.

There is evidence in the Knudsen cell experiments for the formation of higher-molecular-weight unsaturated carbonyl compounds that form as a result of an aldol condensation reaction. For each of the gases investigated, the mass spectrum was also set to follow the parent ion of the aldol condensation reaction product. It was

Table 10. Initial uptake coefficients of acetaldehyde, acetone and propionaldehyde on mineral oxide particles.

Oxide	$\gamma_{0,\text{obs,all layers}}$	Mass (g)	Total BET area (m^2) ^a	Correction factor ^b	$\gamma_{0,\text{BET}}$
Acetaldehyde					
SiO ₂	6.2×10^{-3}	0.0053	1.0600	887	7.0×10^{-6}
α -Al ₂ O ₃	4.6×10^{-3}	0.0123	0.1722	144	3.2×10^{-5}
α -Fe ₂ O ₃	6.0×10^{-5}	0.0107	0.0246	21	2.9×10^{-6}
TiO ₂	7.4×10^{-3}	0.0019	0.0950	79	9.4×10^{-5}
CaO	4.5×10^{-3}	0.0047	0.0183	15	3.0×10^{-4}
Acetone					
SiO ₂	5.0×10^{-3}	0.0012	0.9600	803	6.2×10^{-6}
α -Al ₂ O ₃	1.7×10^{-3}	0.0072	0.1008	84	2.0×10^{-5}
α -Fe ₂ O ₃	9.5×10^{-3}	0.0300	0.0690	58	1.6×10^{-4}
TiO ₂	1.8×10^{-2}	0.0012	0.0600	50	3.6×10^{-4}
CaO	1.8×10^{-3}	0.0045	0.0180	15	1.2×10^{-4}
Propionaldehyde					
SiO ₂	4.6×10^{-3}	0.0025	0.5000	418	1.1×10^{-5}
α -Al ₂ O ₃	1.8×10^{-3}	0.0032	0.0448	38	4.7×10^{-5}
α -Fe ₂ O ₃	2.5×10^{-3}	0.0253	0.0582	49	5.1×10^{-5}
TiO ₃	8.5×10^{-3}	0.0014	0.0700	56	1.5×10^{-4}
CaO	1.7×10^{-2}	0.0088	0.0343	29	5.9×10^{-4}

^a BET surface in square metres per gram are given in the text.

^b Correction factor equals A_{BET}/A_s , where A_{BET} is equal to the total BET area and A_s is equal to 0.01195 m^2 .

found that, after an induction period, small amounts of the aldol condensation product desorbed into the gas phase. This trace amount is estimated to be less than 1% of the amount of carbonyl taken up by the surface based on measured QMS relative sensitivity factors.

The pressure dependence of the uptake of acetaldehyde and formation of crotonaldehyde on CaO was investigated further as a representative case. Six samples of similar masses were used to investigate the pressure dependence. The observed initial uptake was found to be pressure independent in the pressure regime extending from 2 to 20 μTorr (6×10^{10} to 6×10^{11} molecules cm^{-3}) indicating that the adsorption of acetaldehyde is first order in gas pressure. Crotonaldehyde was clearly observed as a product by mass spectrometry. The production of crotonaldehyde, as determined by mass spectrometry, is shown in figure 42. As discussed above, there is an initial induction period followed by a maximum in the rate of formation of crotonaldehyde. Crotonaldehyde production continues and then decreases until the surface is saturated. The maximum rate of formation of crotonaldehyde was measured as a function of pressure in the pressure regime extending from 2 to 20 μTorr (6×10^{10} to 6×10^{11} molecules cm^{-3}). A \ln - \ln plot of the maximum rate of formation of crotonaldehyde versus acetaldehyde pressure is plotted in the inset of figure 42. A linear fit to the data shows that the formation of crotonaldehyde is second order in acetaldehyde pressure.

Second-order kinetics are expected based on the following reaction sequence:

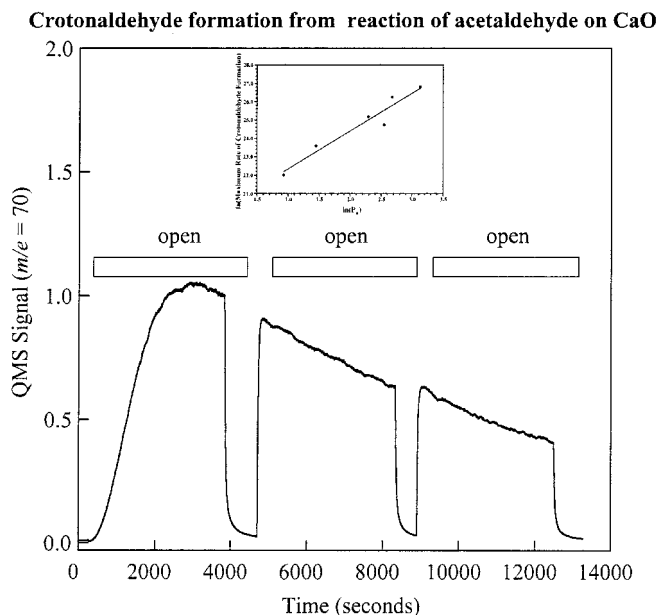
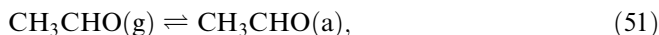


Figure 42. The production of crotonaldehyde from the adsorption of acetaldehyde on CaO was detected by QMS. The inset shows a $\ln\text{-}\ln$ plot of maximum crotonaldehyde formation as a function of acetaldehyde pressure. The pressure range used in these measurements extended from 2 to 20 μTorr . The linear fit to the data shown is $y = 2.06x + 20.30$; with $R = 0.96695$.



The desorption of crotonaldehyde is measured by the mass spectrometer and is used as a measure of the production of crotonaldehyde on the surface. According to this reaction sequence, the formation of crotonaldehyde is second order in acetaldehyde coverage θ_a . Assuming Langmuir adsorption-type kinetics, the coverage of acetaldehyde is proportional to the $KP_a(KP_a + 1)^{-1}$, where P_a is the pressure of acetaldehyde and K_a is the equilibrium constant for adsorption of acetaldehyde. When $KP_a \ll 1$, then θ_a is proportional to P_a ; thus the formation of crotonaldehyde is second order in acetaldehyde pressure.

The experimental data show that acetaldehyde, acetone and propionaldehyde readily adsorb on the surface of oxide particles corresponding to pressures in the parts per billion range and there is evidence for the formation of higher-molecular-weight compounds. Further evaluation of the impact of heterogeneous uptake of acetaldehyde, acetone and propionaldehyde in the atmosphere is discussed below.

6.4. Box-model analysis: atmospheric implications of carbonyl adsorption on mineral dust aerosol

The importance of heterogeneous reactions involving acetone, acetaldehyde and propionaldehyde on oxide and mineral aerosol surfaces needs to be evaluated relative to other loss mechanisms. As discussed above, under the conditions studied,

Table 11. The log-normal distributions used to calculate heterogeneous loss rates.^{a,b}

Mode		n_i	R_i	$\log(\sigma_i)$
Polar	I	2.17×10	0.068 9	0.245
	II	1.86×10^{-1}	0.375	0.300
	III	3.04×10^{-4}	4.29	0.291
Troposphere (background) ^c	I	1.29×10^2	0.003 6	0.645
	II	5.97×10	0.127	0.253
	III	6.35×10	0.259	0.425
Maritime	I	1.33×10^2	0.003 9	0.657
	II	6.66×10	0.133	0.210
	III	3.06	0.29	0.396
Urban	I	9.93×10^4	0.006 51	0.245
	II	1.11×10^3	0.007 14	0.666
	III	3.64×10^4	0.024 8	0.337
Dust ^b	I	7.98	0.88	0.23

^a From Jaenicke and Hanusch (1993) and Zhang *et al.* (1994).

^b Other conditions: diffusivity, $1.48 \times 10^{-11} \text{ cm}^2 \text{ s}^{-1}$; density, 2.0 g cm^{-3} ; mean free path, $0.07 \mu\text{m}$ in the boundary layer and $0.10 \mu\text{m}$ at 4 km.

^c The major difference between the background in the boundary layer and at 4 km is the mean free path.

the laboratory results show irreversible uptake of the carbonyl compounds for most of the oxides investigated. Under the assumption of irreversible uptake, an effective first order rate constant for heterogeneous loss of gaseous carbonyls can be calculated. The heterogeneous uptake of carbonyl compounds was modelled as a pseudo-first-order kinetic expression using the equations described in section 2.4. The k_j values for acetone, acetaldehyde and propionaldehyde were calculated from the above expressions as a function of uptake coefficient using various log-normal distributions for the aerosol number–size distribution (Jaenicke and Hanusch 1993, Pandis *et al.* 1993, Zhang *et al.* 1994). The expression for the log-normal number–size distribution used here is given in equation (35). A summary of the size distribution features used in the calculation is given in table 11. The results are presented in figure 43. The mass transfer uptake rates are highest in polluted environments near the Earth's surface and are lower in the upper troposphere and remote areas as the aerosol size distribution and aerosol loadings change. The mass transfer rate constants vary from about 3×10^{-9} to about $2 \times 10^{-5} \text{ s}^{-1}$ over the range of uptake values reported here.

These rates need to be compared with the major gas-phase chemical loss processes (i.e. photolysis and reactions with OH and NO_3). The photolysis rates of acetone, acetaldehyde and propionaldehyde as a function altitude and season were calculated using the TUV model (Madronich and Flocke 1997) at 30°N latitude. For example, diurnally averaged photolysis rates of acetone increase with altitude from about 10^{-7} s^{-1} at the surface to values of about 10^{-6} s^{-1} at 16 km and are a maximum in the summer. These values are similar to those calculated by McKeen *et al.* (1997). Estimated lifetimes of acetone against loss by photolysis in the upper troposphere thus vary from about 20 days in summer to 170 days in winter. The loss rates by photolysis are shown in figure 43 together with representative loss rates for reaction with OH and NO_3 using 12 h day and night average values of 2×10^6 and $5 \times 10^8 \text{ molecule cm}^{-3}$ respectively. These results indicate that the heterogeneous loss

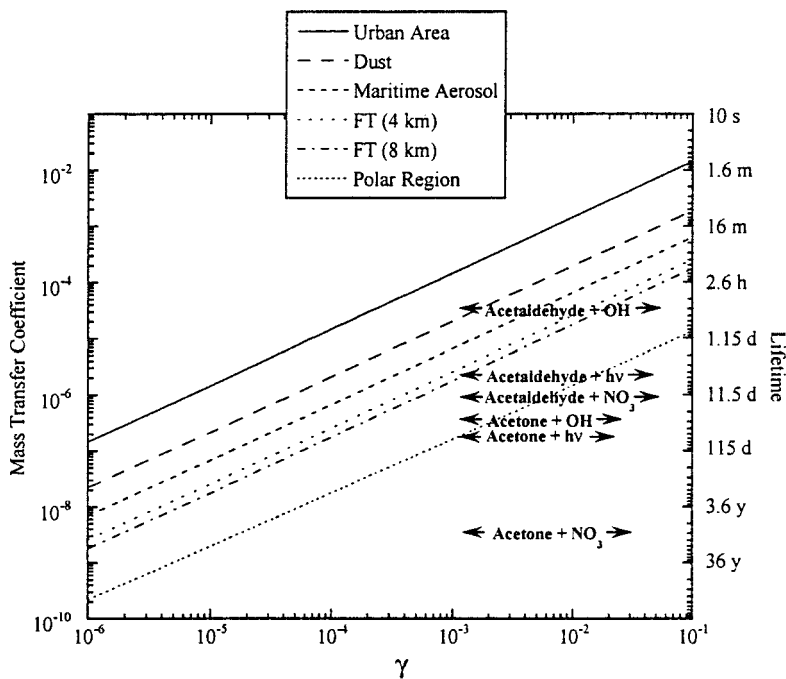


Figure 43. Calculated mass transfer coefficients as a function of the heterogeneous uptake γ (the ranges of measured values of γ are indicated by the arrows). Acetone and acetal (acetaldehyde) photolysis rates and other loss rates due to reaction with OH and NO_3 are shown for comparison. This diagram shows that, under certain conditions, the loss rates of these carbonyl compounds through heterogeneous uptake are comparable with other loss rate mechanisms.

rates measured for carbonyls are comparable with those due to gas-phase processes in the middle and upper troposphere.

The consequences of carbonyl uptake on mineral aerosol are determined by the ultimate fate of the surface-adsorbed carbonyl. If the adsorbed carbonyl molecules remain on the surface then the net effect on the chemistry of the troposphere will be to decrease the HO_x production from carbonyl compounds. However, if the surface adsorbed carbonyl molecules react further then they may have a greater or lesser impact on net HO_x production. To illustrate the possible impact on HO_x chemistry, box-model calculations were performed with the assumption that the surface species react with the same rates and products as gaseous mesitylene (i.e. reaction rate with OH). Under this assumption, and for the same conditions as given in table 11, it was found that HO_x levels were *increased* (over that without the heterogeneous reaction) by 10 to about 100% over the range of k values. The subsequent fate of the surface-adsorbed carbonyl compounds is at present being studied.

The uptake of carbonyl compounds may also represent a source of aerosol secondary organic matter. To illustrate this possibility, the resulting organic mass fraction (as a percentage) due to the continuous and irreversible uptake of acetone on to the mineral aerosol distributions in table 11 was calculated and the results presented in table 12. As shown for typical uptake rates in the free troposphere (10^{-6} s^{-1}) acetone uptake could result in secondary organic aerosol mass fractions of

Table 12. Estimated organic mass fraction of the aerosol due to the irreversible uptake of acetone on to the mineral aerosol size distributions summarized in table 11. The pseudo-first-order reaction coefficients span the range of values calculated using the measured acetone uptake rates as shown in figure 43. These illustrative examples are for 1 ppb acetone; an aerosol volume density of 2.8×10^{-12} (cm^3 aerosol) (cm^{-3} air) and an aerosol mineral density of 1.5 g cm^{-3} .

k (s^{-1})	Estimated organic mass fraction (%) for the following exposure times						
	1 h	5 h	10 h	1 day	5 days	10 days	20 days
10^{-4}	16	50	66	82	96	97	98
10^{-5}	2	10	16	31	69	82	90
10^{-6}	0.2	1	1.9	4.5	19	31.8	48.3
10^{-7}	0.02	0.1	0.2	0.5	2.3	4.5	8.5

5–30%. For reference, assuming a BET/geometric surface area ratio of 30 and a monolayer coverage of 5×10^{14} (molecules acetone) cm^{-2} , a 10% organic mass fraction corresponds to an aerosol coverage of one monolayer.

7. Conclusions

The laboratory and modelling studies presented here suggest that there is compelling evidence that heterogeneous chemistry is important and plays a role in the chemical balance of the troposphere. Heterogeneous reactions should be included in atmospheric chemistry models if the models are to describe adequately all the molecular-level processes that occur. There is still much to be explored in laboratory studies of heterogeneous reactions on solid aerosol surfaces. Some of the questions that remain include the following.

- What additional reactions take place on aerosol surfaces?
- What are the reaction products (in the gas and/or aerosol phase)?
- How do these chemical processes impact aerosol composition and properties (e.g. can they alter radiative properties)?
- How do they influence gas-phase compositions (e.g. do they alter NO_2 , HO_x and O_3 distributions)?
- Under what situations are such reactions expected to be important (at night, in urban environments, upper troposphere, etc.)?
- What processes restrict or enhance the effectiveness of these reactions (e.g. surface saturation effects or surface regeneration effects)?
- What is the role of H_2O , $h\nu$, temperature and reactant mixtures (carbonyls, NO_x and O_3 together in the same air mass), etc., in increasing and/or decreasing the importance of heterogeneous reactions on aerosol surfaces?

Acknowledgements

The research described herein would not have been done without the expertise and efforts of many individuals. My collaborator Professor Gregory Carmichael has been an invaluable resource. He and his group provided the modelling analysis for this project. Former students of my research group, Dr Todd Miller and Dr Angela

Goodman, as well as former postdoctoral scientists, Dr Grant Underwood and Dr Ping Li, were instrumental in developing the experimental apparatus and expertise needed for these studies. Current graduate students Hind Al-Abdaleh and Courtney Usher have also contributed to this work and continue with these studies together with graduate students Brenda Krueger and Sofia Carlos-Cuellar. The aerosol chamber was primarily designed and constructed by Professor Mark Young and Professor Paul Kleiber together with students Amy Preszler Prince and Jennifer Wade. Their efforts are gratefully acknowledged. This work would not have been possible without funding from the National Science Foundation (grants CHE-9988434 and CHE-9614134), Department of Energy Atmospheric Chemistry Program (grant DE-FG01-98ER62580) and the Camille and Henry Dreyfus Postdoctoral Program in Environmental Science. The support provided by these agencies and foundation is gratefully acknowledged. Seed grants funded through the University of Iowa's Carver Scientific Research Grant Program, The Center for Global and Regional Environmental Research and The Environmental Health Sciences Research Center are also gratefully acknowledged.

References

- ABBATT, J. P. D., BEYER, K. D., FUCALORO, A. F., MCMAHON, J. R., WOOLDRIDGE, P. J., ZHONG, R., and MOLINA, M. J., 1992, *J. geophys. Res.*, **97**, 819.
- AKHTER, M. S., CHUGHTAI, A. R., and SMITH, D. M., 1984, *J. phys. Chem.* **88**, 5334.
- AL-ABADLEH, H. A., and GRASSIAN, V. H., 2000, *J. phys. Chem. A*, **104**, 11 926.
- AMMANN, M., KALBERER, M., JOST, D. T., TOBLER, L., ROSSLER, E., PIGUET, D., GAGGELER, H. W., and BALTENSPERGER, U., 1998, *Nature*, **395**, 157.
- APPEL, B. R., WINER, A. M., TOKIWA, Y., and BIERMANN, H. W., 1990, *Atmos. Environ.*, **3**, 611.
- ARIS, R., 1975 *The Mathematical Theory of Diffusion and Reaction in Permeable Catalysts*, Vol. I (Oxford: Clarendon).
- ARNOLD, F., BURGER, V., FANKE, B., GRIMM, F., KRIEGER, A., SCHNEIDER, J., and STILP, T., 1997, *Geophys. Res. Lett.*, **24**, 3017.
- AUMONT, B., MADRONICH, S., AMMANN, M., KALBERER, M., BALTENSPERGER, U., HAUGLUSTAINE, D., and BROCHETON, F., 1999, *J. geophys. Res.*, **104**, 1729.
- AYERS, G., GILLET, R., and GRANER, H., 1997, *Geophys. Res. Lett.*, **24**, 401.
- BARRACLOUGH, P. B., and HALL, P. G., 1974, *Surf. Sci.*, **46**, 393.
- BAULCH, D. L., COX, R. A., CRUTZEN, P. J., HAMPSON, R. F., KERR, J. A., TROE, J., and WATSON, R. T., 1982, *J. phys. Chem. Ref. Data*, **11**, 327.
- BECKER, K. H., KLEFFMANN, J., and KURTENBACH, R., 1996, *J. phys. Chem.* **100**, 14984.
- BEICHERT, P., and FINLAYSON-PITTS, B. J., 1996, *J. phys. Chem.*, **100**, 15 218.
- BORENSEN, C., KIRCHNER, U., SCHEER, V., VOGT, R., and ZELLNER, R., 2000, *J. phys. Chem. A*, **104**, 5030.
- BUNCE, N., 1994, *Environmental Chemistry* (Wurtz).
- BUSCA, G., and LORENZELLI, V. J., 1981, *J. Catal.*, **72**, 303.
- CALOZ, F., FENTER, F. F., TABOR, K. D., and ROSSI, M. J. 1997, *Rev. scient. Instrum.*, **68**, 3172.
- CALVERT, J. G., and PITTS, J. N., JR, 1966, *Photochemistry* (New York: Wiley).
- CARMICHAEL G. R., PETERS, L. K., and SAYLOR, R. D., 1991, *Atmos. Environ. A*, **25**, 2077.
- CHAN, W. H., NORDSTROM, R. J., CALVERT, J. G., and SHAW, J. H., 1976, *Environ. Sci. Technol.*, **10**, 674.
- CHARLSON, R. J., SCHWARTZ, S. E., HALES, J. M., CESS, R. D., COAKLEY, J. A., HANSEN, J. E., and HOFMANN, D. J., 1992, *Science*, **255**, 423.
- CHATFIELD R. B., 1994, *Geophys. Res. Lett.*, **21**, 2705.
- CHUGHTAI, A. R., WELCH, W. F., JR, AKHTER, M. S., and SMITH, D. M., 1990, *Appl. Spectrosc.* **44**, 294.

- COX, R. A., 1984, *J. Photochem.* **25**, 43.
- CRIST K., CARMICHAEL, G. R., HOTCHKISS, B., and JOHN, K., 1996, *Air Pollution Modeling and Its Application XI*, edited by S.-E. Gryning and F. A. Schiermeier (New York: Plenum), p. 155.
- CUNNINGHAM, P. T., JOHNSON, S. A., and YANG, R. T., 1974, *Environ. Sci. Technol.*, **8**, 131.
- DAVIES, J. A., and COX, R. A., 1998, *J. phys. Chem.*, **102**, 7631.
- DAVYDOV, A. A., 1990, *Infrared Spectroscopy of Adsorbed Species on the Surface of Transition Metal Oxides* (New York: Wiley).
- DEHAAN, D. O., BRAVERS, T., OUM, K., STUTZ, J., NORDMEYER, T., and FINLAYSON-PITTS, B. J., 1999, *Int. Rev. phys. Chem.*, **18**, 343.
- DENTENER, F. J., and CRUTZEN, P. J., 1993, *J. geophys. Res.*, **98**, 7149.
- DENTENER, F., CARMICHAEL, G., ZHANG, Y., LELIFELD, J., and CRUTZEN, P., 1996, *J. geophys. Res.*, **101**, 869.
- DONAHUE, N. M., DUBEY, M. K., MOHRSLADT, R., DEMERJIAN, K. L., and ANDERSON, J. G., 1997, *J. geophys. Res.*, **102**, 6159.
- DUANE, S. X., JAYNE, J. T., DAVIDOVITS, P., WORSNOP, D. R., ZAHNISER, M. S., and KOLB, C. E., 1993, *J. phys. Chem.*, **97**, 2284.
- DUNCAN, J. L., SCHINDLER, L. R., and ROBERTS, J. T., 1999, *J. phys. Chem. B*, **103**, 7247.
- DUSHMAN, S., 1962, *Scientific Foundations of Vacuum Technique*, second edition (New York: Wiley).
- FEBO, A., and PERRINO, C., 1991, *Atmos. Environ. A*, **25**, 1055.
- FEBO, A., PERRINO, C., and ALLEGRINI, I., 1996, *Atmos. Environ.*, **30**, 611.
- FENTER, F. F., CALOZ, F., and ROSSI, M. J., 1996, *J. phys. Chem.*, **100**, 1008.
- FINLAYSON-PITTS, B. J., and PITTS JR., J. N., 1986, *Atmospheric Chemistry: Fundamentals and Experimental Techniques* (New York: Wiley), p. 540.
- FINOCCHIO, E., BUSCA, G., LORENZELLI, V., and WILLEY, R. J., 1994, *J. chem. Soc., Faraday Trans.*, **90**, 3347.
- FLOOD, E. A., 1966, *The Solid Gas Interface* (New York: Marcel Dekker).
- FUCHS, N. A., and SUTUGIN, A. G., 1970, *Highly Dispersed Aerosols* (Ann Arbor, Michigan: Ann Arbor Science).
- GARD, E. E., KLEEMAN, M. J., GROSS, D. S., HUGHES, L. S., ALLEN, J. O., MORRICAL, B. D., FERGENSON, D. P., DIENES, T., GALLI, M. E., JOHNSON, R. J., CASS, G. R., and PRATHER, K. A., 1998, *Science*, **279**, 1184.
- GERECKE, A., THIELMANN, A., GUTZWILLER, L., and ROSSI, M., 1998, *Geophys. Res. Lett.*, **25**, 2453.
- GOLDEN, D. M., MANION, J. A., REIHS, C. M., and TOLBERT, M. A., 1994, *The Chemistry of the Atmosphere: Its Impact on Global Change*, edited by J. G. Calvert (Oxford: Blackwell Scientific).
- GOLDEN, D. M., SPOKES, G. N., and BENSON, S. W., 1973, *Angew. Chem., int. Edn Engl.*, **12**, 534.
- GOODMAN, A. L., 2000, PhD Dissertation, The University of Iowa.
- GOODMAN, A. L., BERNARD, E. B., and GRASSIAN, V. H., 2001, *J. phys. Chem. A* (in the press).
- GOODMAN, A. L., UNDERWOOD, G. M., and GRASSIAN, V. H., 1999, *J. phys. Chem. A*, **103**, 7217; 2000, *J. geophys. Res.*, **104**, 053.
- GREGG, S. J., and SING, K. S., 1967, *Adsorption, Surface Area and Porosity* (New York: Academic Press).
- GROSJEAN, E., GROSJEAN, D., FRAZER, M., and CASS, G., 1996, *Environ. Sci. Technol.*, **30**, 2687.
- HADJIIVANOV, K. I., 2000, *Catal. Rev.*, **42**, 71.
- HADJIIVANOV, K., BUSHEV, V., KANTCHEVA, M., and KLISSURSKI, D., 1994, *Langmuir*, **10**, 464.
- HADJIIVANOV, K. I., KLISSURSKI, D. G., and BUSHEV, V. P., 1995, *J. chem. Soc., Faraday Trans.*, **91**, 149.
- HAIR, M. L., 1967, *Infrared Spectroscopy in Surface Chemistry* (New York: Marcel Dekker).
- HAN, J. H., and MARTIN, S. T. 1999, *J. geophys. Res.*, **104**, 3543.
- HANSON, B. E., WIESERMAN, L. F., WAGNER, G. W., and KAUFMAN, R. A., 1987, *Langmuir*, **3**, 549.

- HARRISON, R. M., and KITTO, A. M. N., 1994, *Atmos. Environ.*, **28**, 1089.
- HARRISON, R. M., PEAK, J. D., and COLLINS, G. M., 1996, *J. geophys. Res.*, **101**, 14429.
- HEMMINGER, J. C., 1999, *Int. Rev. phys. Chem.*, **18**, 387.
- HITCHMAN, M. A., and ROWBOTTOM, G. L., 1982, *Coordination Chem. Rev.*, **42**, 55.
- HOTCHKISS, B., 1996, MS Thesis, Department of Chemical and Biochemical Engineering, The University of Iowa.
- IRACI, L. T., and TOLBERT, M. A., 1997, *J. geophys. Res.*, **102**, 099.
- JACOB, D. J., 2000, *Atmos. Environ.*, **34**, 2131.
- JACOX, M. E., 1990, *J. phys. Chem. Ref. Data*, **9**, 1444.
- JAENICKE, R., and HANUSCH, T., 1993, *Aerosol Sci. Technol.*, **18**, 309.
- JAYNE, J. T., WORSNOP, D. R., KOLB, C. E., SWARTZ, E., and DAVIDOVITZ, P., 1996, *J. phys. Chem.*, **100**, 8015.
- JENKIN, M. E., COX, R. A., and WILLIAMS, D. J., 1988, *Atmos. Environ.*, **22**, 487.
- JONAS, P., CHARLSON, R., and RODHE, H., 1995, *Aerosols in Climate Change* (Cambridge University Press).
- JOYNER, L. G., WEINBERGER, E. B., and MONTGOMERY, C. W., 1945, *J. Am. chem. Soc.*, **67**, 2182.
- JUNKERMANN, W., and IBUSUKI, T., 1992, *Atmos. Environ. A*, **26**, 3099.
- KAISER, E. W., and WU, C. H., 1977, *J. phys. Chem.* **81**, 1701.
- KALBERER, M., AMMANN, M., ARENS, F., GÄGGELER, H. M., and BALTENSBERGER, U., 1999, *J. geophys. Res.* **104**, 13 825.
- KALBERER, M., AMMANN, M., GÄGGELER, H. M., and BALTENSBERGER, U., 1999, *Atmos. Environ.* **33**, 2815.
- KALBERER, M., TABOR, K., AMMANN, M., PARRAT, Y., WEINGARTHER, E., PIGHET, D., RÖSSLER, E., JOST, D. T., TÜRLE, A., GÄGGELER, H. W., and BALTENSBERGER, U., 1996, *J. phys. Chem.*, **100**, 15 487.
- KAMM, S., MÖHLER, O., NAUMANN, K.-H., SAATHOFF, H., and SCHURATH, U., 1999, *Atmos. Environ.*, **33**, 4651.
- KANE, S., TIMONEN, R., and LEU, M.-T., 1999, *J. phys. Chem. B*, **103**, 9259.
- KEYSER, L. F., MOORE, S. B., and LEU, M.-T., 1991, *J. phys. Chem.*, **95**, 5496.
- KING, D. A., and TOMKINS, F. C., 1968, *Trans. Faraday Soc.*, **64**, 496.
- KLASSEN, J. K., LYNTON, J., GOLDEN, D. M., and WILLIAMS, L. R., 1999, *J. geophys. Res.*, **104**, 26 355.
- KLEFFMANN, J., BECKER, K., LACKHOFF, M., and WIESEN, P., 1999, *Phys. Chem. chem. Phys.* **1**, 5443.
- KLEFFMANN, J., BECKER, K. H., and WIESEN, P., 1998, *Atmos. Environ.*, **32**, 2721.
- KOLB, C. E., WORSNOP, D. R., ZAHNISER, M. S., DAVIDOVITZ, P., KEYSER, L. F., LEU, M.-T., MOLINA, M. J., HANSON, D.R., RAVISHANKARA, A.R., WILLIAMS, L. R., and TOLBERT, M. A., 1995, *Progress and Problems in Atmospheric Chemistry*, Advanced Series in Physical Chemistry, Vol. 3, p. 771.
- LAMMEL, G., and CAPE, J. N., 1996, *Chem. Soc. Rev.*, **25**, 361.
- LAMMEL, G., and PERNER, D., 1988, *J. Aerosol. Sci.*, **19**, 1199.
- LEE, Y. N., ZHOU X., KLEINMAN, L. I., NUNNEMACKER, L. J., SPRINGSTON, S.R., DAUM, P. H., NEWMAN, L., KEIGLEY, W. G., HOLDREN, M. W., SPICER, C. W., YOUNG, V., FU, B., PARRISH, D. D., HOLLOWAY, J., WILLIAMS J., ROBERTS, J. M., RYERSON, T. B., and FEHSENFELD, F. C., 1998, *J. geophys. Res.*, **103**, 22 449.
- LEE, Y. N., and SCHWARTZ, S. E., 1981, *J. geophys. Res.*, **86**, 971.
- LEUCHS, M., and ZUNDEL, G., 1978, *J. phys. Chem.*, **82**, 1632.
- LI, P., PERREAU, K. A., COVINGTON, E., SONG, C. H., CARMICHAEL, G. R., and GRASSIAN, V. H., 2001, *J. Geophys. Res.*, **106**, 5517.
- LIDE, D. R., 1991, *Handbook of Chemistry and Physics* (Boca Raton, Florida: CRC Press), pp. 4-47.
- LITTLE, L. H., 1966, *Infrared Spectra of Adsorbed Species* (New York: Academic Press).
- LIU, S. C., TRAINER, M., CARROLL, M. A., HUBLER, G., MONTZKA, D. D., NORTON, R. B., RIDLEY, B. A., WALEGA, J. G., ATLAS, E. L., HEIKES, B. G., HUEBERT, B. J., and WARREN, W., 1992, *J. geophys. Res.*, **97**, 10 463.
- LONGFELLOW, C. A., RAVISHANKARA, A. R., and HANSON, O. R., 1999, *J. geophys. Res.*, **104**, 13 833.

- LURMANN, F. W., LOYD, A. C., and ATKINSON, R. A., 1986, *J. Geophys. Res.*, **91**, 10905.
- MADRONICH, S., and FLOCKE, S., 1997, *Solar Ultraviolet Radiation Modeling, Measurements and Effects*, edited by C. S. Zerefos and A. F. Bais (Berlin: Springer-Verlag).
- MAMANE, Y., and GOTTLIEB, J., 1990, *J. Aerosol Sci.*, **21**, S225.
- MARTIN, S. T., 2000, *Chem. Rev.*, **100**, 3403.
- MASEL, R., 1996, *Principles of Adsorption and Reaction on Solid Surfaces* (New York: Wiley).
- McKEEN S., GIERCZAK, T., BUCKHOLDER, J., WENNBERG, P., HANISCO, T., KLEIM, E., GAO, R., LIU, S., RAVISHANKARA, A., and FAHEY, D., 1997, *Geophys. Res. Lett.*, **24**, 3177.
- MILLER, T. M., and GRASSIAN, V. H., 1998, *Geophys. Res. Lett.*, **25**, 3835.
- MOLINA, M., 1994, *The Chemistry of the Atmosphere: Its Impact on Global Change*, edited by J. G. Calvert (Oxford: Blackwell Scientific), pp. 27–38.
- MOLINA, M. J., MOLINA, L. T., and KOLB, C. E., 1996, *A. Rev. phys. Chem.*, **47**, 327.
- MORRISON, S. R., 1990, *The Chemical Physics of Surfaces*, second edition (New York: Plenum), p. 154.
- NAKAMOTO, K., 1970, *Infrared Spectra of Inorganic and Coordination Compounds* (New York: Wiley).
- NAVIO, J. A., CERRILLOS, C., and REAL, C., 1996, *Surf. Interface Anal.*, **24**, 355.
- NOTHOLT, J., HJORTH, J., and RAES, F., 1992, *Atmos. Environ.*, **26**, 211.
- PANDIS, S. N., and SEINFELD, J. H., 1999, *Atmospheric Chemistry and Physics Air Pollution to Climate Change* (New York: Wiley).
- PANDIS, S. N., WEXLER, A. S., and SEINFELD, J. H., 1993, *Atmos. Environ. A.*, **27**, 2403.
- PARRISH, D., RYERSON, T., HOLLOWAY, J., TRAINER, M., and FEHSENFELD, F., 1999, *Atmos. Environ.*, **33**, 5147.
- PETERS, J. S., and EWING, G. E., 1996, *J. phys. Chem.*, **100**, 14 093; 1997, *J. phys. Chem. B*, **101**, 10 880.
- PHADNIS M., and CARMICHAEL, G., 2000, *J. atmos. Chem.*, **36**, 285.
- PIMENTEL, G. C., and MCCLELLAN, A. L., 1960, *The Hydrogen Bond* (San Francisco, California: Freeman).
- PITTS, JR, J. N., SANHUEZA, E., ATKINSON, R., CARTER, W. P. L., WINER, A. M., HARRIS, G. W., and PLUM, C. N., 1984, *Int. J. chem. Kinet.*, **16**, 919.
- POZDNYAKOV, D. V., and FILIMONOV, V. N., 1973, *Kinet. Katal.*, **14**, 760.
- RAVISHANKARA, A. R., 1997, *Science*, **276**, 1058.
- REICHEL, W. T., 1980, *J. Catal.*, **63**, 295.
- REKOSKE, J. E., and BARTEAU, M. A., 1999, *Langmuir*, **15**, 2061.
- ROGASKI, C. A., GOLDEN, D. M., and WILLIAMS, L. R., 1997, *Geophys. Res. Lett.*, **24**, 381.
- SAKAMAKI, F., HATAKEYAMA, S., and AKIMOTO, H., 1983, *Int. J. chem. Kinet.*, **15**, 1013.
- SALIBA, N. A., MOCHIDA, M., and FINLAYSON-PITTS, B. J., 2000, *Geophys. Res. Lett.*, **27**, 3229.
- SANDER, R., and CRUTZEN, P. J., 1996, *J. geophys. Res.*, **101**, 9121.
- SAYLOR, R. D., 1997, *Atmos. Environ.*, **31**, 3653.
- SCHURATH, U., and NAUMANN, K.-H., 1998, *Pure appl. Chem.*, **70**, 1353.
- SHEEHY, D. P., 1992, *Ambio*, **21**, 303.
- SHIMANOUCHE, T., 1977, *J. phys. Chem. Ref. Data*, **6**, 1039.
- SINGH, H. B., CHEN, Y., GREGORY, G. L., SACHSE, G., TALBOT, R., BLAKE, D. R., KONDO, Y., BRADSHAW, J., HEIKES, B., and THORNTON, D. 1997, *Geophys. Res. Lett.*, **24**, 127.
- SINGH, H. B., HERLTH, D., KOLYER, R., SALAS, L., BRADSHAW, J. D., SANDHOLM, S. J., DAVIS, D. D., CRAWFORD, J., KONDO, Y., KOIKE, M., TALBOT, R., GREGORY, G. L., SACHSE, G. W., BROWELL, E., BLAKE, D. R., ROWLAND, F. S., NEWELL, R., MERILL, J., HIEKES, B., LIU, S. C., CRUTZEN, P. J., and KANAKIDOU, M., 1996, *J. geophys. Res.*, **101**, 1793.
- SINGH, H. B., O'HARA, D., HERLTH, D., SACHSE, W., BLAKE, D. R., BRADSHAW, J. D., KANAKIDOU, M., and CRUTZEN, P. J., 1994, *J. geophys. Res.*, **99**, 1805.
- SMITH, D. M., WELCH, W. F., GRAHAM, S. M., CHUGHTAI, A. R., WICKE, B. G., and GRADY, K. A., 1988, *Appl. Spectrosc.* **42**, 674.
- SONG, C. H., 1999, PhD Thesis, The University of Iowa, pp. 108–146.
- SONG, C. H., and CARMICHAEL, G. R., 2001, *J. atmos. Chem.* (to be published).

- SVENSSON, R., LJUNGSTROM, E., and LINDQVIST, O., 1987, *Atmos. Environ.* **21**, 1529.
- TABAZADEH, A., JACOBSON, M. Z., SINGH, H. B., TOON, O. B., LIN, J. S., CHATFIELD, R. B., THAKUR, A. N., TALBOT, R. W., and DIBB, J. E., 1998, *Geophys. Res. Lett.*, **25**, 4185.
- TANNER, R., ZIELINSKA, B., UBERNA, E., HARSHFIELD, G., and MCNICHOL, A., 1996, *J. geophys. Res.*, **101**, 28 961.
- UNDERWOOD, G. M., LI, P., USHER, C. R., and GRASSIAN, V. H., 2000, *J. phys. Chem.*, **104**, 819.
- UNDERWOOD, G. M., MILLER, T. M., and GRASSIAN, V. H., 1999, *J. phys. Chem. A*, **103**, 6184.
- UNDERWOOD, G. M., SONG, C. H., PHADNIS, M., CARMICHAEL, G. C., and GRASSIAN, V. H., 2001, *J. geophys. Res.* (in the press).
- VOGT, R., ELLIOTT, C., ALLEN, H. C., LAUX, J. M., HEMMINGER, J. C., and FINLAYSON-PITTS, B. J., 1996, *Atmos. Environ.*, **30**, 1729.
- VOGT, R., and FINLAYSON-PITTS, B. J., 1994, *J. phys. Chem.*, **98**, 3747.
- YAN, B.-D., MEILINK, S. L., WARREN, G. W., and WYNBLATT, P., 1987, *IEEE Trans. Components, Hybrids Manufacturing Technol.*, **10**, 247.
- ZHANG, Y., and CARMICHAEL, G. R., 1999, *J. appl. Meteorol.*, **38**, 353.
- ZHANG, Y., SUNWOO, Y., KOTAMARTHI, V., and CARMICHAEL, G., 1994, *J. Appl. Meteorol.*, **33**, 813.